Hadronic Production of $\psi(2S)$ Cross section and Polarization

Kwangzoo Chung
of Carnegie Mellon University

A dissertation submitted to the Carnegie Mellon University
for the degree of Doctor of Philosophy

Abstract

The hadronic production cross section and the polarization of $\psi(2S)$ meson are measured by using the data from $p\overline{p}$ collisions at $\sqrt{s} = 1.96$ TeV collected by the Collider Detector at Fermilab. The datasets used correspond to integrated luminosity of 1.1 fb^{-1} and 800 pb^{-1}, respectively. The decay $\psi(2S) \to \mu^+\mu^-$ is used to reconstruct $\psi(2S)$ mesons in the rapidity range $|y(\psi(2S))| < 0.6$. The coverage of the p_T range is 2.0 GeV/$c \leq p_T(\psi(2S)) < 30$ GeV/c for the cross section analysis and $p_T \geq 5$ GeV/c for the polarization analysis. For events with $p_T(\psi(2S)) > 2$ GeV/c the integrated inclusive cross section multiplied by the branching ratio for dimuon decay is 3.17 $\pm$ 0.04 $\pm$ 0.28 nb . This result agrees with the CDF Run I measurement considering the increased center-of-mass energy from 1.8 TeV to 1.96 TeV. The polarization of the promptly produced $\psi(2S)$ mesons is found to be increasingly longitudinal as p_T increases from 5 GeV/c to 30 GeV/c. The result is compared to contemporary theory models.

Acknowledgements

For all those whom I am gratefully indebted to.

I would like to express my very special thanks to my advisor, Professor James Russ, for his invaluable guidance, support, and encouragement. I have learned a lot from you and those will be not only the foundation of my academic career but also the driving force in the future. I would also like to thank Professor Manfred Paulini for his help and advice in depth.

Thanks to all the people who kept the Tevatron accelerator and the CDF II detector running, thanks to all the members of CMU group at CDF for the great work environment, thanks to Mark Mattson for sharing his experience of the CDF Calorimeter ADMEM support, thanks to all my Korean colleagues for their hospitality, thanks to Dr. Han for those conversations on various aspects of life, and thanks to J.

And I am truly grateful to my parents for all their love and support. I love you and thank you for making it possible for me to be who I am today.

Contents

“In order to reach the truth, it is necessary, once in one’s life,
to put everything in doubt - so far as possible.”
— René Descartes 1596–1650

Chapter 1

Introduction

"Three quarks for Muster Mark!
Sure he has not got much of a bark
And sure any he has it's all beside the mark."
— from *Finnegans Wake*, James Joyce 1882–1941

1.1 Quantum Chromodynamics

Quantum Chromodynamics (QCD) is one of the important components of the Standard Model (SU(3) $\times$ SU(2) $\times$ U(1)). It is a non-Abelian gauge field theory describing the strong interactions of colored quarks and gluons. There are six flavors of quarks; up, down, strange, charm, bottom, and top. A quark of each flavor comes in 3 colors and gluons as the generator of the color SU(3) group come in 8 varieties.

All hadronic matter is made of quarks. The idea of quarks came from the fact that the observed spectrum of the lowest mass mesons and baryons required to have physical manifestation for the SU(3) of flavor. The observed baryons are interpreted as three-quark states. To explain the spin states of the low-mass baryons, the quark constituents of the baryons should have half-integral spin. Then the quarks in the spin-$\frac{3}{2}$ baryons are in a symmetrical state of space, spin and SU(3) flavor degrees of freedom, which conflicts with the requirements of Fermi-Dirac statistics: the total antisymmetry of the wave function. The introduction of the color degree of freedom resolves this

dilemma. Each quark carries a color index a with three possible values (red, green, blue for a=1,2,3). This new index makes the baryon wave functions antisymmetric. Since the additional color degree of freedom could lead to a proliferation of states, the color hypothesis has to be supplemented by a requirement that only color singlet states can exist in nature. In the color SU(3) group, with quarks q_a transforming according to the fundamental (3×3 unitary matrix) representation and the antiquarks $\bar{q}^a$ according to the complex conjugate representation, the basic color singlet states are the mesons $q_a \bar{q}^a$ and the baryons $\epsilon^{abc} q_a q_b q_c$, where ϵ^{abc} is the antisymmetric tensor.

The QCD Lagrangian is

$$L_{QCD} = -\frac{1}{4} F^A_{\mu\nu} F^{A\mu\nu} + \sum_{\text{flavors}} \overline{q}_a (i\gamma^\mu D_\mu - m)_{ab} q_b \ . \tag{1.1}$$

The terms in Eq. 1.1 describe the interaction of spin-$\frac{1}{2}$ quarks of mass m and massless spin-1 gluons. Here the notation of Bjorken and Drell is used, with metric given by $g^{\mu\nu} = \text{diag}(1, -1, -1, -1)$ and $\hbar = c = 1$. The gamma matrices satisfy the anticommutation relations,

$$\{\gamma^\alpha, \gamma^\beta\} = 2g^{\alpha\beta} \ , \tag{1.2}$$

and the $F^A_{\mu\nu}$ is the field strength tensor derived from the gluon field $\mathcal{A}^a_\mu$,

$$F^a_{\mu\nu} = [\partial_\mu \mathcal{A}^A_\nu - \partial_\nu \mathcal{A}^A_\mu + g f^{ABC} \mathcal{A}^B_\mu \mathcal{A}^C_\nu] \tag{1.3}$$

where the indices A, B, C run over the eight color degrees of freedom of the gluon field. The third term on the right-hand side of Eq. 1.3 is the non-Abelian term which distinguishes QCD from QED. The triplet and quartic gluon self-interactions and the property of asymptotic freedom come from this term. Since each term in the Lagrangian has mass dimension of four to give the correct dimensions for the action when the Lagrangian is integrated over all space-time, the dimension of the quark field q_a is $\frac{3}{2}$ and the dimension of the gluon field $\mathcal{A}^A_\mu$ is 1.

The sum in Eq. 1.1 runs over the different flavors of quarks and g in the field strength tensor is the coupling constant determining the strength of the interaction between colored quanta. The $f^{ABC}(A, B, C = 1, ..., 8)$ are the structure constants of the SU(3) color group. The quark fields q_a are in the triplet representation ($a = 1, 2, 3$) and D is the covariant derivative. When the covariant derivative acts on triplet fields,

it takes the form

$$(D_\alpha)_{ab} = \partial_\alpha \delta_{ab} - ig\left(\mathcal{A}^C_\alpha t^C\right) \ , \tag{1.4}$$

where t^C are matrices in the fundamental representations of SU(3) group. A representation for the generators t^C is provided by the Gell-Mann matrices, which are hermitian and traceless.

The Eq. 1.1 is invariant under local gauge transformations: The quark fields can be redefined independently at every point in space and time without changing the physical content of the theory. It is worth to notice that the QCD field strength tensor is not gauge invariant due to the self-interaction of the gluon fields. While the photon is electrically neutral as the QED field strength tensor is gauge invariant, the carriers of the color force are themselves colored. On the other hand, similar to QED, there is no gauge invariant way of including a mass term for the gluon fields.

Unlike QED, QCD coupling constant α_s is decreasing at high energies. Conversely, the coupling increases with decreasing energy and thus the perturbation theory cannot be used. As the QCD effective coupling constant α_s decreases as the momentum transfer scale increases, there exists a regime in which $\alpha_s \ll 1$ and this implies a realm in which perturbation theory should be valid. This property is known as *asymptotic freedom*. Asymptotic freedom allows one to make perturbative calculations in α_s only at high energies. Nevertheless, in recent years there has been much progress in understanding and quantifying the predictions of QCD in the nonperturbative region.

Hadrons composed of heavy quarks have masses much heavier than the QCD scale (Λ_{QCD}). This leads to particular kinematic features that allow for specific theoretical techniques which will be discussed in Section 1.2.

1.1.1 Hadron Structure and Parton Distributions

Hadrons are composed of quarks and gluons which are called “partons”. Deep Inelastic Scattering (DIS) provides some of the most precise tests of the theory and determines the momentum distributions of partons in hadrons, for use as input in predicting cross sections in high-energy hadron collisions.

Consider the scattering of a high-energy lepton off a hadron target where the incoming lepton four-momentum is k^μ, the outgoing lepton four-momentum is k'^μ, the

momentum of the target hadron is p^μ, and the momentum transfer is $q^\mu = k^\mu - k'^\mu$. Then the deep inelastic variables can be defined by, $Q^2 = -q^2$, $M^2 = p^2$, $\nu = p \cdot q = M(E' - E)$, $x = Q^2/(2\nu) = Q^2/(2M(E' - E))$, $y = q \cdot p/(k \cdot p) = 1 - E'/E$, where the energy variables are defined in the hadron rest frame and M is the mass of the hadron target. The scattering is mediated by the exchange of a virtual photon when the lepton is an electron or muon.

The structure functions $F_i(x, Q^2)$ are defined in terms of the lepton scattering cross sections and they parametrize the structure of the target as 'seen' by the virtual photon. In the Bjorken limit, $Q^2, \nu \to \infty$, the structure functions are observed to obey an approximate scaling law [1], $F_i(x, Q^2) \to F_i(x)$.

The parton distribution functions are the probability density for finding a particle with a certain longitudinal momentum fraction x at momentum transfer Q^2. The parton distribution functions are determined experimentally.

1.2 Effective Field Theories

Effective field theory (EFT) is a very powerful tool which provides a systematic formalism for the analysis of multi-scale problems. Especially in QCD, where the value of the running coupling constant α_s can significantly change in different energy scales, it is very important.

The basic idea behind EFT lies in the fact that to calculate observables of an interesting (low) energy region, one can integrate out the degrees of freedom of other regions. This simplifies calculations and the calculations gives equivalent physical result to the fundamental QCD calculations in that energy region.

The Heavy Quark Effective Theory (HQET) is a typical example of EFT for heavy quarks. It provides a simplified description of systems with a single heavy quark interacting with light partons. Two energy scales, the scale of the mass m and Λ_{QCD}, are the main characteristics of these systems. In HQET, the scale m is integrated out and the theory is expanded in powers of Λ_{QCD}/m. For bound states made of two heavy quarks, additional scales need to be introduced. Integrating out the scale m leads to an EFT, Nonrelativistic QCD (NRQCD) [2, 3]. In the next section NRQCD for the heavy quarkonium will be briefly discussed, since it is the framework on which many contemporary applications are based.

1.2.1 Heavy Quarkonium and NRQCD

Heavy Quarkonium is a meson composed of a heavy quark and its antiquark pair. The scales of quarkonium include the mass m of the heavy quark, momentum transfer mv, and kinetic energy of the quark and antiquark in the center-of-mass frame mv^2. The quark mass m sets the total energy scale for annihilation decays and the scale of the kinematic threshold for quarkonium production. The inverse of the momentum mv is the length scale for the size of the quarkonium state. And the kinetic energy mv^2 is the scale of the splittings between radial excitations and orbital angular momentum excitations in the quarkonium spectrum. Another important energy scale in quarkonium physics is Λ_{QCD} which is the scale of nonperturbative effects involving gluons and light quarks. By definition, the heavy quark mass m is large in comparison with the hadronic scale Λ_{QCD}. Hence, processes at scale m are expected to be successfully described by perturbation theory, due to the asymptotic freedom of QCD.

NRQCD is designed to describe the dynamics of a heavy quark and antiquark pair at energy scale $\hat{s}$ in the center-of-mass frame much smaller than their masses (which are much larger than Λ_{QCD}). NRQCD introduces a single ultra-violet (UV) cut-off $\nu_{NR} = \nu_p, \nu_s$ satisfying $mv, mv^2, \Lambda_{QCD} \ll \nu_{NR} \ll m$, where ν_p is the UV cut-off of the relative three-momentum of the heavy quark (antiquark) and ν_s is the UV cut-off of the energy of the heavy quark (antiquark) and the four-momentum of the gluons and light quarks. Since $\nu_{NR} \gg \Lambda_{QCD}$, energy fluctuations about the heavy quark (antiquark) mass and three-momentum fluctuations up to the scale ν_{NR} for the heavy quark (antiquark) fields and four-momentum fluctuations up to the same scale for the fields of the light quarks can be integrated out perturbatively in $\alpha_s(\nu_{NR})$. Even though the high-energy modes have been integrated out, they still have a relevant effect on the low-energy part. This effect is encoded into the matching coefficient and new local interactions of the NRQCD Lagrangian.

Since $Q\overline{Q}$ production arises at momentum scales of order m or larger, it can be accounted by contact interactions in NRQCD. Consequently, the inclusive cross section for the direct production of the quarkonium at large transverse momentum (p_T of order m or larger) in hadron or ep colliders or at large momentum in the CM frame (p^* of order m or larger) in e^+e^- colliders can be expressed as a sum of products of

NRQCD matrix elements and short-distance coefficients.

$$\sigma[\psi] = \sum_n \sigma_n(\Lambda)\langle\mathcal{O}_n^\psi(\Lambda)\rangle \ , \tag{1.5}$$

where Λ is the ultraviolet cutoff of the effective theory, the σ_n are short-distance coefficients, and the $\langle\mathcal{O}_n^\psi(\Lambda)\rangle$ are vacuum expectation values of four-fermion operators in NRQCD. The short-distance coefficients σ_n in Eq. 1.5 are essentially the process-dependent partonic cross sections to make a $Q\overline{Q}$ pair convolved with parton distributions, and the coefficients are determined by matching the square of the production amplitude in NRQCD to full QCD. This matching can be carried out in perturbation theory since the scale of the $Q\overline{Q}$ production is of order m or greater. The vacuum matrix element of the four-fermion operators in Eq. 1.5 is the probability for a $Q\overline{Q}$ to form a quarkonium plus anything. These matrix elements include all the nonperturbative physics associated with evolution of the $Q\overline{Q}$ pair into a quarkonium state. The matrix elements are "universal", *i.e.*, process independent and this important property increases the predictive power of NRQCD remarkably.

The operators can be counted in v, and the v and α_s are the two small expansion parameters of NRQCD. For an accuracy of order $(\alpha_s^i v^j)$, only the matching coefficients that contributes up to the same order need to be kept. The couplings will be determined by the requirement that NRQCD reproduces the results of QCD up to order $(\alpha_s^i v^j)$.

1.3 Charmonium Production and Polarization

Since the discovery of J/ψ , quarkonium physics has provided a unique laboratory for testing our understanding of QCD at the interface of the perturbative and nonperturbative regimes which describe the physics of heavy-quark creation and bound state formation respectively.

The charm quark and anti-charm quark bound states are the first bound systems of quarks to which QCD could be applied as a perturbation theory. The charm quark mass ($m_c \approx 1.3$ GeV) sets a mass scale high enough to approach the asymptotically free regime. The two small expansion parameters of NRQCD for heavy quarkonium are [4] : $\alpha_s(m_c) \approx 0.25$ and $\alpha_s(m_b) \approx 0.18$, $v^2 \approx 0.3$ for charmonium, and $v^2 \approx 0.1$ for bottomonium. With a reasonable truncation of the expansion having not too many

adjustable parameters to have any predictive power, the expansion uncertainty of charmonium production is larger than that of bottomonium and the mv^2 of charmonium may be smaller than Λ_{QCD} [**?**]. Although the perturbative method is still applicable to charmonium, this may indicate a need for different theoretical approaches for charmonium and bottomonium in perturbative calculations.

In analogy to positronium, the $c\overline{c}$ bound states are named charmonium. The charmonium system has rich spectra of orbital and angular momentum excitations as shown in Fig. 1.1. Experimentally, the most clean signatures are provided by the $J^{PC} = 1^{--}$ states (J/ψ(1S) and ψ(2S)) and they have been a particularly important test stand for studying the physics of heavy quarks.

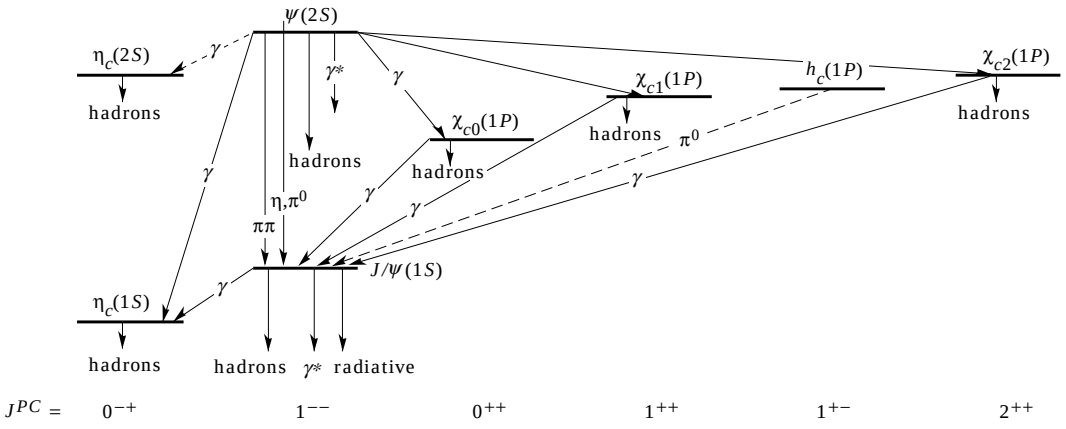

Figure 1.1: The Charmonium System [5].

The earliest prediction for quarkonium production was the color-singlet model (CSM) [6]. CSM is inspired by the factorization theorem of QCD in which the hard part is calculated by the application of perturbative QCD and the soft part is factorized in a universal wave function. The six diagrams for the ${}^3S_1$ states production associated with a gluon are shown in Fig. 1.2.

In 1994, CDF experiment at Tevatron released a preliminary result of J/ψ and ψ(2S) production cross section [7] and it turns out that the CSM under-predicts the prompt cross section of in $p\overline{p}$ collisions by more than an order of magnitude as shown in Fig. 1.3.

This large discrepancy was referred to ψ' anomaly. Since then there have been many theoretical efforts to explain the anomaly. One of the successful formalism was the NRQCD factorization including color-octet mechanism. Some of those models will

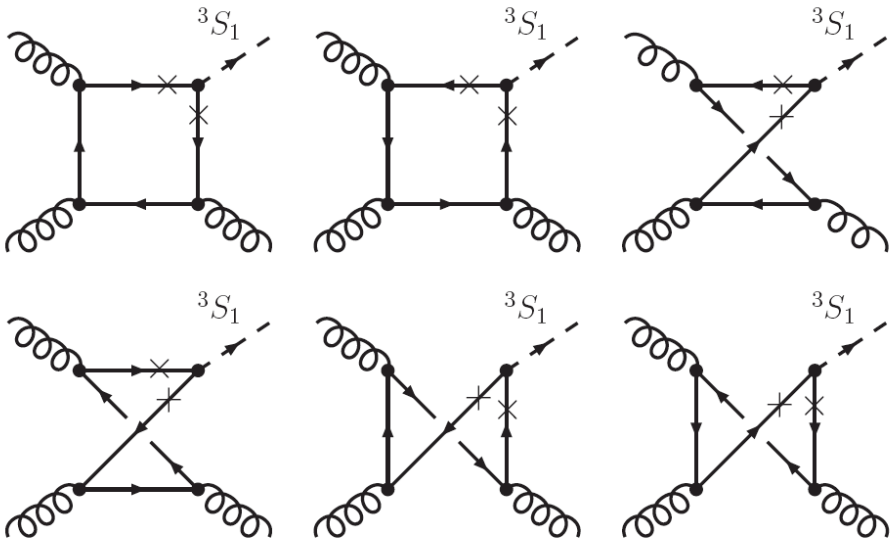

Figure 1.2: The six Feynman diagrams for the $^3S_1$ states at LO within the CSM.

be discussed in below [1].

1.3.1 NRQCD factorization

NRQCD factorization approach basically separates short-distance effects involving momenta of order m or larger from those effects that involve the smaller momentum scale mv, mv^2, and Λ_{QCD}. The scale m is assumed to be perturbative, so that short-distance effects can be calculated using perturbation expansion in $\alpha_s(m)$. It exploits the fact that in a nonrelativistic bound state, the typical velocity v provides a small expansion parameter.

In this model the $Q\overline{Q}$ pair can be produced in a color-singlet state or a color-octet state. The spin state can be singlet or triplet. The matching of the square of the production amplitude in NRQCD to full QCD determines the short-distance coefficients. The color-octet matrix elements have the interpretation of the probability to find the quarkonium in a Fock state consisting of a $Q\overline{Q}$ pair plus numbers of gluons. In the leading order color-octet production mechanisms the gluons are emitted during the subsequent hadronization process. As discussed in Section 1.2.1, non-perturbative parameters are universal and can be applied not only at the Tevatron but also for HERA

[1] This does not mean to be a thorough review of contemporary quarkonium models.

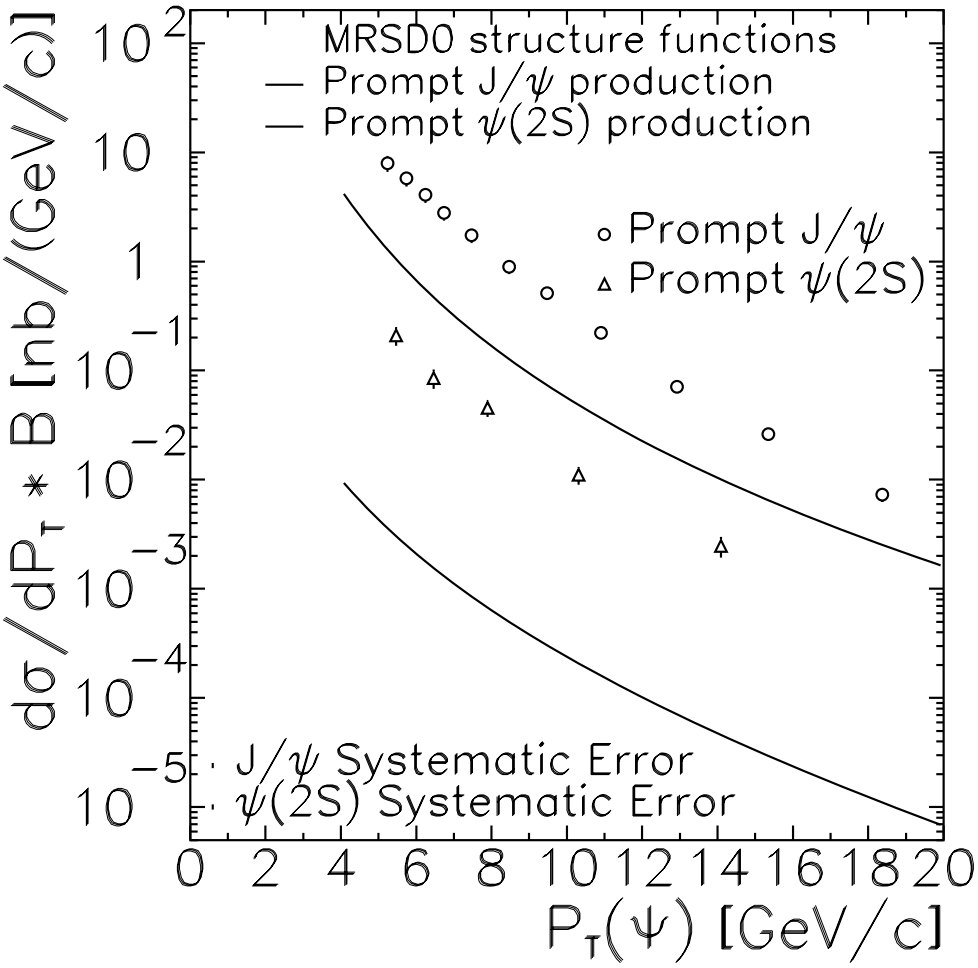

Figure 1.3: The differential cross section times branching ratio for prompt ψ mesons with the theoretical expectations based on the CSM[15].

and even in a fixed target experiment.

Sometimes the NRQCD factorization approach is called the "color-octet model" in a mistaken manner. Even though color-octet terms are expected to dominate in some situations, there are also situations in which color-singlet terms are expected to dominate. The NRQCD is a rigorous consequence of QCD in the limit $\Lambda_{QCD}/m \to 0$.

The polarization of an 1^{--} state, like $\psi(2\mathrm{S})$ can be measured from the angular distribution of its decays into lepton pairs. The NRQCD factorization approach has a simple prediction for the polarization at large transverse momentum. Gluon fragmentation is the dominant process in the production of a quarkonium with p_T much

larger than the quarkonium mass [8]. In this process the quarkonium is formed in the hadronization of a gluon that is created with an even larger transverse momentum. The fragmenting gluon is nearly on its mass shell at large p_T and thus it is transversely polarized. The gluon fragmentation into a $Q\overline{Q}$ pair in a color-octet ${}^3S_1$ state is the dominant gluon-fragmentation process in the NRQCD factorization approach [9, 10]. The presence of the color-octet production mechanism could be tested by the measurement of the quarkonium states.

1.3.2 k_T-factorization

At modern hadron colliders such as Tevatron, the production of quarkonium can be initiated by partons with low momentum (a few percent of the hadron). In other words, the properties of parton distributions in the small x region describes the dynamics of interactions. This domain can be characterized by energy scales, $\Lambda_{QCD} \ll \hat{s} \simeq \mu^2 \ll s$, where μ denotes the typical parton interaction scale which is the order of the subprocess invariant energy $\sqrt{\hat{s}}$. In this "semihard" condition, the perturbation expansion in α_s may contain large coefficients $O[\ln(s/\mu^2)] = O[\ln(1/x)]$ which increase fast and therefore including only a few calculable terms in the perturbative expansion would not be sufficient.

The large logarithmic contributions of the type $\alpha_s[\ln(1/x)]^n$ need to be resummed. This resummation is done in the k_T-factorization approach [11–14] in which the incoming t-channel gluons have a finite transverse momentum k_T and are off mass shell. The resummation of the terms $[\ln(\mu^2/\Lambda^2_{QCD})\alpha_s]^n$, $[\ln(\mu^2/\Lambda^2_{QCD})\ln(1/x)\alpha_s]^n$, and $[\ln(1/x)\alpha_s]^n$ leads to the unintegrated parton distributions $\mathcal{F}_i(x, k_T^2, \mu^2)$, which determine the probability of finding a parton of type i carrying the longitudinal momentum fraction x and transverse momentum k_T at the probing scale μ^2. The unintegrated parton distributions are described by certain evolution equations, *e.g.*, Balitskiĭ-Fadin-Kuraev-Lipatov (BFKL) or Ciafaloni-Catani-Fiorani-Marchesini (CCFM) equation. By integrating out the k_T dependence, the conventional Dokshitzer-Gribov-Lipatov-Altarelli-Parisi (DGLAP) densities can be obtained from the unintegrated parton distributions.

One of the noticeable aspects of the k_T-factorization approach is that the off-shell gluons can have longitudinal components in the spin density matrix and thus affect the quarkonium polarization properties.

1.3.3 Gluon tower: enhanced NNLO contributions

The production of ${}^3S_1$ charmonium states through gluon-gluon fusion always requires an additional gluon in the final state to form the color-less mesons. The C-parity conservation also prohibits this additional gluon from being in the initial states. The CSM provided the most natural and simplest process to produce a color-octet quark-antiquark pair ($gg \rightarrow c\overline{c}$) and to emit an additional gluon carrying the color away. However, as discussed earlier, the CSM cross section prediction at leading order (LO) was more than an order of magnitude lower than the Tevatron measurement [15] as the process is suppressed by the small QCD coupling α_s.

An additional gluon attached to the heavy quark loop is considered by V.A. Khoze *et al.* [16] as shown in Fig. 1.4. Although the contributions containing an extra loop in cross section are suppressed by the small QCD coupling α_s, they investigated the possibility that the α_s suppression is compensated by the large number of possible graphs where the additional gluon is absorbed by different parton spectators. Since the parton multiplicity n is proportional to $\log s$, this process can be considered as the LO amplitude in the BFKL approach. In collinear approximation, this amplitude corresponds to the next-to-next-to-leading order (NNLO) contribution in the cross section. At high energies, they found that this contribution would be enhanced.

The extra gluon exchange considered in their calculation was hidden in the value of the non-perturbative matrix element $\langle \mathcal{O}_n^{\psi}(\Lambda) \rangle$ in the case of the color-octet mechanism where the charmonium meson is formed from the color-octet $Q\overline{Q}$ pair after the non-perturbative interaction included in the $\langle \mathcal{O}_n^{\psi}(\Lambda) \rangle$ matrix element.

Their calculation of the amplitude is similar to the computation of the amplitude for diffractive J/ψ photoproduction [17] and they also allowed for the emission of secondary s-channel gluons from the symmetric octet (gg) additionally encouraged by the successful adaptations of the BFKL approach on the HERA data. They also considered an alternative possibility of creating a color-octet $c\overline{c}$ pair, which then transforms to a color singlet by re-scattering via gluon exchange. This mechanism, in which two gluons in a symmetric color-octet t-channel state, $(gg)_{8s}$, belong to two different Pomerons, has smaller contribution than their main processes at the Tevatron energy but it may dominate at asymptotically large energies.

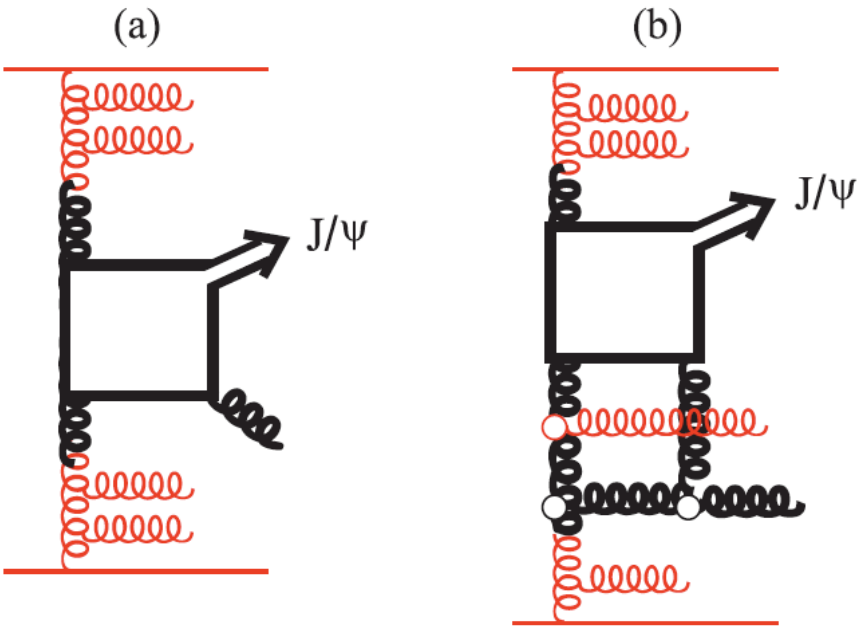

Figure 1.4: (a) LO perturbative QCD in the CSM (b) NNLO perturbative QCD or LO BFKL contributions [16].

1.4 The $\psi(2S)$ Production Cross section and Polarization

There have been many theoretical efforts to understand the production mechanism of quarkonium since the discrepancy between CSM and the Tevatron measurement. The NRQCD factorization approach succesfully matched the measured cross section with universal parameters extracted from the data. An unavoidable consequence of the NRQCD factrorization method is that the dominant contribution of on-shell gluons at larger p_T results in a prediction of transversely polarized prompt states. The CDF Run I measurement of J/ψ and $\psi(2S)$ polarization had not perfectly agree with the transversely polarized states at larger p_T but the measurement was statistically not strong enough to be conclusive [18]. It is also worth to note that directly-produced $\psi(2S)$ states are not populated from other charmonium decays while the prompt J/ψ states can be produced either directly or via the decay of χ_c or $\psi(2S)$ parent states.The measured polarization compared to the theory prediction is shown in Fig. 1.5.

On the other hand, there have been experimental improvements with more ad-

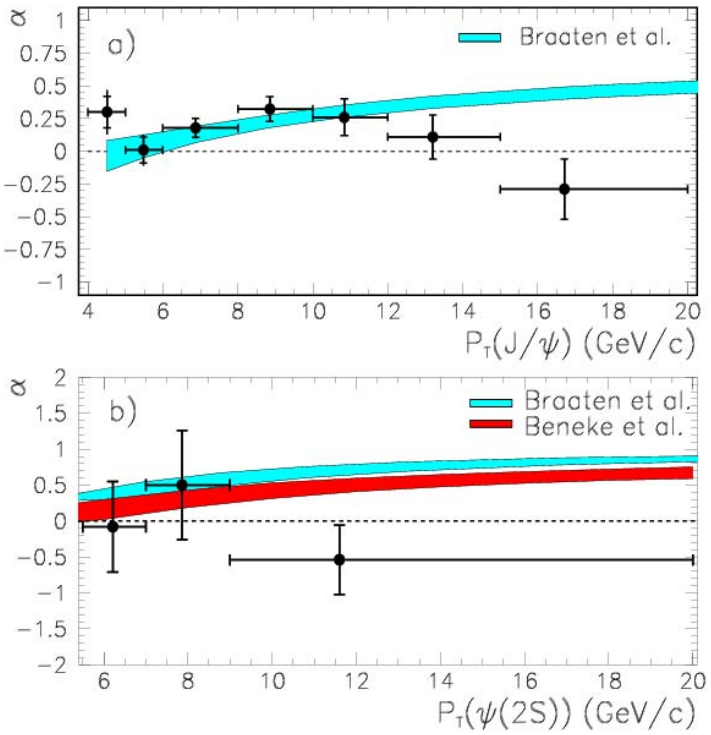

Figure 1.5: The CDF Run I measurement of J/ψ and $\psi(2S)$ polarization[18].

vanced experimental instruments, and much more data have been accumulated with much better understood detector performance.

The newly measured $\psi(2S)$ production cross section and polarization results will be addressed in this thesis, which would provide a further test on existing theory models and shed light on quarkonium hadroproduction mechanism.

Chapter 2

Experimental Apparatus

"Every day I remind myself that my inner and outer life are based on the labors of other men, living and dead, and that I must exert myself in order to give in the same measure as I have received and am still receiving."

— Albert Einstein 1879–1955

The Collider Detector at Fermilab (CDF) is a multi-purpose detector installed at the Fermi National Accelerator Laboratory (Fermilab or FNAL). The CDF detector has been updated to CDF II. The data used in these analyses were collected by CDF II detector. In this chapter, a synopsis of the accelerator complex and the detector, concentrating on those components of the detector with the most impact on the $\psi(2S)$ production cross section and polarization analyses.

2.1 The Tevatron

The Tevatron is currently the highest energy accelerator in the world. Its name is derived from the the phrase "tera electron volt" or TeV, which means one trillion electron volts. Although the normal operation energy for Run II is 980 GeV, the Tevatron has achieved an energy as high as 1.012 TeV during accelerator studies. The accelerator is located in a tunnel with a radius of 1 km. As a superconducting magnet synchrotron, all dipoles, quadrupoles, and correction element magnets are cooled to about 4.6 K with liquid Helium.

In the early 1980's, the Tevatron was built at the Fermilab in Batavia, Illinois, USA. The Tevatron was designed to accelerate protons and antiprotons to one TeV of energy. The Tevatron was operated at center of mass energy of 1.8 TeV for Run I. Between September 1997 and March 2001, both the accelerator complex and the collider detectors underwent major upgrades and Run II has been operated at the center of mass energy of 1.96 TeV. Run II is scheduled to last until the end of Fiscal Year 2009 with an integrated luminosity goal of 8 fb^{-1}. Early in 2007, the Tevatron had already delivered over 2 fb^{-1} of integrated luminosity with a record initial luminosity of 2.85×10^{32} cm^{-2} s^{-1}.

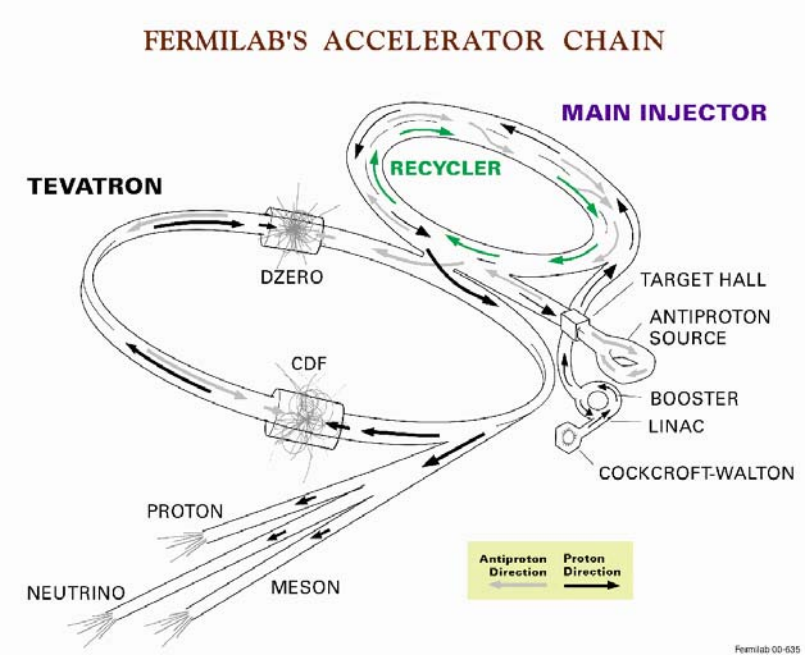

Figure 2.1: Diagram of the Fermilab accelerator chain.

A diagram of the Fermilab accelerator chain is shown in Fig. 2.1.

The Fermilab accelerator systems are composed of the Pre-accelerator, Linac, Booster, Main Injector, Recycler, Tevatron, Debuncher and Accumulator. The first three systems are known as the proton source and the last two machines are referred to as the antiproton source. The first accelerator, Pre-accelerator is the source of the negatively charged hydrogen ions. In the Pre-accelerator, the H^- ions are produced by electrical discharges and accelerated in the Cockroft-Walton up to an energy of 750 keV. Then the beam travels through a transfer line called the 750 keV line until it enters the Linac. The Linac is a 500 foot long linear accelerator. It takes the ions and accelerates them

to an energy of 400 MeV. The continuous beam of H^- ions from the Pre-accelerator is separated into bunches by the AC nature of the Linac. The Booster is the next level of acceleration. It is approximately 75-meter radius proton synchrotron with an injection energy of 400 MeV and an extraction energy of 8 GeV. The Booster strips the electrons off from the H^- ion using a thin carbon foil and leaves only the proton. These protons are sent to either the Main Injector or the MiniBooNE experiment which uses 8 GeV protons to produce a neutrino beam. The Main Injector accepts 8 GeV particles from the Booster or the antiproton source and accelerates them to 150 GeV, and accelerates 120 GeV protons for antiproton production. In the antiproton source, the 120 GeV proton beam strikes the nickel alloy target and produces a shower of secondary particles. The antiprotons are produced through the interaction $p + p \rightarrow p + \overline{p} + p + p$. At Fermilab, it takes $10^5 - 10^6$ protons to make an antiproton. In order to collect the antiprotons from the secondary particles, a lithium lens is used to focus the particles followed by a pulsed dipole magnet in which the negatively charged particles with the proton mass will bend at the correct angle to be delivered to the Debuncher with an energy of approximately 8 GeV. In the Debuncher, the momentum spread of the antiproton beam is reduced through bunch rotation and adiabatic debunching. Beam cooling is a technique to reduce the physical size and energy spread of a particle beam circulating in a storage ring without any loss of the beam. A stochastic cooling which is named because of the stochastic nature of the beam has been playing the major role of beam cooling at Fermilab. It reduces both the beam size and momentum spread. The stochastic cooling samples a motion of a particle and corrects the motion. It is similar to other beam feedback systems used on accelerators except that the stochastic cooling system works on individual particle amplitudes. Every particle has a slightly different frequency of motion, and the force generated by all the other particles has a random phase and thus averages to zero. The net result is that a damping force created by each particle linear in the system feedback gain describes cooling of each particle, and the heating force created by all the other particles averages to zero to first order in the feedback gain but causes particle diffusion proportional to the gain squared. The transverse size of a beam can be reduced by betatron or transverse cooling. Betatron cooling senses the particle displacements in the pickup and applies a correcting signal at the kicker. The pickup and the kicker are placed 90° apart in betatron phase so that a position displacement at the pickup will become an angular displacement at the kicker. The momentum cooling system reduces the longitudinal energy spread of a beam by accelerating or decelerating particles in the beam distribution towards a central momentum. In a momentum cooling system, the pickup signals are applied to the

kicker electrodes providing longitudinal fields to accelerate or decelerate the passing particles.

The Accumulator is a triangular-shaped synchrotron of radius 75-meter which accepts the antiproton beam from the Debuncher. In the accumulator, the antiprotons are stored at 8 GeV and cooled until they are injected into the Recycler in the Main Injector. The Recycler cools the antiproton beam further than the Accumulator is capable. It uses both a stochastic cooling system and an electron cooling system. Electron cooling uses a heat exchange between the antiproton beam and the electron beams with much less variation in transverse kinetic energy The antiproton beam is stored at a constant kinetic energy of 8 GeV and transferred to the Tevatron for collisions.

The largest of the Fermilab accelerator, the Tevatron is a circular superconducting synchrotron with eight accelerating cavities. The Tevatron accepts both protons from the Main Injector and antiprotons from either the Accumulator or the Recycler and accelerates them from 150 GeV to 980 GeV. At this energy, one full revolution takes about 21 μs. Being the only cryogenically cooled accelerator at Fermilab, the magnets used in the Tevatron are made up of a niobium/titanium alloy which needs to be kept ~ 4 K to remain a superconductor. In the current collision mode, 36 bunches of protons and antiprotons are colliding each other every 396 ns. At two collider experiments (CDF and DØ) located in the Tevatron, the proton and antiproton beams are focused by quadrupole magnets to a width of approximately 35 μm for collisions. As the bunch width is sharply focused at the collision sites, the length of each bunch is de-focused consequently. The typical bunch size is about 35 μm wide and 30 cm long.

2.2 The Collider Detector at Fermilab

The $\psi(2\mathrm{S})$ production cross section and polarization analyses use data accumulated by the CDF II detector which is an azimuthally and forward-backward symmetric particle detector for the study of $p\overline{p}$ collisions in the Tevatron. A comprehensive description of the CDF II detector can be found in Ref. [19].

The CDF II detector is a general purpose solenoidal detector in which precision charged particle tracking with fast projective calorimetry and fine grained muon detection are combined. By using the CDF II detector, we can make many different precise measurements and search for new particles and new physics. The Run II detec-

tor upgrades include several important changes [20]: the replacement of the central tracking systems, the replacement of a gas sampling calorimeter with a scintillating tile calorimeter in the plug region, the addition of pre-shower detectors and a time-of-flight detector, extended coverage of muon detectors, and improved trigger, readout electronics, and data acquisition systems. The CDF collaboration is a multi-national collaboration of over 800 physicists from more than 60 institutions. The CDF II detector in an elevation view is shown in Fig. 2.2. The different aspects of each detector components will be described in following sections.

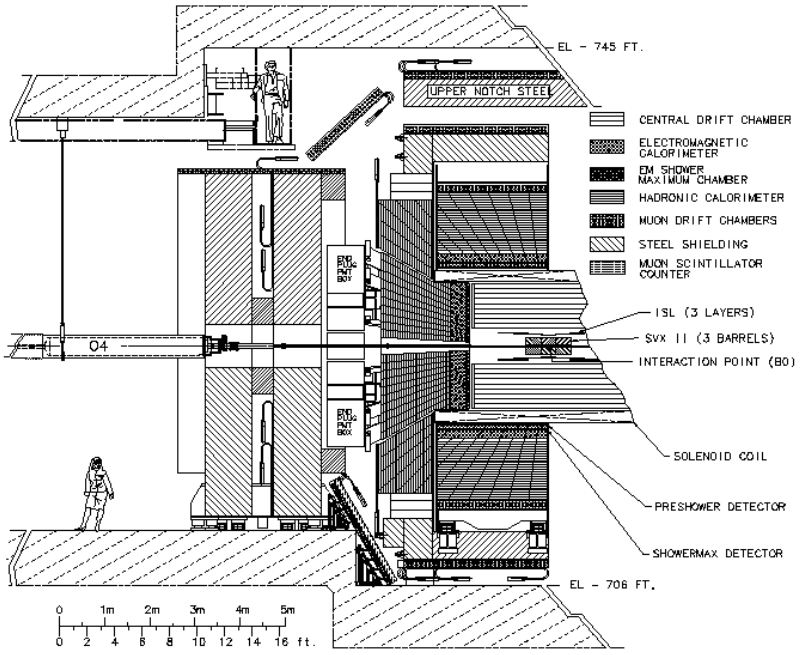

Figure 2.2: An elevation view of one half of the CDF II detector. The detector is roughly three stories tall .

2.2.1 The CDF II Detector

The CDF II detector is forward-backward symmetric with respect to the $p\overline{p}$ interaction point and also cylindrically symmetric around the beamline. In the coordinate system used in the CDF II, the polar angle θ is measured from the proton direction, the azimuthal angle ϕ is measured from the Tevatron plane, and the pseudo-rapidity is defined as $\eta \equiv \tanh^{-1}(\cos\theta)$. There are independent subsystems in the CDF detector and each of the subsystems is designed to measure the properties of physical objects

produced by the collision. A detailed description of the subsystems can be found in the CDF II technical design report[19].

Tracking Systems

The state of the art of the CDF analysis technique is primarily based on efficient, precision charged particle tracking. Some of the applications of charged particle tracking at the CDF II include efficient, precise reconstruction of track momentum at both high and low transverse momentum, efficient electron and muon identification with high purity by combining tracks with information from calorimeter or muon chambers, precise reconstruction of track impact parameter, and the precise reconstruction of the interaction vertex z coordinate. The tracking system is located in the center of the CDF II detector system around the beamline.

The Run II tracking system is composed of a large open cell wire drift chamber at large radii and a silicon microstrip detector inside the drift chamber. The whole tracking system is placed in a superconducting solenoid which typically operates at 4650 A to produce a relatively uniform field of about 1.4 T along the proton direction. The overall length of the solenoid is 5 m, inner bore is 2.86 m, and outer diameter is 3.35 m. A schematic view of the CDF II tracking system is shown in Fig. 2.3.

Inner Tracker

A semiconductor detector has a much higher resolution in tracking charged particles than wire chambers. Silicon is in particular popular due to its commercial applications, unmatched energy and spatial resolution, and has excellent response time. When a charged particle penetrates a semiconductor such as silicon, it will ionize in the bulk of the material and produce electron-hole pairs along its trajectory. The pairs are separated by an externally applied electric field before they recombine. The electrons drift towards the anode and the holes drift to the cathode. Then the charge is collected by the electrodes.

There are two types of semiconductor, “n-type” and “p-type”. The n-type silicon can be made by adding atoms of another element having more electrons than silicon and the p-type silicon with atoms having fewer electrons. When p-type and n-type silicons are combined together in very close contact, a pn junction is formed. Silicon detectors

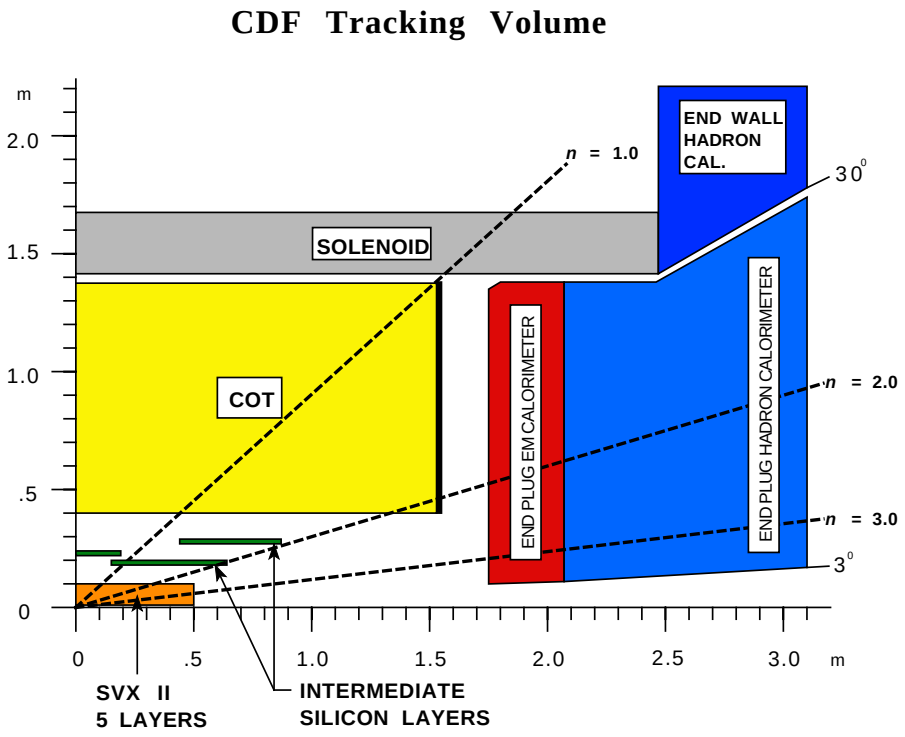

Figure 2.3: A longitudinal view of the CDF II tracking systems. .

are asymmetric pn junctions: on top of the bulk silicon (usually n-type), strips of the other type (usually p-type) are applied. To work as a detector, the silicon sensor are depleted by applying a voltage across the sensor. The electrons produced by charged particles in the silicon sensor drift through the bulk towards the strips on top.

The low energy threshold determines the intrinsic energy resolution. To produce an electro-hole pair, only 3.6 eV are necessary for silicon detectors while the ionization energy in gas is 30 eV. The high density of silicon reduces the range of the secondary electrons and thus yields a good spatial resolution.

The CDF II inner tracker system is composed of of three subsystems, Layer 00 (L00), Silicon Vertex (SVX II), and Intermediate Silicon Layer (ISL) detectors[21]. An end view and a diagram of the silicon subsystems are shown in Fig. 2.4.

In the original CDF II technical design, the L00 silicon detector[22] was not considered. Later on, to improve the impact parameter resolution on tracks and the efficiency of tagging jets from b quark production[22], the L00 has been installed. The L00 consists of 48 single-sided, radiation-tolerant silicon strips detectors which employs Large Hadron Collider (LHC) designs for sensors supporting high-bias voltages. It has been

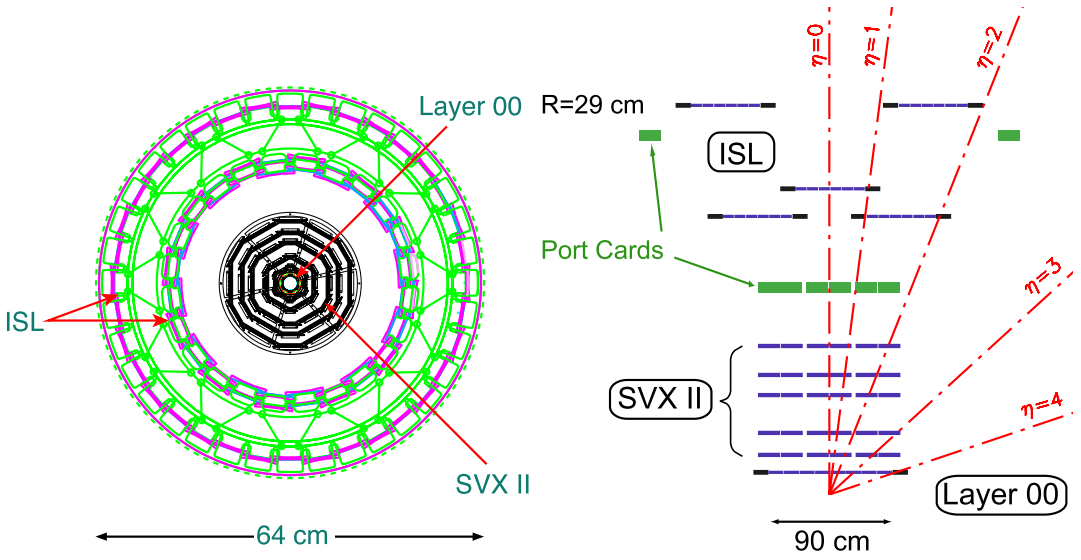

Figure 2.4: Left: End view of the CDF II inner tracker system, with all three silicon subsystems labeled. Right: Side view of the upper half of the CDF II silicon system. The scale of the z-coordinate is highly compressed in the figure.

assembled around the beryllium beampipe inside of the SVX II. The strips sensors are 25 μm pitch and 8 μm wide. The readout pitch is 50 μm since only alternating strips are used. The silicon wafers have two different widths, 8.4 and 14.6 mm and these wafers are interleaved in a 12-sided pattern as shown in Fig. 2.5. The L00 is located at a radius of 1.5 cm from the beamline and 90.0 cm long. The silicon wafers are cooled to -10 °C to reduce the flow of free charge carriers and prolong the life of the detector.

The five double-sided silicon microstrips layers of the SVX II detector are located around the L00 detector. The SVX II layers extends from a radius 2.44 cm from the beamline to 10.6 cm. The SVX II detectors are double-sided to provide $r-z$ readout for improved pattern recognition and 3-D vertex reconstruction. The impact parameter resolution of the combination of the SVX II and ISL is 40 μm including 30 μm contribution from the beamline and the z_0 resolution is 70 μm. In double-sided detectors, one side has strips parallel to the axial direction providing $r-\phi$ information while the other side has strips at an angle (stereo angle) with respect to the axial direction providing the axial position information. To optimize both vertex resolution and pattern recognition, the first, second and fourth layers have a "90 ° stereo" design while a "small angle stereo" design is applied to the third and fifth layers. The "90 ° stereo" sensors have strips running in the axial direction on the pn junction side of the sensor and strips running laterally on the ohmic contact side to measure the $r-\phi$ position

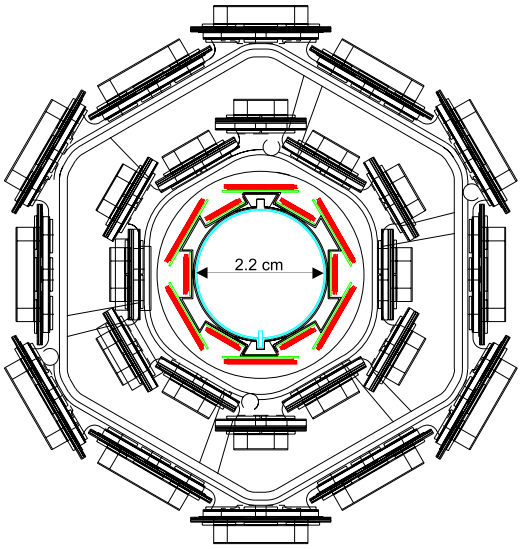

Figure 2.5: End view of the L00 silicon detector surrounded by the two inner layers of the SVX II detector.

of the particle and the $r-z$ position correspondingly. The mechanical parameters of the SVX II are summarized in Table 2.1. The SVX II is composed of three cylindrical barrels which supports five layers. In each layer, the silicon wafers are arranged in ladders which are four-wafer long. The SVX II detector system is cooled to -10 °C.

Property	Layer 0	Layer 1	Layer 2	Layer 3	Layer 4
number of ϕ strips	256	384	640	768	896
number of Z strips	256	576	640	512	896
stereo angle	90°	90°	+1.2°	90°	-1.2°
ϕ strip pitch (μm)	60	62	60	60	65
Z strip pitch (μm)	141	125.5	60	141	65
total width (mm)	17.140	25.594	40.300	47.860	60.170
total length (mm)	74.3	74.3	74.3	74.3	74.3
active width (mm)	15.300	23.746	38.340	46.020	58.175
active length (mm)	72.43	72.43	72.38	72.43	72.38

Table 2.1: The SVX II detector mechanical parameters.

The ISL detector is located between the SVX II and the drift chamber as shown in Fig. 2.4. The similar technology used in the SVX II is applied for the ISL. A layer of

double-sided silicon sensors is placed at a radius of 22 cm in the central region and two layers are placed at radii of 20 cm and 28 cm in the region $1.0 \leq |\eta| \leq 2.0$. Both $r - \phi$ and a small angle stereo measurement can be made by all three layers. The ISL is cooled to +6 °C. Radiation damage to the ISL is smaller than for the inner systems because the ISL layers are located at larger radii than the L00 and the SVX II.

Central Outer Tracker

The tracking at large radii in the central region $|\eta| \leq 1.0$ is done with a large open cell drift chamber. The central outer tracker (COT) [23] reconstructs charged particles in the central region. When charged particles enter a wire drift chamber, they ionize the gas inside the chamber and thus produce free electrons. These electrons drift from the cathode (field wires) and toward the anode (sense wires) in an electric field. The maximum drift time is designed to be less than the 132 ns bunch spacing.

The cylindrical COT covers a radial span beginning at 43.4 cm and ending at 132.3 cm and the entire azimuth angle with a total length of 310 cm. A 50:50 mixture of argon and ethane gas is filled in the COT volume. There are 8 superlayers each consists of 12 sense wires in the COT. The axial superlayers are labeled with even numbers (2,4,6, and 8) and the stereo superlayers which are at ± 2 ° stereo to the z-axis with odd numbers (1,3,5, and 7). Each superlayer is divided into "super cells" in ϕ with one wire plane and one field plane on each side, and each supercell contains 12 sense wires. The superlayer geometry of the COT is summarized in Table 2.2. The COT provides accurate measurement of transverse momentum from the $r-\phi$ view and substantially less accurate for the measurement of the pseudo-rapidity. The resolution of hit position is approximately 140 μm and the momentum resolution $\sigma(p_T)/p_T^2 = 0.0015\ (\text{GeV}/c)^{-1}$.

Property	SL 1	SL 2	SL 3	SL 4	SL 5	SL 6	SL 7	SL 8
Stereo Angle (°)	+2	0	-2	0	+2	0	-2	0
Number of cells	168	192	240	288	336	384	432	480
Radius (cm)	46.774	58.534	70.295	82.055	93.815	105.575	117.335	129.096

Table 2.2: A summary of the COT superlayer geometry.

Since the COT is in a magnetic field, the drift-time relation is complicated. This

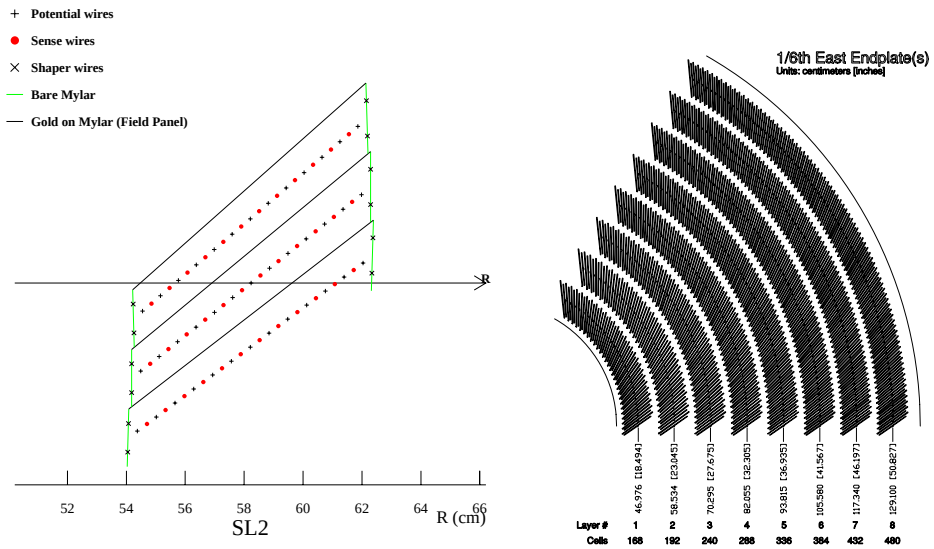

Figure 2.6: Left: Nominal cell layout for superlayer 2 in the central outer tracker (COT) wire drift chamber. Other superlayers (including the stereo layers) are similar except for the taper. Right: Arrangement of cells on the COT endplate.

is accounted by the drift angle (Lorentz angle). At the drift field of ~ 2.5 kV/cm, the cells are tilted at the Lorentz angle of 35 $^\circ$. This also makes the tracking efficiency higher for the low momentum tracks bend in the same direction as the cells as they would cross more wires. The cell layout for the superlayer 2 is shown in Fig. 2.6 along with the arrangement of cells on the endplate. The dE/dx information for the reconstructed tracks can also be provided by the COT.

Time-of-Flight System

The time-of-flight (TOF) system is located between the COT the superconducting magnetic coil as shown in Fig. 2.7. The TOF system consists of 216 bars of plastic scintillators which are about 300 cm in length with a cross section of 4×4 cm. The scintillators are arranged into a barrel shape around the COT. The fine-mesh photomultipliers are used since the TOF system is inside the magnetic field volume. The TOF can distinguish kaons and pions for momenta less than 1.6 GeV/c by a 2 standard deviation. The energy loss dE/dx measured in the COT and the TOF measurement are used for particle identification.

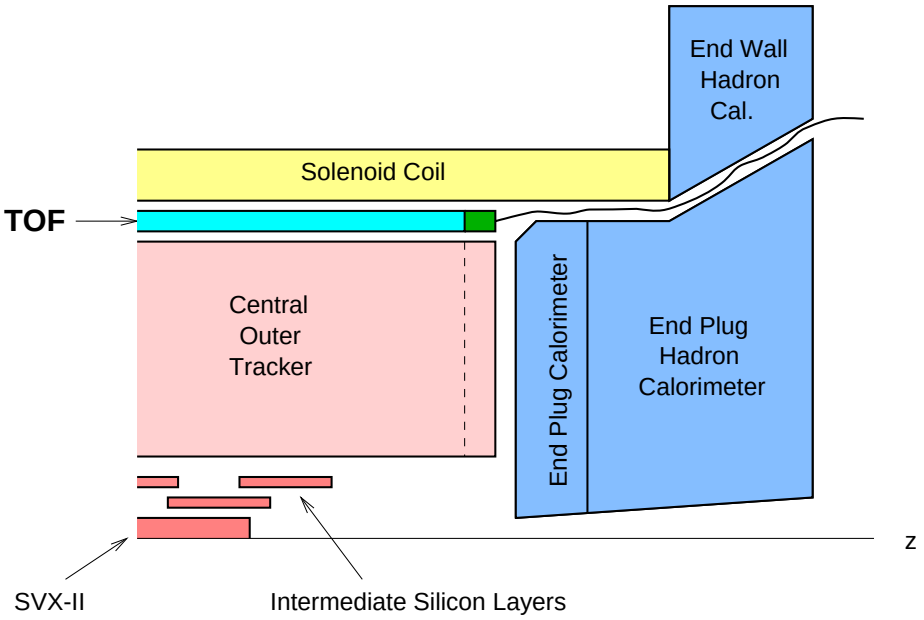

Figure 2.7: The location of TOF system inside CDF II detector.

Calorimeter Systems

The scintillator-based calorimeter system is located outside of the solenoid to measure the energy and position of incident particles or jets using total absorption of particles . The CDF II calorimeter systems use sampling calorimeters. In sampling calorimeters the particle absorption and the signal readout are separated, which allows optimal choice of absorber materials and a certain freedom in signal processing. When particles interact in the absorber, "showers" are generated by cascades of interactions. The showers produces scintillation light in the scintillator and the scintillation light is delivered to photomultipliers tubes (PMTs). The signal converted by PMTs is digitized by the front end electronics. The amount of light is proportional to the incident energy.

The CDF II calorimeter system is divided into two regions: central and plug region. The central calorimeters are located around the tracking volume and the plug calorimeters are located forward and backward of the tracking region. The central calorimeter system is segmented into towers and each tower is 15 $^\circ$ wedges in azimuth by about 0.11 in pseudo-rapidity. In the plug calorimeter covering $1.10 < |\eta| < 2.11$, the wedges are segmented into 7.5 $^\circ$ in azimuth.

The calorimeter is composed of an inner electromagnetic (EM) section and an outer hadronic section. In both sections, scintillator tiles are used as the active elements and

the wavelength shifting (WLS) fibers are embedded in the scintillator for readout. The EM calorimeter is a multi-layer lead/scintillator sampling calorimeter. A unit layer is composed of 4.5 mm lead and 4 mm scintillator. The hadron calorimeter uses 23 layers of iron and scintillator with a unit layer of 2 inch iron and 6 mm scintillator.

The CDF II also employs a shower maximum detector which is an embedded two dimensional readout strip chamber at the expected point of the shower maximum. The shower maximum detector provides the position information to match with tracks and map the transverse shower profile and thus can be used to identify electromagnetic showers and separate photons from neutral pions.

The central calorimeter is composed of the central electromagnetic (CEM), central hadronic (CHA), and end-wall hadronic (WHA) calorimeters and the plug calorimeter comprises the plug electromagnetic (PEM) and plug hadronic (PHA) calorimeters. A cross section of the plug calorimeters is shown in Fig. 2.8.

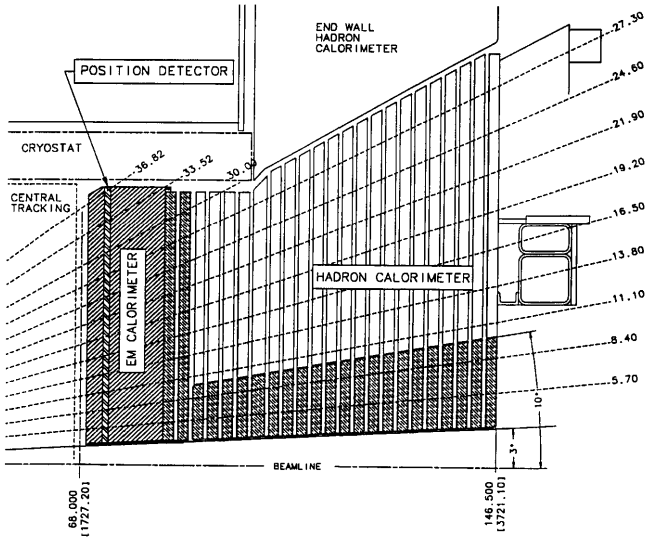

Figure 2.8: Cross section of upper part of end plug calorimeter.

Since both the central and plug regions have the scintillator-based calorimeter, a common design is used for much of the front-end electronics for the both calorimeters and associated shower-maximum detectors. The calorimeter ADC readout uses the multi-ranging QIE (Charge Integrating and Encoding) chip developed for the KTEV experiment. An adc/memory (ADMEM) VME board has small front-end modules on which the QIE and commercial ADC are mounted. The ADMEM board digitizes the

signal from the PMTs and then sums into trigger towers based on 24 divisions each in η and ϕ. The energy is weighted by $\sin\theta$ considering the position of the PMT in the detector to calculate E_T. Each ADMEM boards includes 20 of the front-end modules and provides the Level-1 trigger with transverse energy sums and Level-2 storage. The ADMEM sends the event to the Digital Information Receive And Compare (DIRAC) boards then the Level 1 decision is generated. Upon the receipt of a Level Accept (L1A), the Digital Cluster And Sum (DCAS) boards latch the event in one of four buffers and begin the clustering algorithms. The result of the clustering are sent into the Level 2 decision crate. The final decision from the Trigger Supervisor (TS) will be transmitted to the Front End crates and the data latched into the on board buffers will be recorded or discarded. The data flow of the Level-1 calorimeter trigger is shown in Fig. 2.9

Muon Systems

A muon has a long lifetime (2.2 μs) and low rate of interaction with matter for energy above a few GeV. If a charged particle penetrates a large amount of absorber with only minor energy loss and undergoes only a small angular displacement, it is considered to be a muon. The calorimeter steel, the magnet return yoke, additional steel walls, and the steel from the Run I forward muon toroids are used as the absorbers. The CDF II muon detectors consist of four systems of scintillators and proportional chambers for detection of muons in the region $|\eta| \leq 2.0$. The four systems are all functionally similar but are divided into four logical systems due to the geometric and engineering problems of covering the full η region. The Central Muon (CMU) is the original set of muon chambers since the Run I and the Central Muon Upgrade (CMP) consists of a second set of muon chambers behind an additional 60 cm of steel in the region 55 $^\circ$ $\leq \theta \leq$ 90 $^\circ$ with a layer of scintillation counters (CSP). The Central Muon Extension (CMX) with scintillation counters (CSX) is located at each end of the central detector and extends in polar angle from 42 $^\circ$ to 55 $^\circ$. The Intermediate Muon Detector (IMU) has a barrel of CMP-like chambers and CSP-like scintillation counters. The pseudo-rapidity and other parameters of the CDF II muon detectors are listed in Table 2.3 and the location of the muon detectors in azimuth ϕ and pseudo-rapidity η for Run II is shown in Fig. 2.10.

In the muon chamber, charged particles ionize the gas and the ionization electrons

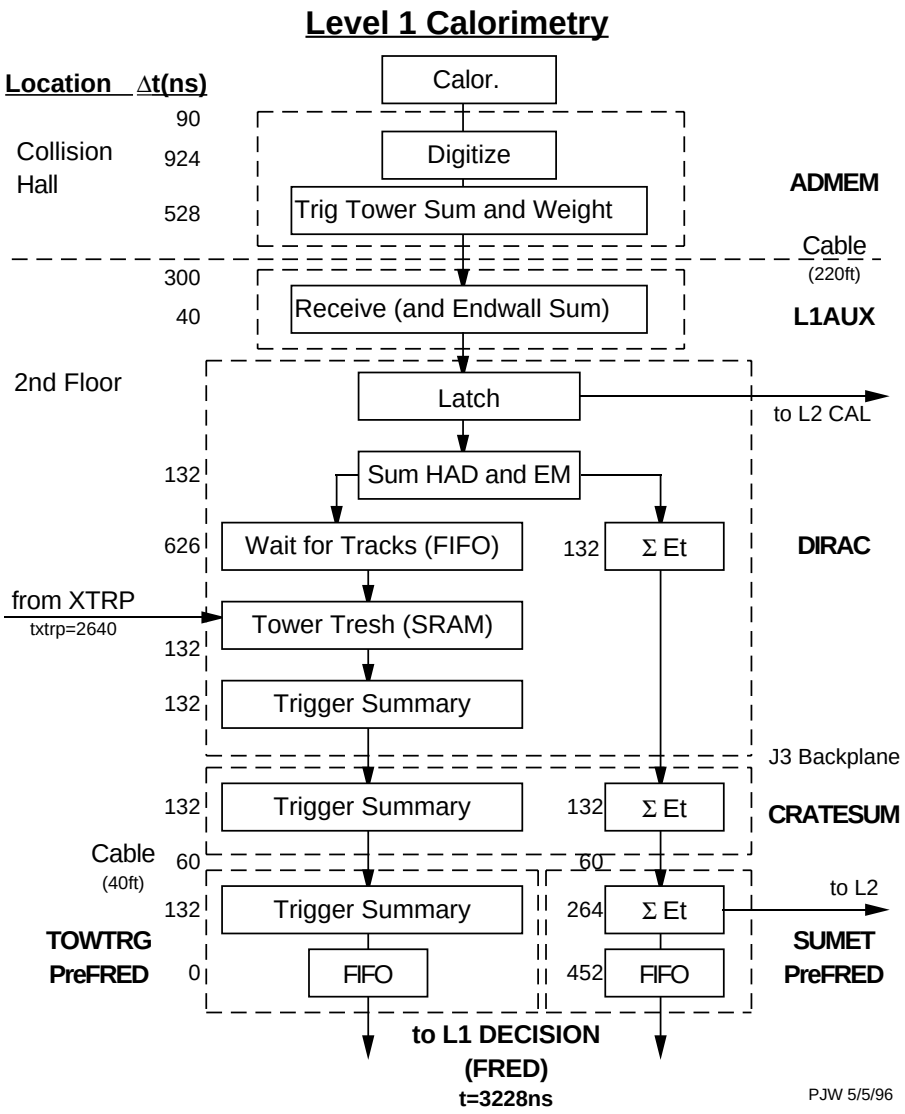

Figure 2.9: A block diagram of the Level-1 calorimeter trigger.

drift toward the sense wire. The gas used in the chambers is the same as that of COT (50:50 mixture of argon and ethane). The scintillation counters are located beyond the muon chambers and used for timing and rejecting backgrounds from out-of-time interactions. The configuration of the Central Muon Upgrade (CMP) wall is shown in Fig. 2.11.

	CMU	CMP/CSP	CMX/CSX	IMU
Pseudo-rapidity coverage	$\lvert\eta\rvert \leq \sim 0.6$	$\lvert\eta\rvert \leq \sim 0.6$	$\sim 0.6 \leq \lvert\eta\rvert \leq \sim 1.0$	$\sim 1.0 \leq \lvert\eta\rvert \leq \sim 1.5$
Drift tube cross-section	2.68×6.35 cm	2.5×15 cm	2.5×15 cm	2.5×8.4 cm
Max drift time	800 ns	1.4 μs	1.4 μs	800 ns
Minimum muon p_T	1.4 GeV/c	2.2 GeV/c	1.4 GeV/c	1.4 - 2.0 GeV/c

Table 2.3: The pseudo-rapidity coverage and other parameters of CDF II muon detectors.

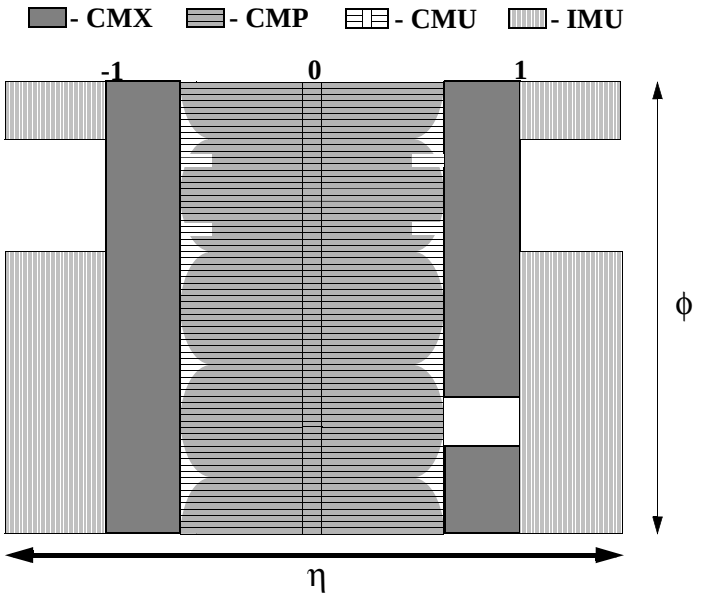

Figure 2.10: Extent of CDF II muon detector coverage in the azimuth ϕ and pseudo-rapidity η.

Luminosity Measurement

The Cherenkov Luminosity Counters (CLC) measure the luminosity at CDF II. The CLC is located around the beamline in the forward region ($3.7 < |\eta| < 4.7$). The CLC consists of long, conical, gaseous Cherenkov counters that point to the collision region and has excellent amplitude and time resolution. By correlating signal arrival time with the Tevatron RF signal, the CLC can distinguish collisions of particles in the bunches from beam losses, which are typically out of synchronization. The amplitude measured by the CLC is proportional to the number of proton-antiproton interactions. The amplitude is converted to a luminosity measurement with an uncertainty dominated by the 6% systematic uncertainty due to the uncertainty on the knowledge of the inelastic $p\overline{p}$

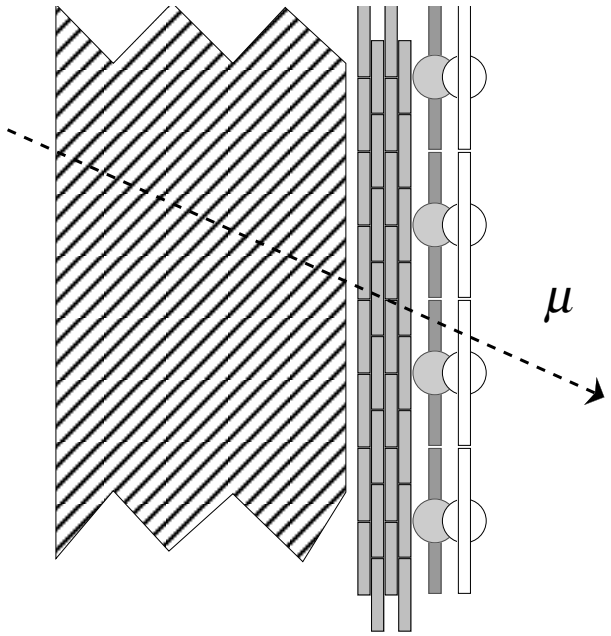

Figure 2.11: The configuration of steel, chambers and counters for the Central Muon Upgrade (CMP) walls. A muon track is drawn to establish the interaction point. Counter readout is located at z=0. Counters layers are offset from the chambers and from each other in x to allow overlapping light guides and PMTs, minimizing the space required.

cross-section[24].

2.2.2 Trigger Systems

In hadron collider experiments the collision rate is much higher than the rate at which data can be stored on tape. The collision rate for Run II is about 1.7 MHz while the maximum tape-recording rate is only about 75 Hz. To cope with such high collision rate, the trigger must efficiently extract the most interesting physics events from the large number of minimum bias events. The CDF II trigger system has a three level architecture. Each level provides a sufficient rate reduction which allows for processing in the next level with minimal deadtime. The block diagram of the CDF II trigger system is shown in Fig. 2.12.

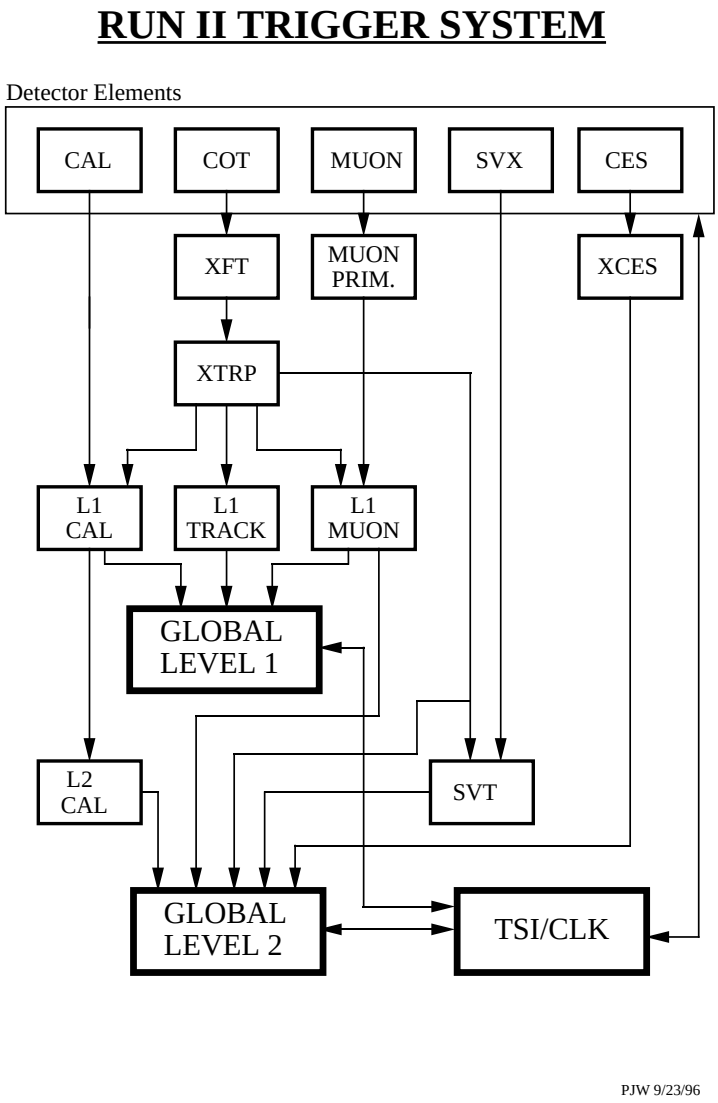

Figure 2.12: Block diagram of the CDF II trigger system. The CLC and TOF triggers are not shown here.

Level-1

The Level-1 (L1) trigger is a synchronous hardware trigger in which the decision is made at a fixed time, $\sim 5\,\mu$s after collisions. All data have to be buffered for at least this delay time for the trigger to operate. The hardware implementation is unavoidable since the L1 accept (L1A) rate is limited to about 25 kHz based on the time needed by the Level-2 triggers. The input to the L1 hardware is from the calorimeters, tracking chamber, and muon detectors. A L1 decision can also be made by matching preliminary tracks available at L1 to clusters in the electromagnetic calorimeters and to stubs

in the muon detectors for electron and muon identification. In the L1 processing, the eXtremely Fast Tracker (XFT) collects the data from the four axial superlayers of the COT. The tracks reconstructed by the XFT are sent to the extrapolation unit (XTRP). Using lookup tables, the XTRP extrapolates the tracks to the calorimeter and muon detector systems. The XTRP sends the tracks or information derived from the tracks to the L1 muon system (L1MUON), the L1 calorimeter trigger (L1CAL), and the L1 track trigger (L1TRACK) as shown in Fig. 2.12. The Global Level-1 hardware collects all the decisions from each subprocess and makes a final L1 decision based on AND/OR combinations of the subprocesses. Data buffered for an accepted event are passed to L2 processing.

Level-2

An asynchronous combination of hardware and software triggers is used in the Level-2 (L2) trigger system. The L2 accept rate is about 600 Hz with average processing time of $\sim 30\ \mu$m. After an event is written into one of the four L2 buffers by L1A, the L2 starts processing of the event for L2 decision. While the event is analyzed by L2 that buffer cannot be used for additional L1A. When all four L2 buffers are filled at the same time the system goes dead. The L2 decision time needs to be less than about 80% of the average time between L1A to keep the deadtime acceptable. The L2 decision uses all the L1 information with higher precision and additionally the data from the SVX II detector and the shower maximum detector. The Silicon Vertex Tracker (SVT) combines the data from SVX II and the tracks from the XTRP. The SVT should be able to reconstruct 2-D tracks quickly as accurate as the full offline analysis. This is crucial for finding b hadrons which have a relatively long lifetime ($\sim 10^{-12}$ s). The b hadrons generated at CDF II typically travel a few millimeters before they decay. The displaced tracks of the daughter particles from the primary vertex and a consequent large impact parameter d_0 can be used to identify the b hadrons. The SVT substantially increased the b physics reach by a precise measurement and selection on the impact parameters of tracks.

The SVT reads out the data from the SVX II and process it through the Hit Finder. The Hit Finder scans the data stream for clusters of hit strips and finds the centroid of each cluster, which is the most probable track intersection point when acceptable clusters are found. While the Hit Finders are running, the list of tracks found during L1 is sent to the Associative Memory Sequencer (AMS) from the XTRP. The AMS converts

the cluster centroid into a coarser Superstrip in preparation for the pattern-recognition by using a lookup table. The data from the AMS is transmitted the Associative Memory (AM) boards which distributes the data stream out to 128 AM chips mounted on the board. Each AM chip stores 128 combinations of outer tracks and coarse SVX hits and each combination represents a valid particle trajectory or "road". When the track candidate match a pattern the road is sent to the Hit Buffer and the Hit Buffer collects necessary data for each road. The Hit Buffers send a track packet which consists of one outer track and four SVX hits to the Track Fitter. The Track Fitter performs a linear approximation fit on each track packet. The architecture of the SVT trigger is shown in Fig. 2.13.

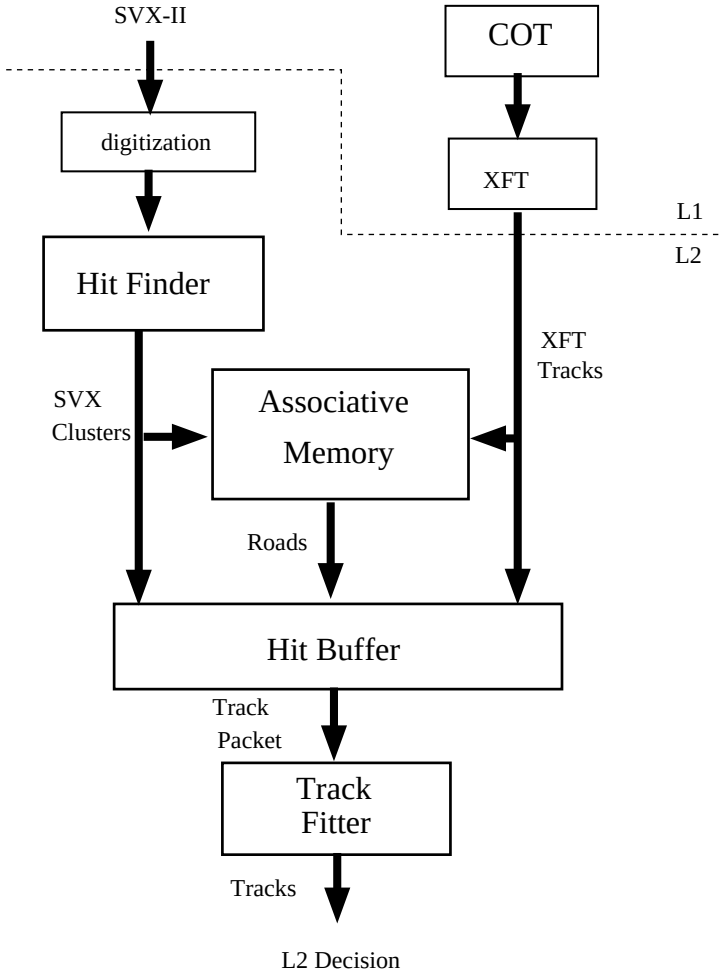

Figure 2.13: The architecture of the SVT trigger.

The data from the EM calorimeter shower maximum detector reduce trigger rates for electrons and photons triggers. The shower maximum readout board has an extra

trigger circuit which produces the trigger output bits (XCES) to be used in the L2 decision. The XCES bit is determined by comparing the sum of the signals from the four adjacent showermax wires to a threshold. The requirement of a cluster above threshold in the shower maximum detector prunes the background from single-PMT discharge and the track matching from the central tracker to the shower maximum reduces the combinatoric background for electron triggers since the spatial resolution of the shower maximum detector is much smaller than a calorimeter wedge.

The L1CAL thresholds have to be set much lower than the jet energy due to the fact that jets are not fully contained by trigger towers in the L1. This could lead to unacceptably high rates for readout into L3. The Level-2 Cluster Finder (L2CAL) provides a reduction in the jet trigger rates at L2 using the transverse energy of trigger towers. The L2CAL combines contiguous regions of calorimeter towers with non-trivial energy to form clusters and thus allows a higher trigger cut to be applied to the total transverse energy of the clusters.

The Global L2 decision making hardware collects all the L2 information from the SVT, track and muon information, XCES, and L2CAL. The analysis of an event in L2 can occur simultaneously as the data for the next event is loaded into memory. A L2 accept (L2A) actuates full detector readout for the event.

Level-3

The Level-3 (L3) uses a "farm" of parallel processors running on the full event readout. The L3 trigger subsystems receives fragments of the event data from the Event Builder which is a small farm of Scanner CPUs and builds complete events into the data structures for analysis. A L3 trigger algorithm then categorizes the events and decides to write the events to mass storage. The L3 algorithms use the full detector information and higher resolution which are not available in the lower trigger levels, *e.g.*, full 3-dimensional track reconstruction and tight matching of tracks to calorimeter and muon system. The L3 system consists of 18 subfarms and each subfarm has 10-15 processing nodes, a converter node, and an output node. The converter node assembles the data fragments from the Event Builder and distributes the complete event to the next available processor node in its subfarm. The processors nodes fully reconstruct the event and check all trigger paths for the L3 trigger decision. The accepted events are collected by the output nodes which send the events to Consumer Server Logger (CSL). The CSL writes the event to the disk and the raw data will be moved to the

Grid Computing Center (GCC) where the data is archived onto tape. A fraction of the data is passed to the online monitoring processes by the CSL.

Dynamic Prescale

The limited trigger bandwidth is shared by broad physics program. A "path" is defined by a unique AND combination of L1, L2, and L3 triggers. The trigger bandwidth is planned by dataset which consists of one or several paths. This approach has advantages of an easy identification of the provenance of a dataset and a convenient monitoring of the cross section of individual triggers within a path in the presence of variations of luminosity and detector noise.

As an additional effort to minimize deadtime while accommodating high rate triggers, a Prescale (PS) is introduced. The PS accepts a predetermined fraction of events for high rate triggers to fit the triggers into the limited trigger bandwidth. Since the trigger cross sections grow with luminosity, using a fixed value of the fraction for all luminosities will be too restrictive as luminosity falls during a run. The Dynamic Prescale (DPS) has been implemented in the trigger paths since 2002 and applied to triggers with high growth rate. The DPS reduces the PS fraction dynamically in a time scale of minutes (μs in special case) as luminosity falls. The three values, Maximum PS (initial value at start of a run), Default PS, and Minimum PS, are used to adjust PS fraction as the trigger rate changes in the course of a run. There are several different DPS schemes (Fractional Prescale, Rate Limit, Über Prescale, Luminosity Enable, etc.) used in the trigger paths utilizing various aspects of the trigger system.

Chapter 3

$\psi(2S)$ Polarization Measurement

"Do not fear to be eccentric in opinion,
for every opinion now accepted was once eccentric."
— Bertrand Russell 1872–1970

The polarization of the $\psi(2S)$ meson is measured from the angular distribution of its decay into muon pairs ($\psi(2S) \to \mu^+\mu^-$). The decay angle θ^* is defined as the angle between the μ^+ direction in the $\psi(2S)$ rest frame and the $\psi(2S)$ direction in the lab frame as shown in Fig. 3.1. The polarization determines the distribution of the decay angle:

$$\frac{d\Gamma}{d\cos\theta^*} \propto \frac{3}{2\,(\alpha+3)}\left(1+\alpha\cos^2\theta^*\right) \tag{3.1}$$

Parity conservation requires that the distribution is symmetric about $\cos\theta^* = 0$. The longitudinally and transversely polarized $\psi(2S)$ can be defined to be ones whose spin components along the polarization axis are 0 and ± 1 respectively. Strictly speaking, since the polarization parameter α discriminates either helicity states ± 1 or 0, the spin alignment of $\psi(2S)$ is measured in this thesis, not the individual helicity states $+1$, 0, -1. For fully transversely polarized production the polarization parameter α is equal to $+1$ and α is equal to -1 for fully longitudinal polarization.

In order to determine the polarization parameter, the measured $\cos\theta^*$ distribution is compared to the distribution of realistic Monte Carlo simulations taking account of geometric and kinematic acceptance of the detector as well as the reconstruction

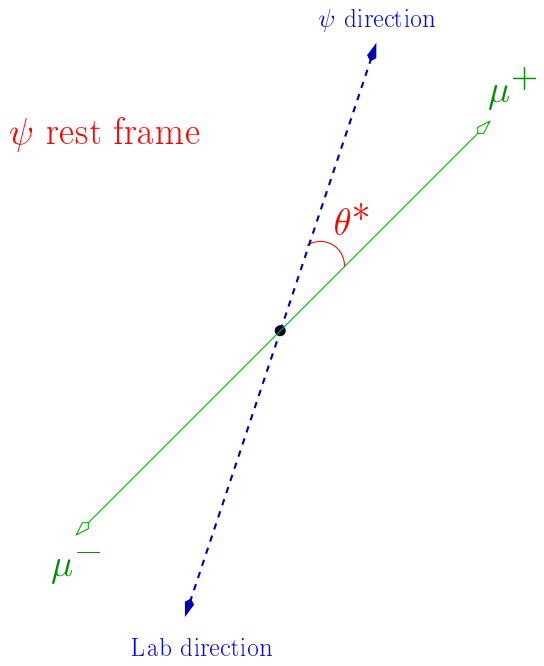

Figure 3.1: The definition of the decay angle θ^*.

efficiency. Based on the impact parameter information, polarization of the prompt and B-decay $\psi(2S)$ are separately measured.

The observed $\cos\theta^*$ distribution can not be directly compared to the vector meson decay angle distribution given by Eq. 3.1 due to detector acceptance and efficiency effects. Therefore MC samples were generated with a fully transverse or longitudinal polarization state. The experimental efficiency function was applied to each MC sample. The simulated samples go through the detector simulation and corrections for the acceptance.

3.1 Datasets and Event Selection

The data collected from February 2002 to February 2006 have been used in the polarization analysis. The dataset sample is the J/ψ dimuon trigger datasets `jpmm0d`, `jpmm0h` and `jpmm0i`, and the `GOODRUN LIST v.13` from the Data Quality Monitor group is used for the good run selection. Since this analysis uses data collected by the track based dimuon trigger, the performance of the COT is very important. Early in the `jpmm0d` dataset, the COT suffered a gain drop due to wire aging and the performance

was not stable until oxygen was added to the gas. The $\psi(2S)$ polarization with different muon p_T cuts including this period has been looked at and a muon p_T dependency was discovered even though the efficiency for a single muon varied only moderately with single muon p_T. Large non-statistical fluctuations in polarization during this period is also reported in the J/ψ polarization analysis [25]. Therefore only the data after the full recovery of the COT are used in this analysis. This comprises runs from 184228 to 212133 and the total luminosity included is approximately 800 pb^{-1}.

The $\psi(2S) \rightarrow \mu^+\mu^-$ decays are reconstructed by selecting events with two oppositely charged muon candidates reconstructed in the COT and CMU(P). A muon candidate is triggered by a match between a track found in the COT and a collection of hits (stub) in the muon detectors. The SVX II information is added to the candidate tracks later on. Only the muons in the CMU(P) fiducial region $|\eta| < 0.6$ are used in the analysis. Events are required to have satisfied the trigger path `L1_TWO_CMU1.5_PT1.5` and following L3 path `JPSI_CMUCMU1.5`. The trigger requirements are verified for the off-line reconstructed candidates. The Level 1 trigger requirements are verified by using the `MuonTrigMatch` module in the `cdfsoft` package. The muon stub was validated by tower ID and track matching between XFT and reconstructed tracks; agreement was defined to be $\Delta\phi < 0.5^\circ$ and $\Delta(1/p_T) < 0.1(\text{GeV}/c)^{-1}$. Tracks passing within 1.5cm of the center of the COT wire planes in any of the four axial superlayers have been excluded to avoid the region of low XFT tracking efficiency. The CMU wedge 17W is known for its lower efficiency due to a hardware problem. The muons from this wedge are excluded. The acceptance is corrected for these cuts. In addition, each CMU stub matched to a triggered stub must lie within the XTRP search window set by the Level 1 triggered track. Furthermore, track momentum is corrected for energy loss due to specific ionization and multiple scattering accounting for the detector materials. The $\psi(2S)$ candidate invariant mass has been calculated from the four-momenta of the two muons.

The offline selection cuts are applied matching those in the dimuon trigger efficiency study for the $B_s \rightarrow \mu^+\mu^-$ analysis [26]. A muon p_T cut, $p_T > 1.75$ GeV/c, has been applied to avoid the XFT turn-on at 1.5 GeV/c and the 1.6 GeV/c threshold of the dimuon trigger efficiency function. The offline selection cuts are listed in Table 3.1.

The invariant mass of the $\psi(2S)$ candidates is required to be within $3.4 \leq m_{\mu^+\mu^-} < 3.9$ and the $p_T(\psi(2S))$ is required to be equal or greater than 5 GeV/c. The $p_T(\psi(2S))$ is binned into 3 regions: 5 - 7, 7 - 10 and 10 - 30 GeV/c. Then a mass fit is performed

Basic offline requirements	CMU-only or CMUP muons
	$\chi^2(\Delta(r\phi)_{CMU}) < 9$
	$\Delta\phi < 2.25$
	$\lvert\Delta z_0\rvert < 5$ cm
	$\lvert z_0(\mu)\rvert < 60$ cm
	$\lvert y(\mu^+\mu^-)\rvert < 0.6$
	$3400 \leq m_{\mu^+\mu^-} \leq 3900$ MeV/c^2
Basic SVXII cut	at least 3 $r-\phi$ silicon hits
SVXII vertex quality cut	$\sigma_{L_{xy}} \leq 0.025$
	Fit probability ≥ 0.001
COT hit selection	Axial/Stereo hits ≥ 10

Table 3.1: Offline selection cuts

in each bin using a single Gaussian signal with a linear background. The signal and sideband regions in the dimuon mass are defined for each $p_T(\psi(2S))$ bin, as shown in Table 3.2. These are used in the polarization fit. The signal region covers ± 3 standard

$p_T(\psi(2S))$ [GeV/c]	peak/width [MeV/c]	Signal region [MeV/c]	Lower sideband [MeV/c]	Upper sideband [MeV/c]
$\geq$ 5	3685.3/16.9	3634.4 - 3736.1	3515.9 - 3566.7	3803.8 - 3854.6
5 - 7	3685.5/16.5	3635.9 - 3735.0	3520.2 - 3569.8	3801.1 - 3850.7
7 - 10	3685.1/16.9	3634.5 - 3735.8	3516.2 - 3566.9	3803.4 - 3854.1
10 - 30	3684.3/19.3	3626.3 - 3742.3	3491.0 - 3549.0	3819.7 - 3877.7

Table 3.2: The signal and sideband regions of $\psi(2S)$ mass fit.

deviation(width of the Gaussian fit) around the signal peak(centroid of the Gaussian fit). A symmetric sideband region is chosen to avoid the radiative tails. The lower sideband is from $m_{\psi(2S)} - 10\sigma$ to $m_{\psi(2S)} - 7\sigma$ and the upper sideband from $m_{\psi(2S)} + 7\sigma$ to $m_{\psi(2S)} + 10\sigma$. The mass fit results and the illustration of the signal and sideband regions are shown in Figure. 4.3. In the lowest p_T bin, which has the largest number of events, the radiative tail under the peak is not well described by the single Gaussian fit. The event loss of the radiative tail due to a single Gaussian fit is examined in a Monte Carlo sample for the highest statistics p_T bin. The largest loss is 1.43 %. A

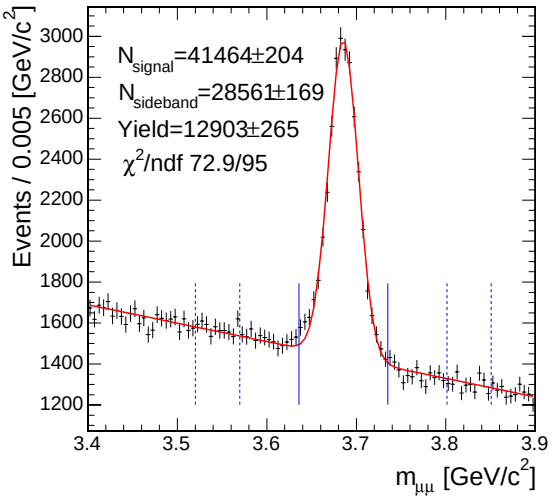

(a) $p_T(\psi(2S))$ 5 - 7

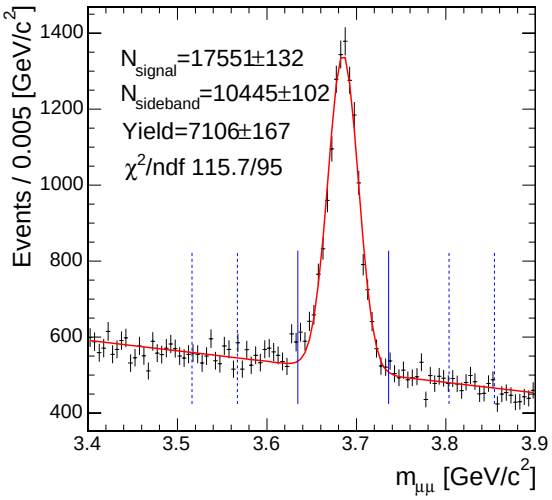

(b) $p_T(\psi(2S))$ 7 - 10

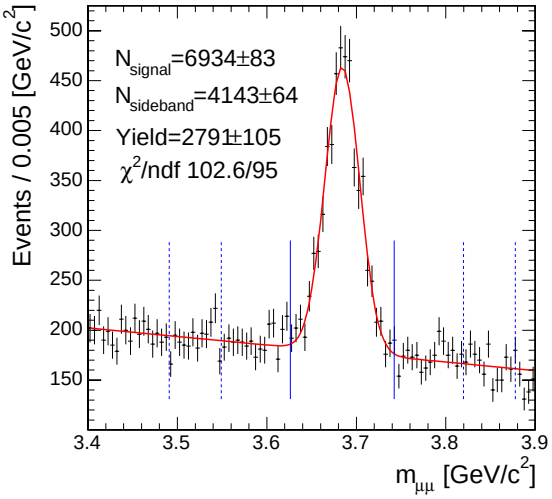

(c) $p_T(\psi(2S))$ 10 - 30

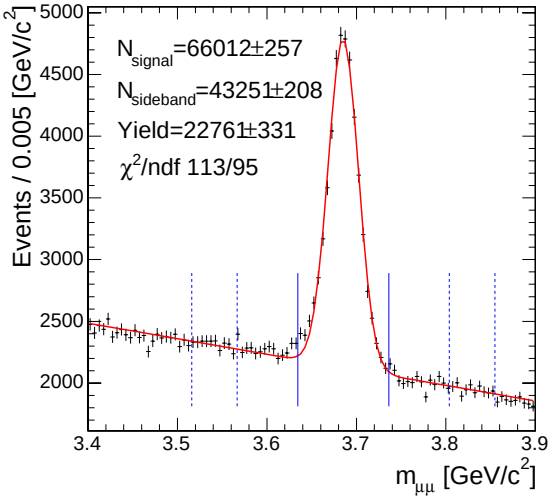

(d) $p_T(\psi(2S))$ 5 - 30

Figure 3.2: The $\psi(2S)$ mass fit result and the signal and sideband regions.

systematic uncertainty is assigned for this small loss.

3.1.1 Prompt and B-decay $\psi(2S)$

Based on the fact that the prompt events have ct consistent with zero and B-decays have an exponential ct distribution, the prompt and B-decay $\psi(2S)$ mesons have been separated by applying a cut on the sum of squares of the impact parameter significance

of the two tracks, S:

$$S = \left(\frac{d_0(\mu^-)}{\sigma_{d_0(\mu^-)}}\right)^2 + \left(\frac{d_0(\mu^+)}{\sigma_{d_0(\mu^+)}}\right)^2 . \tag{3.2}$$

By requiring $S \leq 8$, events arising from B-decay are significantly reduced and thus a prompt $\psi(2S)$ sample is made as shown in Figure 3.3. The flat background has been strongly attenuated. The cut value decision is based on the S distribution of the data sample (Figure 3.4a). The cut is optimized for keeping the prompt fraction higher

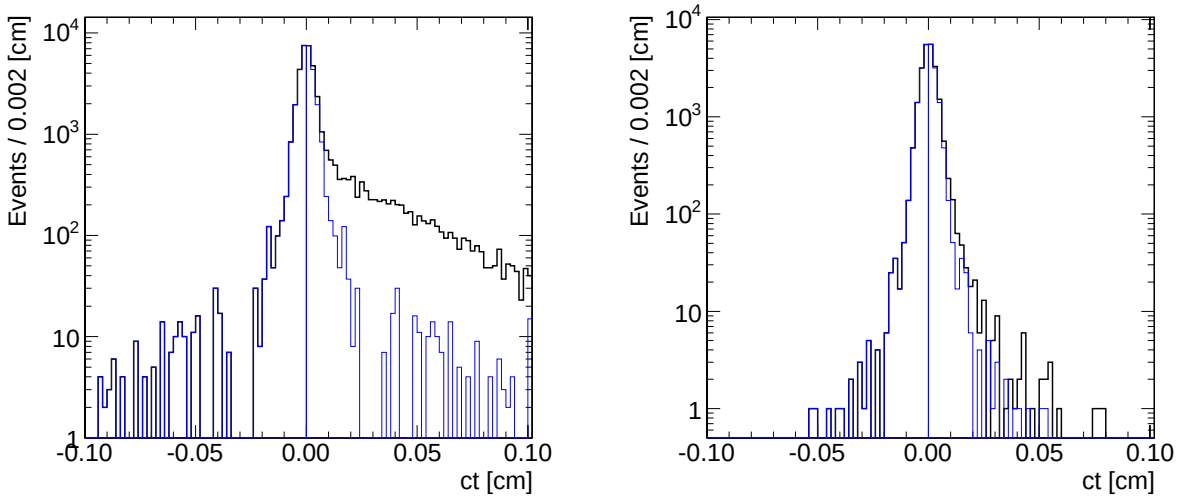

(a) No impact parameter significance cut

(b) $S \leq 8$

Figure 3.3: The ct distributions: The negative ct is reflected around $ct = 0$ to get prompt distribution. The prompt decay has a Gaussian distribution centered at 0 affected by the detector resolution. In Figure 3.3b, we see that the flat background has been clearly eliminated.

while reducing the B-decay effectively. Since B-decay events are not expected to have negative ct [1] and prompt events is expected to have a Gaussian distribution centered around $ct = 0$ due to the detector resolution, the events in the $ct < 0$, N_N, have been reflected around $ct = 0$ to get prompt distribution. The B-decay events N_B in each ct bin are the difference between the total events in the bin for $ct > 0$ and the number of events in the corresponding negative ct bin. The fraction of the B-decay background, F_B which also includes a flat tail of mis-measured events, is $N_B/(N_N + N_P)$. The

[1] A simulation shows that the fraction of mis-measured B-decay events with negative ct is negligible($< 0.2\ \%$) [25].

number of N_N and N_B events are listed in Table 3.3. The fraction of B-decays in the

$p_T(\psi(2S))$[GeV/c]	$N_{S\leq 8}$	N_N	N_B	F_B[%]
$\geq$ 5	22760	10980	800	3.5 ± 0.7
5 - 7	12903	6349	205	1.6 ± 0.9
7 - 10	7105	3378	349	4.9 ± 1.2
10 - 30	2790	1275	240	8.6 ± 1.8

Table 3.3: The prompt and B-decay $\psi(2S)$ events in each p_T bin.

prompt sample after the impact parameter significance cut is 3.5 ± 0.7 % overall. This will be corrected in each bin by an independent measurement of the $\psi(2S)$ polarization from B-decay.

The B-decay sample has been constructed by requiring the impact parameter significance cut, $S \geq 16$ which removes most of the prompt $\psi(2S)$ events centered around $ct = 0$. The impact parameter significance cut for B-decay was decided by looking at the S distribution of an unpolarized prompt $\psi(2S)$ Monte Carlo sample (Figure 3.4b). After applying the impact parameter significance cut with $S > 16$, B-decay events are mostly in the positive ct region, as shown in Fig. 3.5. The negative ct distribution is again reflected around 0 to get prompt and random contribution. The flat tail in Fig. 3.5 comes from mis-measured events. Most of the prompt events that peak at small ct are removed. The N_N, N_P, and N_B events are assigned in the same way as the prompt sample, and the fraction of the prompt and random distribution, F_{bgnd} is defined as $2N_N/(N_N + N_P)$. The number of events are summarized in Table 3.4. There

$p_T(\psi(2S))$[GeV/c]	$N_{S\geq 16}$	N_N	N_B	F_{bgnd}[%]
$\geq$ 5	5806	341	5124	11.7 ± 0.4
5 - 7	2644	90	2464	6.8 ± 0.5
7 - 10	1906	144	1618	15.1 ± 0.9
10 - 30	1176	57	1062	9.7 ± 0.9

Table 3.4: The B-decay and background events.

is overall 11.7 ± 0.4 % residual random background. This background is dominated by the mis-measured events and assumed to have zero polarization in all p_T bins.

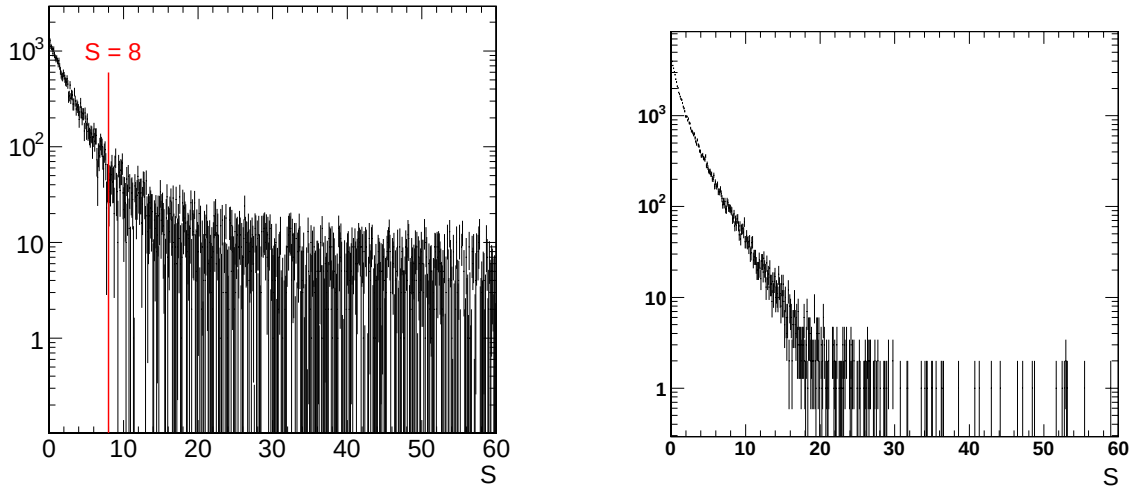

(a) S distribution of the data sample

(b) S distribution of a MC sample

Figure 3.4: The impact parameter cut determination for the prompt and B-decay samples. In (a) one sees that the data distribution is peaked at small S with a long tail primarily from B-decay events for $S > 8$. In (b) a Monte Carlo sample of prompt $\psi(2S)$ decays shows that few Monte Carlo events survive past $S > 16$.

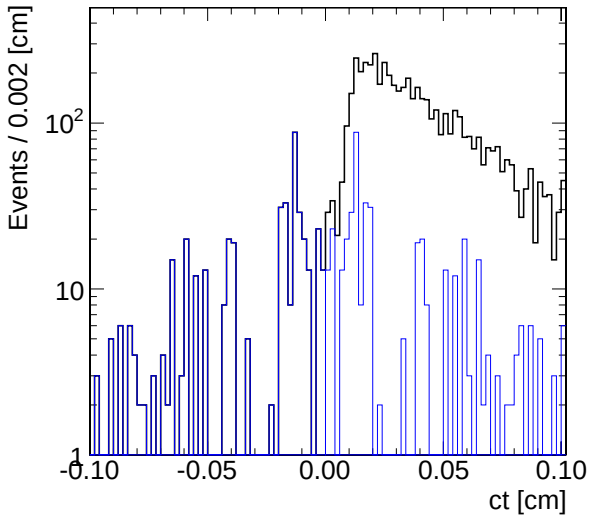

Figure 3.5: The ct distribution of B-decay sample. The positive ct events are from B-decay and the negative ct is reflected to get prompt and random events. The prompt events were removed and the flat background is dominant.

3.2 Monte Carlo Simulation

Monte Carlo(MC) samples are one of the most important ingredient of the template method polarization fit. The main idea of the template method is to compare the

observed $\cos\theta^*$ distribution with fully polarized (transverse/longitudinal) $\cos\theta^*$ distribution from MC samples.

In order to measure the prompt and B-decay $\psi(2S)$ polarization, a set of Monte Carlo templates has been generated for prompt and B-decays using `B-Physics Monte Carlo` with `release 5.3.4`. The templates are generated by processing simulated samples of $\psi(2S) \to \mu^+\mu^-(B \to \psi(2S) + X,\ \psi(2S) \to \mu^+\mu^-)$ decays with a detector simulation and an emulation of the data-based trigger efficiency [26]. A pair of transverse/longitudinal templates is generated for each sample. The plots of each $\cos\theta^*$ templates used in this analysis can be found in Appendix B.

3.2.1 Prompt MC generation

For prompt $\psi(2S)$ Monte Carlo simulation, 12 million events have been generated for each transverse/longitudinal template. A single particle gun, `FAKE_EVENT`, generated $\psi(2S)$ with flat ϕ over 2π radian, the rapidity $|y| < 0.8$, and an effective p_T distribution; An unpolarized Monte Carlo sample with flat $\psi(2S)$ p_T distribution is generated and followed by detector simulation and muon trigger efficiency correction. Then the effective p_T spectrum is extracted by comparing the output p_T distribution to the data p_T distribution. Then `EvtGen` [28] decayed the particle in a fully transverse/longitudinal polarization state to a muon pair. `EvtGen` is an event generator which is designed for the simulation of B decays. `EvtGen` is developed to provide a framework to handle complex sequential decays and $\mathcal{CP}$ violating decays. The most related part of tcl script to run the simulation is shown in Appendix B.2.1.

3.2.2 B-decay MC generation

For B-decay $\psi(2S)$ Monte Carlo simulation, 3 million events have been generated for each transverse and longitudinal template using `Bgenerator` with the measured B hadron p_T spectrum from the Run II measurement [29]. `Bgenerator` produced $B \to \psi(2S) + X$ events for $|y| < 1.3$ and flat ϕ over 2π radian. And then `EvtGen` is used as a decay package. All the B meson decay modes including $\psi(2S)$ have been selected from the `EvtGen` decay file `DECAY.DEC` in `cdfsoft v5.3.4` and then the sum of the decay mode fraction is normalized. The most related part of tcl script to run the simulation is shown in Appendix B.2.2 and the modified decay table is shown in Appendix B.3.

3.2.3 Acceptance and Trigger Efficiency

The dimuon trigger strongly shapes the acceptance as a function of $\cos\theta^*$. In $\psi(2S)$ decays with large values of $\cos\theta^*$, one of the muons is boosted mostly backward from the $\psi(2S)$ direction, and so is likely to have low p_T and hence fail the trigger. The acceptance and trigger efficiency have been accounted by CDF detector simulation (`cdfsim release 5.3.4`) and the data-based trigger efficiency [26]. The rare B-decay group measured Level-1,2 and 3 low-p_T dimuon trigger efficiencies for their $B_s^0 \to \mu^+\mu^-$ analysis. Each level trigger efficiency is measured for different muon p_T,η,ϕ and type (CMU,CMX) in each trigger path and run number. Using these measured values, they developed a trigger efficiency function [30] as a C++ class, `MuonLoPtEfficiency`. The methods of `MuonLoPtEfficiency` class can be used to calculate the trigger efficiency of each level or the total trigger efficiency for a given trigger paths. The `getTotalEfficiency` method for `L3_JPSI_CMUCMU` trigger path with other inputs from realistic MC simulation has been used for this analysis by randomly accepting/rejecting MC events according to the returned trigger efficiency. The trigger efficiency function has no silicon requirement on muon tracks. Since at least 3 silicon $r-\phi$ hits on each muon track are required, a possible bias from the SVX II efficiencies is considered by comparing $\cos\theta^*$ distributions. The ratio of the $\cos\theta^*$ distributions with silicon hits requirement and without the requirement has been calculated and used as a silicon efficiency function. Then a MC events in each $\cos\theta^*$ bin has been randomly accepted/rejected according to the silicon efficiency function. The effective p_T spectrum is calculated from the p_T distribution of the raw data by using an acceptance function $\epsilon(p_T)$ calculated for each p_T bin. The acceptance function is computed using a large sample of Monte Carlo events generated with unpolarized $\psi(2S)$ decays distributed uniformly in p_T. Trigger efficiency and reconstruction losses are included in the calculation as described above.

3.3 Polarization Fit

The polarization parameter is determined by using a chi-square (χ^2) fit to the $\cos\theta^*$ distribution in the data. In the template method polarization fit, two equally-weighted $\cos\theta^*$ distributions, one from fully transverse MC sample and one from fully longitudinal MC sample, are used to fit the observed cosθ^* distribution. The longitudinal fraction η is adjusted as a fit parameter and thus the polarization of $\psi(2S)$ is extracted

from the observed cosθ^* distribution.

A longitudinal polarization fraction η,

$$\eta = \frac{1-\alpha}{\alpha+3}\,, \tag{3.3}$$

which is equivalent to the spin density matrix element ρ_{00} [2] has been used as a χ^2 fit parameter.

The data events are histogrammed in $\cos\theta^*$, with bin widths of 0.1. The data is then fitted to a weighted sum of two (transverse/longitudinal) Monte Carlo templates. The same number of events were generated for transverse and longitudinal Monte Carlo samples so that the fitted weighting between the transverse and longitudinal templates yields the longitudinal fraction η. Then α is derived from the fit parameter, Eq.(3.3).

The fit uses two data $\cos\theta^*$ histograms: one from the mass signal window and one from the mass sideband windows. The sideband windows are used to estimate the $\cos\theta^*$ distribution of background events under the $\psi(2S)$ peak. And two Monte Carlo templates, transverse and longitudinal, are used. The number of events in $\cos\theta^*$ i th bin of the data signal region is denoted by D_i, and S_i for the data sideband region, T_i for the transverse template and L_i for the longitudinal template.

A χ^2 function is defined which takes into account the Poisson distribution of both signal and background events[31]:

$$\chi^2 = 2\cdot\sum_i (E_i+\beta_i-D_i) - D_i\cdot\ln\left(\frac{E_i+\beta_i}{D_i}\right) + (\beta_i - S_i) - S_i\ln\frac{\beta_i}{S_i}\,, \tag{3.4}$$

where E_i is the expected number of signal events in bin i, and β_i is the expected number of background events. Bins with no signal data events are not included in the fit. The β_i do not introduce any extra degrees of freedom into the fit, but are derived explicitly by requiring that

$$0 = \frac{\partial\chi^2}{\partial\beta_i} = 2\left(1 - \frac{D_i}{E_i+\beta_i} + 1 - \frac{S_i}{\beta_i}\right). \tag{3.5}$$

Eq.(3.5) is quadratic in β_i, but only one of the solutions is physical. The expected

[2]The spin density matrix is discussed in Appendix A.

number of signal events is derived from the templates and depends on the polarization:

$$E_i = F_{norm}\left(\eta \cdot L_i + (1-\eta)\cdot T_i\right), \tag{3.6}$$

where η is the longitudinal polarization fraction. The factor F_{norm} is used to normalize the templates to the data. The total number of expected signal events to the total sideband-subtracted number of data events:

$$F_{norm} = \frac{\sum_i (D_i - S_i)}{\sum_i \left(\eta \cdot L_i + (1-\eta)\cdot T_i\right)} \tag{3.7}$$

The software package `MINUIT` is used to minimize the χ^2 function. The fit parameter is η from which α can be derived and the fit returns η and its one standard deviation statistical uncertainties.

An intensive fitter study is done in J/ψ polarization analysis. The fitter has been tested with independently generated MC samples and also the fit error has been studied with 1000 pseudo-experiments by varying each data point of the measured $\cos\theta^*$ distribution with a Gaussian distribution centered at the data point and whose sigma is the error of the $\cos\theta^*$ bin. More details of the fitter test can be found in Section 4 of reference [25].

3.3.1 B-decay Polarization

Since there is no reliable measurement of $\psi(2S)$ polarization from B-decays, the B-decay polarization is measured with the same template method polarization fit. A clean B-decay sample is made by requiring the impact parameter significance cut, $S \geq 16$ as described in Section 3.1. The polarization fit is done for the whole p_T range, 5 GeV/$c \leq p_T(\psi(2S)) < 30$ GeV/c considering the limited statistics. The B-decay polarization is not expected to vary with p_T for the high p_T range considered here: For the B-decay polarization measurement, the decay angle θ^* is defined by using the lab frame in the same way as the prompt polarization measurement. On the other hand, a proper measurement of the polarization of $\psi(2S)$ from B-decay would require the use of a decay angle defined in the B-hadron rest frame. As the B-hadrons were not at rest in the lab frame, the Lorentz boost of the B-hadrons in the lab frame dilutes the polarization measured by θ^*. The $cos\theta^*$ distribution of the fit is shown in Figure 3.6. The returned fit parameter $\eta_{B,fit}$ in Eq. 3.8 still includes the polarization

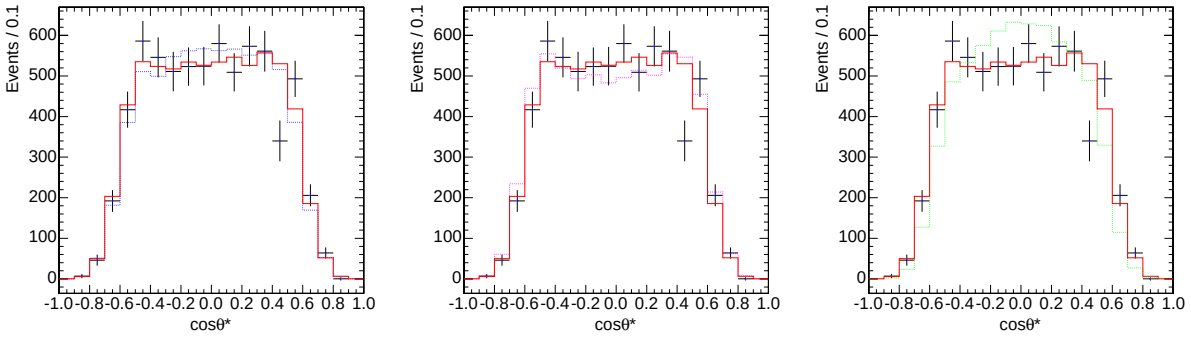

Figure 3.6: The fitted $cos\theta^*$ distribution of $\psi(2S)$ from B-decays with scaled MC templates: In the left, dashed blue line is unpolarized template. In the middle, dashed magenta line is transverse template. In the right, dashed green line is longitudinal template. The solid red line is the best fit line in that p_T bin.

from the remaining background (11.7 ± 0.4 %).

$$\eta_{B,fit} = 0.21 \pm 0.08 \text{ or } \alpha_{B,fit} = 0.30 \pm 0.22, \ \chi^2/\text{d.o.f.} = 24.9/16. \tag{3.8}$$

Since Fig. 3.5 shows only random events for the background, the polarization of the background is set to zero, *i.e.*, setting $\eta_{bgnd} = 1/3$ in Eq. 3.9.

$$\eta_B = \frac{\eta_{B,fit} - F_{bgnd} \cdot \eta_{bgnd}}{1 - F_{bgnd}}. \tag{3.9}$$

After the background correction, the polarization parameter is measured to be:

$$\eta_B = 0.19 \pm 0.09 \text{ or } \alpha_B = 0.36 \pm 0.25. \tag{3.10}$$

To compare with the Run I result listed in Table 3.5, the Run II result is looked at in 3 p_T bins as shown in Table 3.6. Both results are plotted in Figure 3.7. The results agree well except the second p_T bin where the Run I polarization central value was unphysical.

p_T bin [GeV/c]	Mean p_T [GeV/c]	α_B
5.5 - 7.0	6.2	$-0.26 \pm 1.26 \pm 0.04$
7.0 - 9.0	7.9	$-1.68 \pm 0.55 \pm 0.12$
9.0 - 20.0	11.6	$0.27 \pm 0.81 \pm 0.06$

Table 3.5: Run I result for B-decay $\psi(2S)$ polarization.

p_T bin [GeV/c]	Mean p_T [GeV/c]	α_B	χ^2/d.o.f
5.0 - 7.0	5.9	-0.19 ± 0.45	27.8/12
7.0 - 10.0	8.3	0.71 ± 0.39	9.2/14
10.0 - 30.0	13.5	0.08 ± 0.31	15.9/16

Table 3.6: Run II result for B-decay $\psi(2S)$ polarization.

3.4 Systematic Uncertainties

The prompt $\psi(2S)$ polarizations for different muon p_T cuts have been measured while the p_T threshold of $\psi(2S)$ has been kept at 5 GeV/c. The results are shown in Ta-

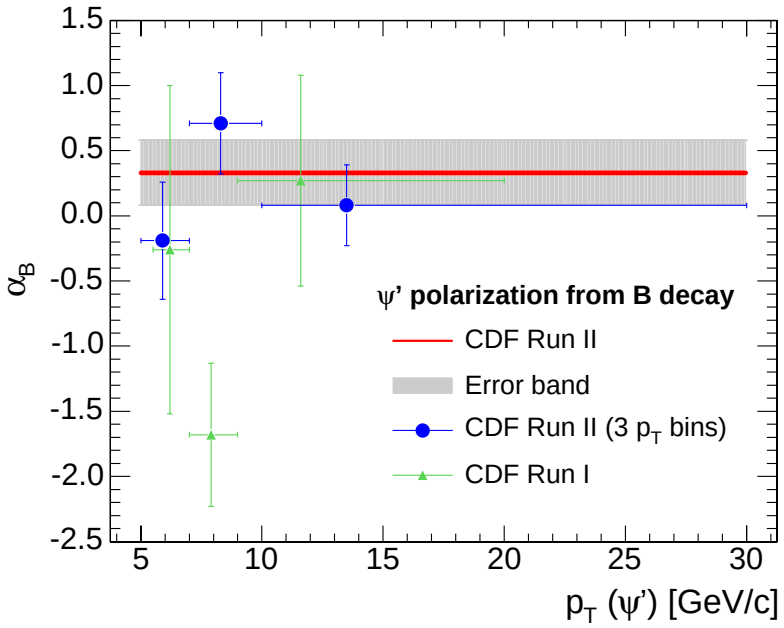

Figure 3.7: The Run II B-decay $\psi(2S)$ polarization compared to Run I result.

$p_T(\psi(2S))$[GeV/c]	η_{fit}	F_B [%]	η_{prompt}	χ^2/d.o.f
5 - 7	0.155 ± 0.101	3.3 ± 0.9	0.153 ± 0.104	9.5/10
7 - 10	0.249 ± 0.097	4.8 ± 1.2	0.250 ± 0.102	21.0/12
10 - 30	0.553 ± 0.147	8.7 ± 1.9	0.585 ± 0.161	21.6/16

Table 3.7: Prompt $\psi(2S)$, $p_T(\mu) > 2.0$ GeV/c.

$p_T(\psi(2S))$[GeV/c]	η_{fit}	F_B [%]	η_{prompt}	χ^2/d.o.f
5 - 7	0.114 ± 0.157	2.3 ± 1.0	0.112 ± 0.161	16.8/10
7 - 10	0.244 ± 0.119	5.0 ± 1.3	0.245 ± 0.125	19.8/12
10 - 30	0.663 ± 0.208	9.4 ± 1.9	0.709 ± 0.230	17.6/16

Table 3.8: Prompt $\psi(2S)$, $p_T(\mu) > 2.25$ GeV/c.

ble 3.7, 3.8 and Figure 3.8. The uncertainties on the fit values for different p_T cuts are highly correlated because all of the events in the higher p_T cut samples are included in the lower p_T cut samples. The polarization of the events for $p_T(\mu) > 2.25$ GeV/c should not be changed when the p_T cut is lowered to 2.0 GeV/c. Then the significance of $\delta\eta = \eta p_{T>2.0} - \eta p_{T>2.25}$ is checked by taking account of the correlated uncertainties. The $\delta\eta$ in each p_T bin is, 0.041, 0.005, and 0.124. This is at most 0.55σ change in the largest p_T bin. There is no indication of systematic uncertainty.

According to the rare B group study, the systematic error on the acceptance function is 0.012. The maximum change in the fit parameter η is 0.003 if the trigger efficiencies are changed by 1σ.

The experimental sensitivity to polarization for a given p_T threshold is shown in Figure 3.9 and 3.10.

The $\psi(2S)$ polarization is sensitive to the p_T distribution of muons. The data muon p_T spectrum is compared with polarization tuned MC samples in each p_T bin. The MC sample has been tuned to match the polarization in each p_T bin by combining transverse polarization MC events and longitudinal polarization MC events with ratio

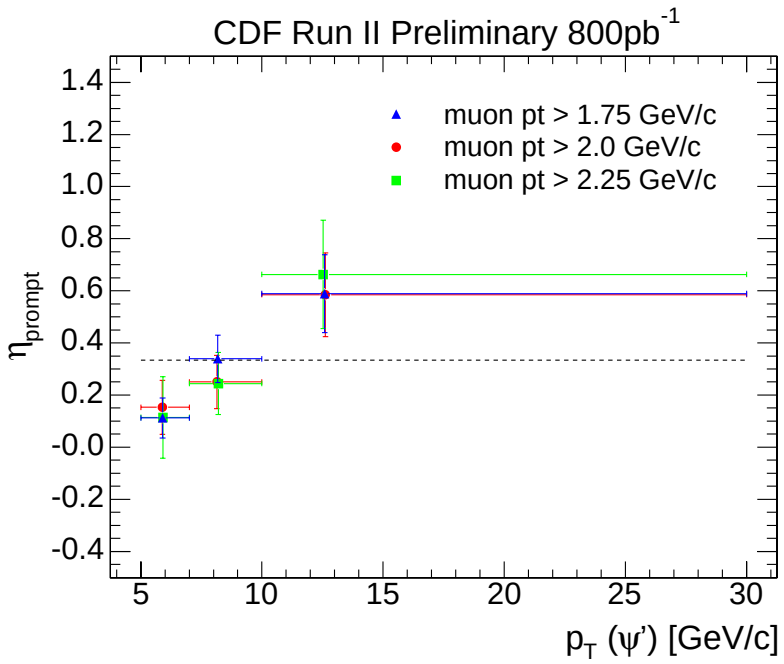

Figure 3.8: The prompt $\psi(2S)$ polarization with different muon p_T cuts.

calculated from

$$\alpha = \frac{\frac{1}{2}\sigma_T - \sigma_L}{\frac{1}{2}\sigma_T + \sigma_L} \,. \tag{3.11}$$

With a given α in each p_T bin, the transverse/longitudinal MC events are mixed with the ratio σ_T/σ_L. The result is plotted in Figure 3.11. The muon p_T distributions of the tuned MC samples in each p_T bin match the muon p_T distributions of data well. The invariant dimuon mass is modeled by a single Gaussian signal and a linear background. This single Gaussian fit misses the radiative tails especially in the highest statistics p_T bin. The yield loss of the radiative tails has been examined in a MC sample as discussed in Section 3.1. The largest loss is 1.43 % and a systematic uncertainty of 0.01 is assigned for the fit parameter η to cover a possible effect.

The 800 pb^{-1} data have been divided into subsets (Before and after Run 199025). The results from the two subsets are consistent within statistics as listed in Table 3.9 and Table 3.10. The plot is available in Fig. 3.12.

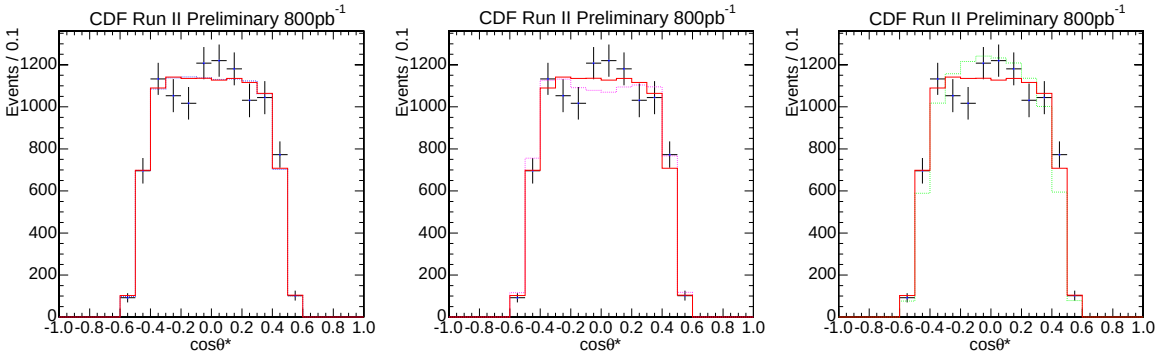

(a) $\cos\theta^*$: $p_T(\psi(2S))$ 5 - 7 GeV/c

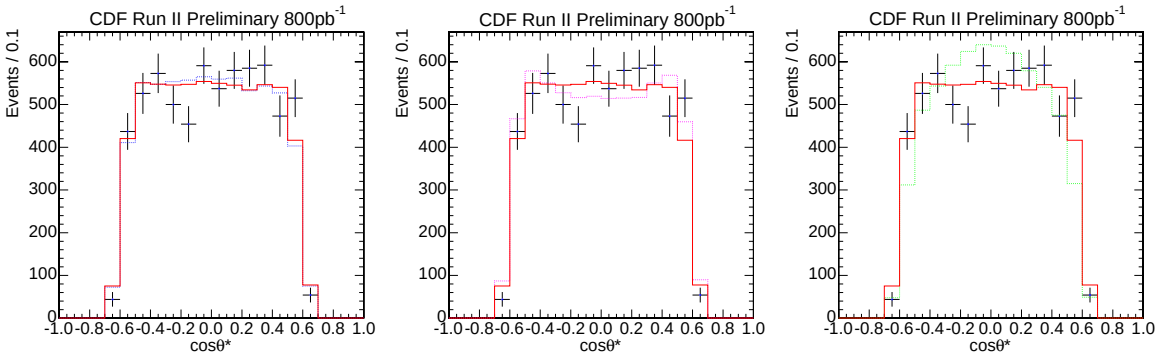

(b) $\cos\theta^*$: $p_T(\psi(2S))$ 7 - 10 GeV/c

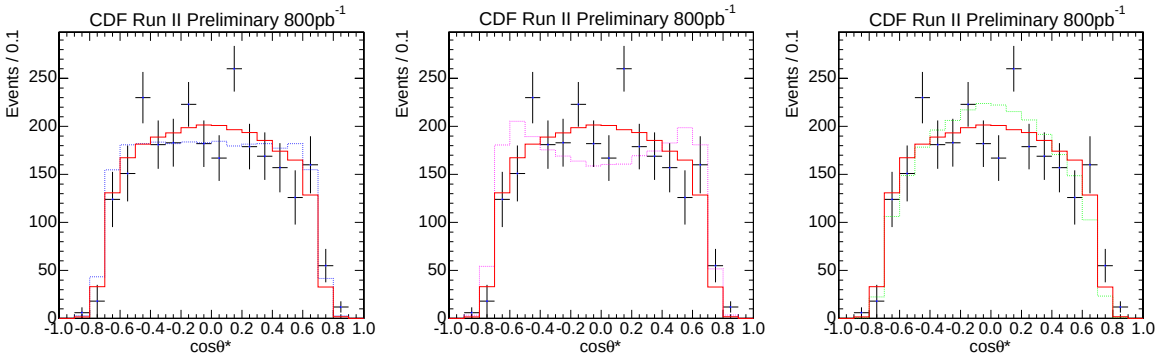

(c) $\cos\theta^*$: $p_T(\psi(2S))$ 10 - 30 GeV/c

Figure 3.9: The fitted $\cos\theta^*$ distribution with scaled MC templates for $p_T(\mu) > 2.0$ GeV/c: In the left, dashed blue line is unpolarized template. In the middle, dashed magenta line is transverse template. In the right, dashed green line is longitudinal template. The solid red line is the best fit line in that p_T bin.

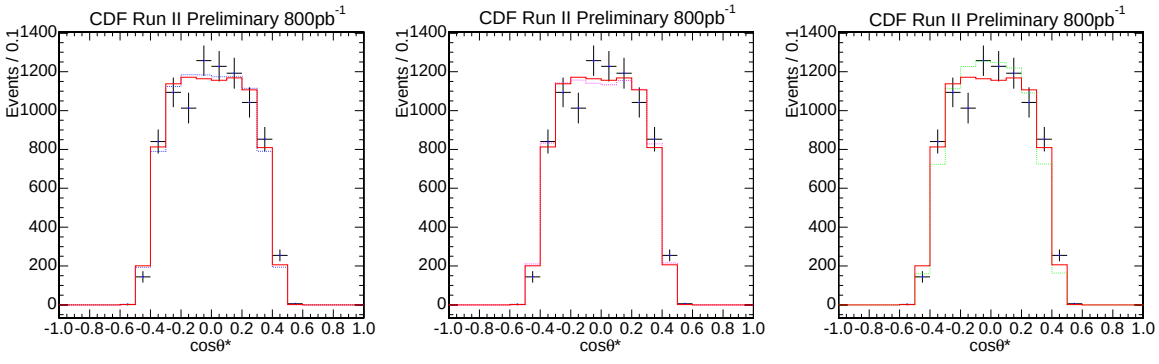

(a) $\cos\theta^*$: $p_T(\psi(2S))$ 5 - 7 GeV/c

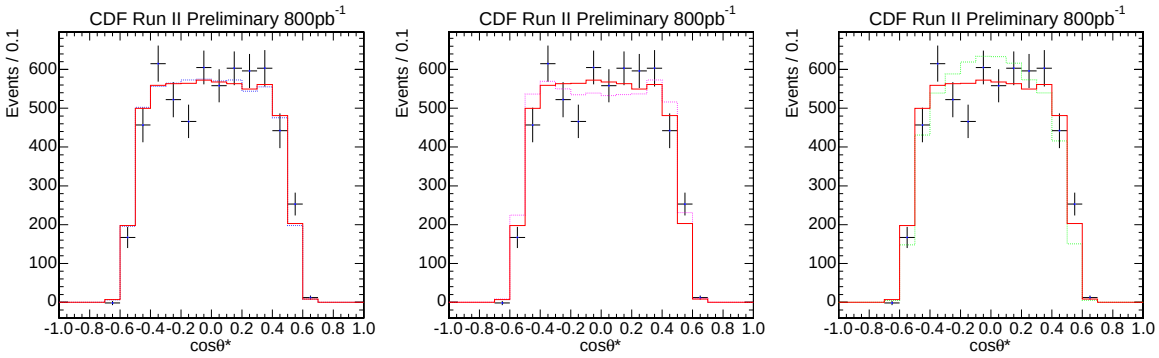

(b) $\cos\theta^*$: $p_T(\psi(2S))$ 7 - 10 GeV/c

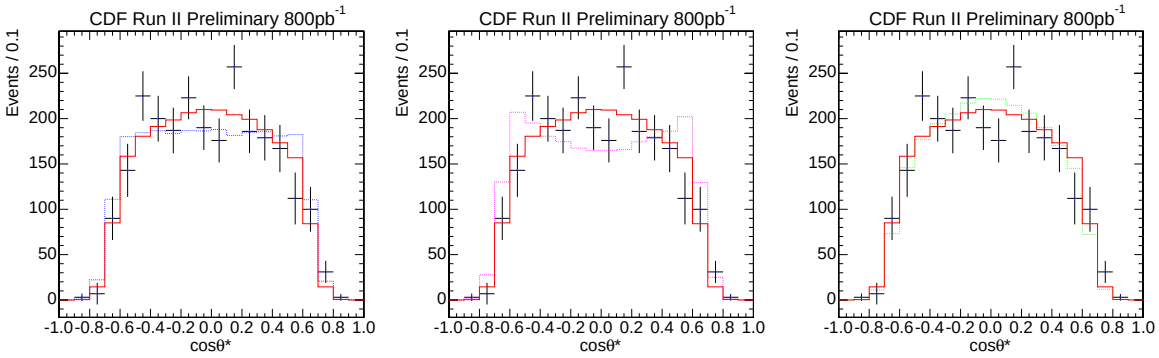

(c) $\cos\theta^*$: $p_T(\psi(2S))$ 10 - 30 GeV/c

Figure 3.10: The fitted $\cos\theta^*$ distribution with scaled MC templates for $p_T(\mu) > 2.25$ GeV/c: In the left, dashed blue line is unpolarized template. In the middle, dashed magenta line is transverse template. In the right, dashed green line is longitudinal template. The solid red line is the best fit line in that p_T bin.

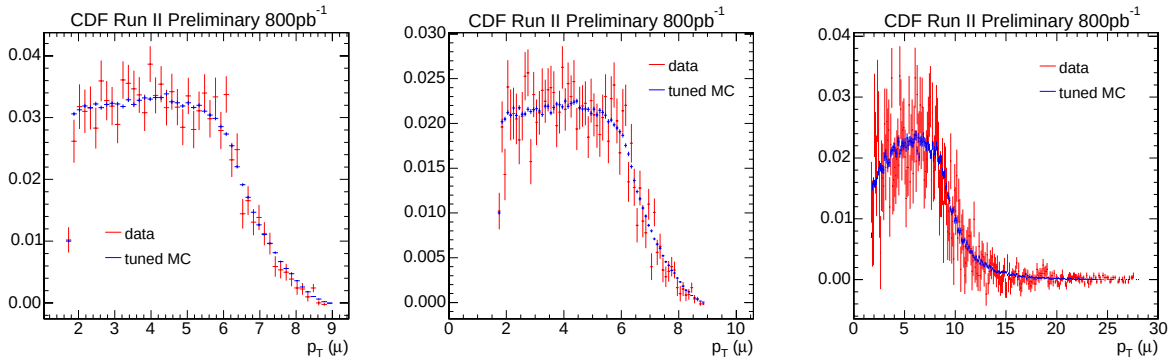

Figure 3.11: The data muon p_T spectrum in each p_T bin compared to tuned MC samples.

$p_T(\psi(2S))$ [GeV/c]	η_{fit}	F_B [%]	η_{prompt}	χ^2/d.o.f
5 - 7	0.016 ± 0.099	2.5 ± 1.3	0.018 ± 0.102	6.3/12
7 - 10	0.395 ± 0.156	3.4 ± 1.7	0.401 ± 0.161	16.8/14
10 - 30	0.458 ± 0.197	4.0 ± 2.9	0.468 ± 0.205	15.2/16

Table 3.9: The polarization fit of the data before Run 199025.

$p_T(\psi(2S))$ [GeV/c]	η_{fit}	F_B [%]	η_{prompt}	χ^2/d.o.f
5 - 7	0.149 ± 0.138	1.6 ± 1.5	0.148 ± 0.140	10.7/12
7 - 10	0.312 ± 0.124	2.2 ± 1.9	0.314 ± 0.127	29.5/14
10 - 30	0.698 ± 0.247	7.2 ± 3.4	0.735 ± 0.266	13.5/16

Table 3.10: The polarization fit of the data after Run 199025.

Systematic	Prompt $\psi(2S)$	B-decay $\psi(2S)$
Radiative tail event loss	± 0.01	-
Acceptance function	± 0.003	± 0.003
Background polarization	-	± 0.01

Table 3.11: Summary of the systematic uncertainties.

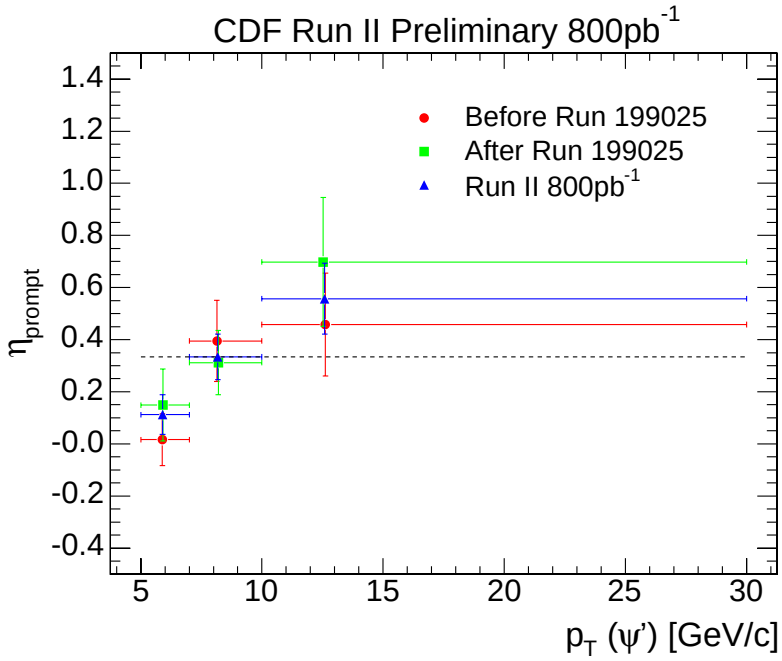

Figure 3.12: The prompt $\psi(2S)$ polarization in different datasets.

3.5 Result

The $\psi(2S)$ polarization from B-decay and from prompt production have been measured:

$$\eta_B = 0.19 \pm 0.09 \pm 0.01(syst.) \text{ or } \alpha_B = 0.36 \pm 0.25 \pm 0.03(syst.).$$

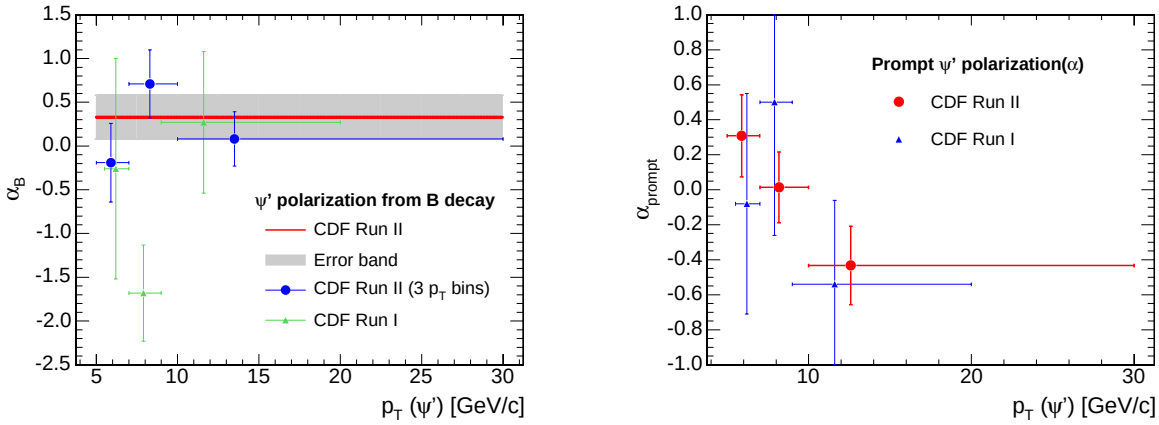

Figure 3.13: The $\psi(2S)$ polarization from B-decay (left) and from prompt production (right).

$p_T(\psi(2S))$ [GeV/c]	$< p_T >$ [GeV/c]	η_{prompt}	α_{prompt}	χ^2/d.o.f
5 - 7	6.2	$0.210 \pm 0.086 \pm 0.01$	$+0.306 \pm 0.235 \pm 0.027$	14.4/12
7 - 10	7.9	$0.327 \pm 0.089 \pm 0.01$	$+0.014 \pm 0.202 \pm 0.023$	18.7/14
10 - 30	11.6	$0.558 \pm 0.136 \pm 0.01$	$-0.433 \pm 0.224 \pm 0.016$	26.8/16

Table 3.12: Prompt $\psi(2S)$ polarization.

The measurement indicates that the prompt $\psi(2S)$ polarization in the highest p_T bin is longitudinal in contrast to the NRQCD prediction of large transverse polarization for the prompt $\psi(2S)$.

Chapter 4

$\psi(2S)$ Cross Section Measurement

"Science is facts; just as houses are made of stones, so is science made of facts; but a pile of stones is not a house and a collection of facts is not necessarily science."

— Henri Poincaré 1854–1912

The p_T- dependent differential cross section of $\psi(2S)$ is measured using the same dimuon decay channel ($\psi(2S) \to \mu^+\mu^-$) as the polarization analysis.

The $\psi(2S)$ differential cross section is evaluated using the expression

$$\frac{d\sigma(\psi(2S))}{dp_T} = \frac{N(\psi(2S))}{\mathcal{A} \cdot \epsilon_{reco} \cdot \int \mathcal{L}dt \cdot \Delta p_T} \quad , \tag{4.1}$$

where $d\sigma/dp_T$ is the average cross section of $\psi(2S)$ in the p_T bin integrated over $|y(\psi(2S))| \leq 0.6$, $\mathcal{A}$ is the trigger efficiency combined acceptance, ϵ_{reco} is the reconstruction efficiency, $\int \mathcal{L}dt$ is the integrated luminosity, and Δp_T is the size of the p_T bin.

An unbinned maximum likelihood fit is used to extract the $\psi(2S)$ events from the background, and to separate the prompt and b-decay processes simultaneously.

The prompt and b-decay processes have been separated by an impact parameter significance cut in the polarization analysis. This cut-based separation has its own strength in extracting the physical property (angular distribution) of each process as the cut can be optimized to make a sample which represents dominantly one of the processes with highly reduced contaminations from others regardless of the yield of

each process, although the yield still can be estimated from the ct distribution.

While in the cross section measurement, the yields of each process themselves are the most interesting quantity. The simultaneous mass-lifetime fit separates the prompt and b-decay process, and directly determines the yield of each process. Therefore the data selection procedure has been changed from the cut-based separation to the likelihood fit.

4.1 Yield

The same dataset which is described in Section 3.1 is used in the cross section measurement. The whole 1.1 fb^{-1} of integrated luminosity has been used since the cross section measurement does not depend on the COT performance critically. Most of the trigger requirements and offline selection cuts are the same as the polarization analysis. The compressed dimuon trigger datasets `xpmm0d`, `xpmm0h` and `xpmm0i` have been used and a different mass window of the invariant mass of the $\psi(2S)$ candidates is used to improve the fit process: $3500 \leq m_{\mu^+\mu^-} \leq 3800$ MeV/c as shown in Fig. 4.1a.

The unbinned maximum likelihood fit is performed to extract the $\psi(2S)$ events from the background events and at the same time the prompt and B-decay $\psi(2S)$ events are separated. The fit is mainly composed of two components - mass and lifetime.

The mass component separates the signal and the background. The signal function for the mass fit is modeled by a Crystal Ball function which describes the radiative tail well, together with a Gaussian and a first order polynomial is used to describe the mass background.

The Crystal-Ball function is an empirical probability density function introduced by the Crystal Ball Collaboration [32] to describe distributions with a low-side tail to a Gaussian shape. It consists of a Gaussian core portion and a power-law low-end tail, below a certain mass value.

$$Crystal\ Ball\ Function = \begin{cases} A \cdot e^{-\frac{(Et-Em)^2}{2\sigma^2}} & \text{if } \frac{Em-Et}{\sigma} > -\alpha \\ A \cdot \left(\frac{n}{\alpha}\right)^n \frac{e^{-\frac{\alpha^2}{2}}}{\left(\frac{Et-Em}{\sigma}+\frac{n}{\alpha}-\alpha\right)^n} & \text{if } \frac{Em-Et}{\sigma} \leq -\alpha \end{cases} \tag{4.2}$$

where Em is a fit parameter for the invariant mass peak, Et is the invariant mass of each event, A is the normalization constant, and empirical parameters α and n describe the tail function.

The separation of promptly-produced $\psi(2S)$ from $\psi(2S)$ originating in the decays of long-lived particles (mostly B-decays) is made by a proper time fit. A double Gaussian probability density function is used to describe the prompt component and the long-lived component is modeled by an exponential convoluted by a Gaussian.

$$EcG = \frac{1}{c\tau} exp\left[\frac{\sigma^2}{2c\tau^2} - \frac{x}{c\tau}\right] \cdot \left[1 - Freq\left(\frac{\sigma}{c\tau} - \frac{x}{\sigma}\right)\right] , \tag{4.3}$$

where $c\tau$ is the mean of proper decay length, σ is the error of $c\tau$, x is the proper decay length of each event, and $Freq(y)$ is the normal frequency function, $Freq(y) = \frac{1}{\sqrt{2\pi}} \int_{-\infty}^{y} e^{(-t^2/2)}\, dt$. The background component in the lifetime fit is modeled by the sum of a prompt term (double Gaussian), a symmetric long-lived (EcG) term, a positive-ct long-lived (EcG) term, and a negative-ct long-lived (EcG) term.

The likelihood, L, is defined as

$$\begin{aligned} L \;=\; & f_s P_s^{mass}\left(f_p P_p^{ct} + (1-f_p)\, P_{EcG}^{ct}\right) \\ & +(1-f_s) P_{bgnd}^{mass}\left(f_{symm} P_{symm}^{ct} + f_+ P_+^{ct} + f_- P_-^{ct}\right. \\ & \left.+(1 - f_{symm} - f_+ - f_-) P_p^{ct}\right) \quad , \end{aligned} \tag{4.4}$$

where

- f_s is the $\psi(2S)$ signal fraction from the total number of candidates in the fit,
- f_p is the fraction of prompt $\psi(2S)$,
- f_{sym} is the fraction of symmetric long-lived background,
- f_+ is the fraction of positive-ct long-lived background,
- f_- is the fraction of negative-ct long-lived background,
- P is the corresponding probability density function(PDF): P_s^{mass} is the normalized ($CrystalBallFunction$ + Gaussian), P_p^{ct} is the normalized double Gaussian, P_{EcG}^{ct} is the normalized exponential convoluted Gaussian, P_{bgnd}^{mass} is the normalized first order polynomial, P_{symm}^{ct} is the normalized function in which an exponential convoluted Gaussian for $Et > 0$ is reflected to the negative region,

$(EcG)((H[ct] - H[-ct]) \cdot ct)$, where $H[ct]$ is the Heaviside step function. P_+^{ct} is the normalized $H[ct] \cdot EcG$, P_-^{ct} is the normalized $H[-ct] \cdot (EcG)(-ct)$, P_p^{ct} is the normalized Gaussian.

4.1.1 Fixing Crystal Ball Function Parameters

Because the Crystal Ball function is an empirical description of data, its tail parameters have to be constrained by the physics of the process under study. We have used the high statistics of the full data set along with Monte Carlo simulation to fix the tail parameters in order to avoid unphysical fluctuations in the signal fraction or B meson proper decay length in the lower-statistics data from individual p_T bins.

Fixing tail parameters

The empirical parameters n and α which describe the radiative tail of the invariant mass distribution give a good description of the $\psi(2S)$ mass peak, as shown in Fig. 4.1. One sees from the overall data that the radiative tail accounts for 2 percent of the signal. The fit quality for both the mass and proper time projections is good.

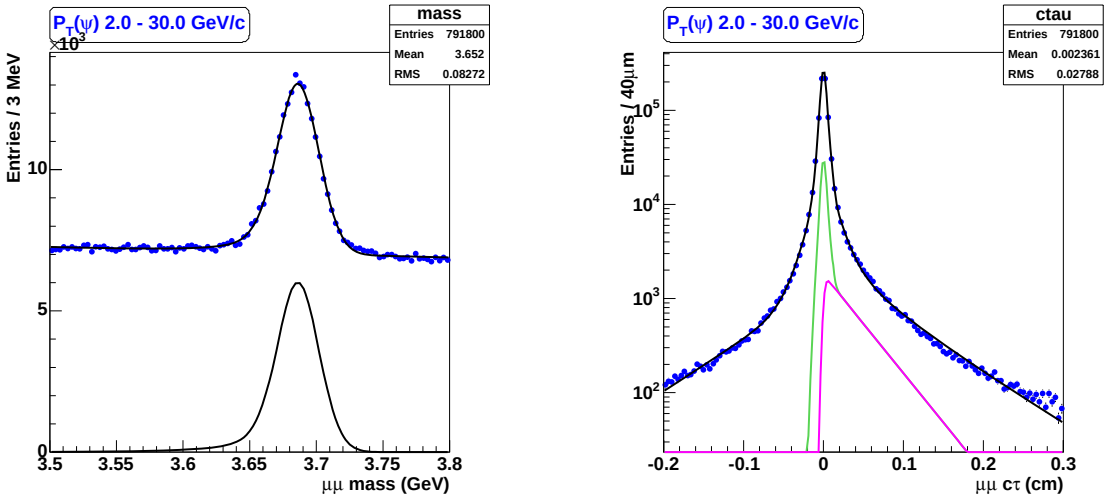

(a) Projection on the invariant mass

(b) A projection on the proper decay length

Figure 4.1: The projections on the invariant mass and the proper decay length for all events. The fit curve for signal and long-lived component is overlayed.

The fit works well for most p_T bins, as exemplified for a randomly-chosen p_T bin in Fig. 4.2. However, unconstrained fits for the tail parameters can be confused by background fluctuations. This can assign an unphysically large fraction of the so-called signal events to the tail region, distorting the mass fit and inflating the yield, as shown at left in Fig. 4.3a. In order to avoid these effects, the tail parameters are fixed, using data and Monte Carlo information. In this same bin, the plot in Fig. 4.3b shows a good fit after fixing the parameters according to the prescription to be explained below.

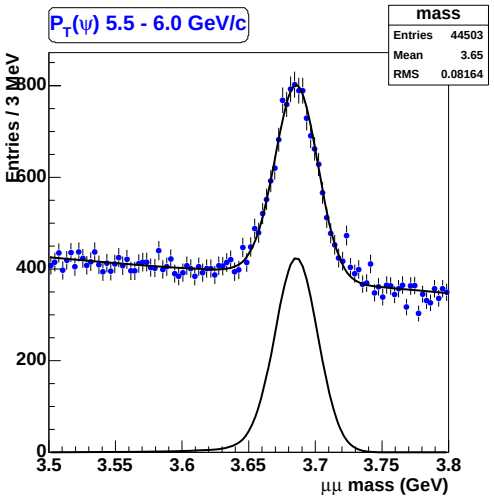

(a) A projection on the invariant mass

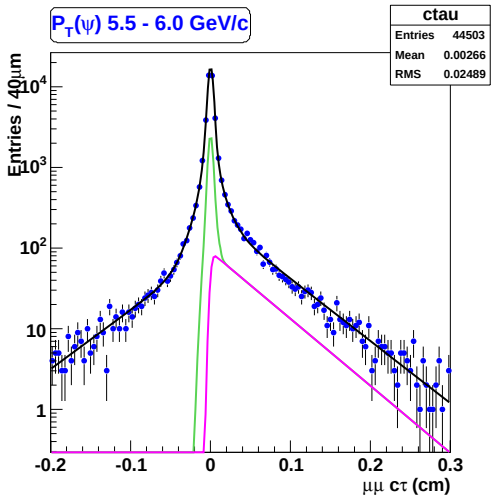

(b) A projection on the proper decay length

Figure 4.2: The projections on the invariant mass and the proper decay length in p_T range 5.5 - 6.0 GeV/c. The fit curve for signal and long-lived component is overlayed.

p_T-dependence of n & α

Radiation effects are dominated by inner bremsstrahlung in the muon channel at these energies due to the abrupt appearance of two charged particles at the instant that the $\psi(2S)$ decays. At these momentum values, muon external bremsstrahlung in material should have very little effect. Consequently, the radiative tail of the mass distribution is not expected to depend on $p_T(\psi(2S))$. This has been checked by looking both at the data and at MC samples generated with the `EvtGen PHOTOS` package to handle the final state radiation. The goal is to show that the tail parameters are independent of the p_T region both in Monte Carlo and in data. The data and MC samples are divided into 2 p_T

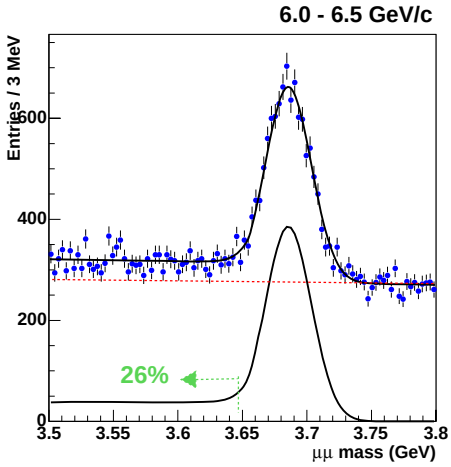

(a) Floating tail parameters

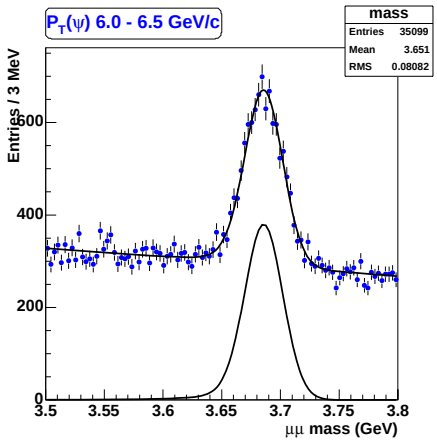

(b) Fixed tail parameters

Figure 4.3: (a) The empirical fit parameters,n and α confused by low-statistics and background fluctuation resulted in an overestimation of signal fraction. (b) The tail distribution is correctly described after fixing the parameters.

regions: 2-6 GeV/$c$and 6-30 GeV/c. The tail fit parameters for data and Monte Carlo are compared, and these parameters are fixed. The high p_T data is fitted and the fit quality is checked. For the low p_T data, the fit yields $n = 3.53 \pm 3.48$, $\alpha = 0.82 \pm 0.34$ with the projection fit probability 0.99. The data are very insensitive to the n parameter. Fitting the low p_T MC sample with a first order polynomial background yields $n = 4.50 \pm 0.14$, $\alpha = 0.81 \pm 0.12$. The α parameters for data and MC are in good agreement within errors. The n value is consistent, though one can hardly tell anything from the data. Next the high p_T data sample is fitted with fixing the n and α parameters from the low p_T Monte Carlo fit. The fit is excellent, with probability 0.83, as shown in Fig. 4.4. This leads to a conclusion that the radiative tail of the mass distribution does not depend on $p_T(\psi(2S))$.

The empirical parameters are fixed as $n = 4.50$ and $\alpha = 0.81$ for all p_T bins.

Weighting the Gaussian Fraction

As discussed in 4.1.1, the radiative tail fraction should be p_T independent, but the measured Gaussian width changes with p_T due to scattering and resolution. If the Gaussian fraction is allowed to float freely in each p_T bin, fluctuations can put more events into the tail even when the tail parameters are fixed. To prevent this unphysical situation, the fraction of events in the Gaussian peak need to be fixed while accounting

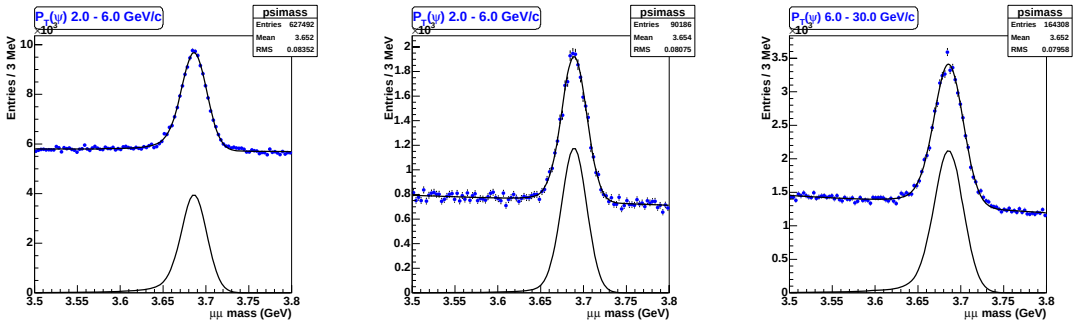

(a) Low-p_T data **(b)** Low-p_T MC **(c)** High-p_T data

Figure 4.4: The mass fit projection of different data and MC samples. In the MC sample (b), to emulate data background events, a randomly filled histogram with the same S/B ratio is added to the signal MC.

for the width changes with p_T.

While the CDF Monte Carlo does not predict the exact width of particle mass distributions correctly, it should represent well how the Gaussian width changes with p_T. As shown in Fig. 4.5, there is an increase of the width with increasing p_T in the MC sample.

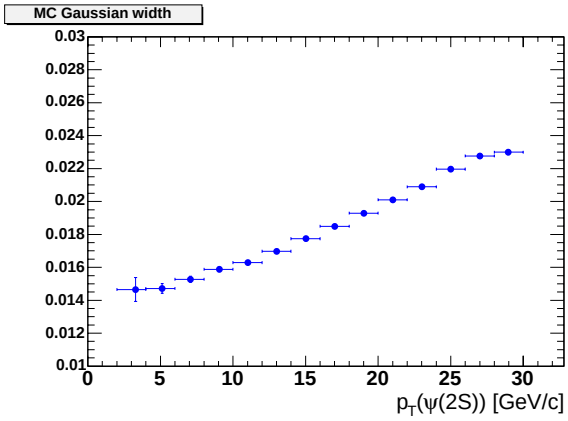

Figure 4.5: The MC sample Gaussian widths in p_T bins of 2 GeV/c.

Although the experimental widths are not the same as the MC predictions, the difference is assumed to be multiplicative and independent of p_T. A width scale factor s is introduced as

$$\sigma_{exp(p_T)} = s \cdot \sigma_{MC(p_T)} \ . \tag{4.5}$$

The scale factor s is determined by minimizing the total χ^2 for all of the mass fits in the 25 p_T bins while varying s. The χ^2 probabilities for different s values is shown in Fig. 4.6. The best scale factor choice was $s = 1.077$, which gave an overall χ^2-

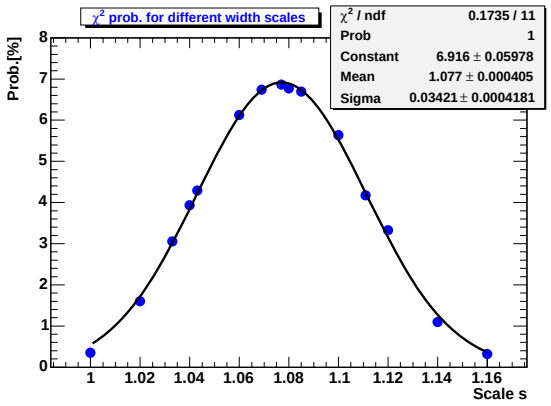

Figure 4.6: The χ^2-probabilities for different width scales s.

probability for the fits to the 25 mass plots of 8.4 % ($\sum \chi^2/ndf = 2597.9/2500$). The fit uncertainty for the scale factor is defined as the s value for which χ^2 increased by one unit. The result is $s = 1.077 \pm 0.008$. The effect of the s variation on yield will be discussed in Section 4.4.

B meson Proper Decay Length

The lifetime fit is used to separate the promptly produced $\psi(2S)$ from B-decay $\psi(2S)$. Although the lifetime doesn't affect the total yield, it directly affects the prompt fraction. In the lifetime fit, when the fit parameter of B-meson proper decay length is set to float in each p_T bin, a random fluctuation of the parameter over a large range was found, as shown in Fig. 4.7.

Based on an assumption that in the CDF data set there is equal production of B^+ and B^0 mesons, the average lifetime associates with the $\psi(2S)$ from B-decay will be their mean value. The world average of B meson proper decay length reported by Particle Data Group [5] is, $c\tau(B^\pm) = 491.1\ \mu m$, $c\tau(B^0) = 458.7\ \mu m$. And thus the average proper decay length, $c\overline{\tau} = \frac{c\tau_{B^\pm} + c\tau_{B^0}}{2} = 474.9\ \mu m$. Because these $\psi(2S)$ events are daughter of the B-hadrons and don't have a well-defined lifetime, another scale factor $s1$ is introduced here, such that effective average proper decay length, $c\tau_{eff} = s1 \cdot c\overline{\tau}$. The decay proper time $c\tau_{eff}$ should be independent of p_T, so a global

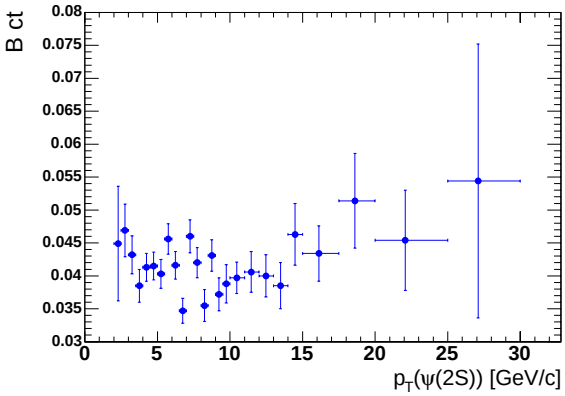

Figure 4.7: The B meson proper decay length in each p_T bin when it is allowed to float in the fit.

fit is performed with minimizing the total χ^2 of the lifetime fit to get the best scale factor $s1$. The total χ^2 values for different $s1$ are shown in Fig. 4.8. The best χ^2 value and the $\Delta\chi^2 = 1$ points $s1 = 1.1 \pm 0.025$. The effect of the $s1$ variation on yield and prompt $\psi(2S)$ fraction are discussed in Section 4.4.

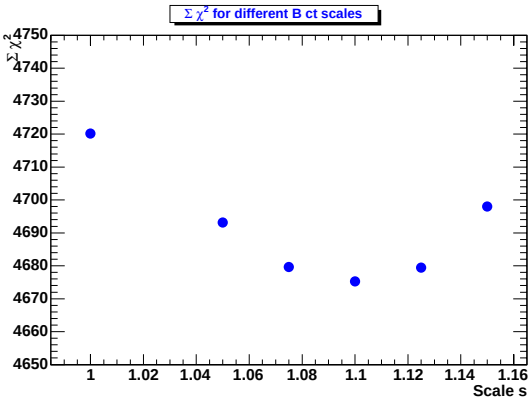

Figure 4.8: The total χ^2 of the lifetime fit for different $s1$.

Punzi Effect

In the unbinned maximum likelihood fit, the same σ_{ct} for signal and background is used. Using the same resolution for different distributions in unbinned maximum likelihood fit would cause a bias in general [33], which is often called as 'Punzi Effect'.

However, if the distribution of resolution is the same for all types of events, the probability density function of the resolution in the likelihood can be factored out, and it will not affect the maximization.

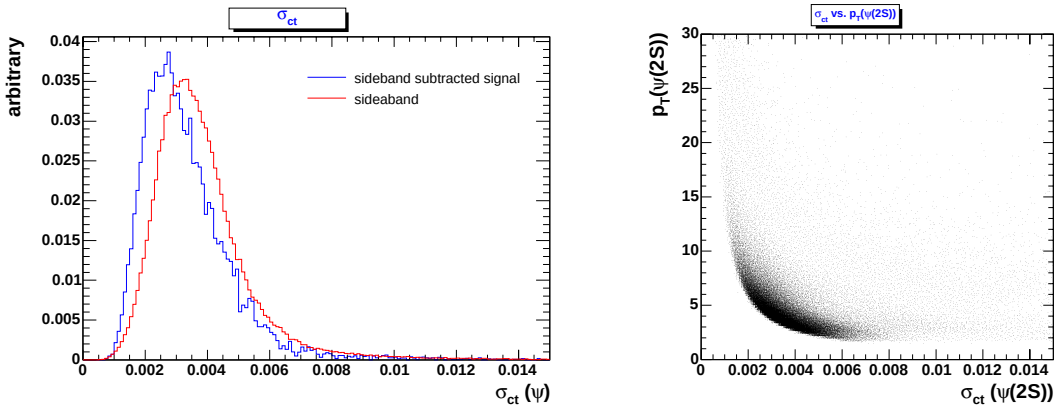

(a) The σ_{ct}-distribution for the integrated p_T

(b) The σ_{ct} vs p_T

Figure 4.9: (a) The σ_{ct} distribution for sideband subtracted signal and sideband events for the integrated p_T. Each distribution is normalized to unity. (b) A strong correction of σ_{ct} with $p_T(\psi(2S))$.

In Fig. 4.9a, the σ_{ct} distribution of sideband subtracted signal and sideband events for the integrated p_T indicate a possible Punzi effect in the fit. In this plot the sideband-subtracted total signal and the sideband σ_{ct} distributions have been separately normalized to unit areas. There is a strong correction of σ_{ct} with p_T as shown in Fig. 4.9b. Because the p_T distributions of signal and background are quite different, this biases the interpretation of Fig. 4.9a. Furthermore, since this measurement is done in p_T bins, the comparison of the σ_{ct} distributions should be in individual p_T bins, not as integrated quantities. The change in the signal to background(S/B) ratio with p_T can be seen in Fig. 4.10.

The σ_{ct} distribution in each p_T bin has been investigated. The σ_{ct} distributions of sideband subtracted signal and sideband events in each p_T bin lie atop each other as shown in Fig. 4.11. Therefore there is no Punzi effect.

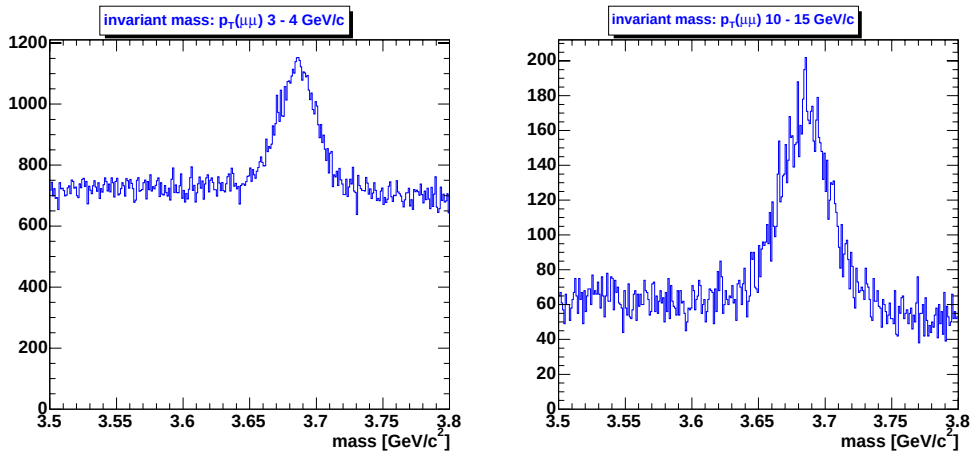

Figure 4.10: The invariant mass plots of two p_T bins. At the higher p_T, the S/B has increased.

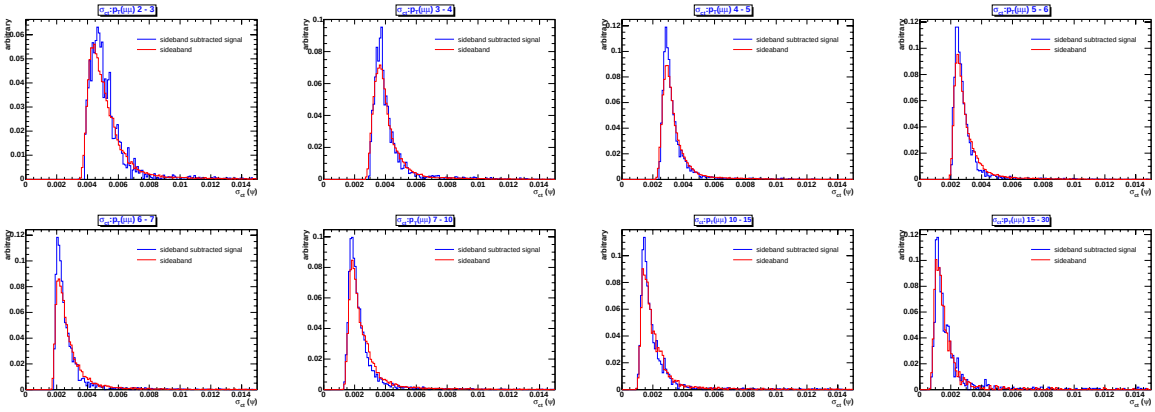

Figure 4.11: The σ_{ct} distribution in each p_T bin.

4.1.2 Alternative Mass Parametrization

The mass signal has been modeled by using the Crystal Ball function with a single Gaussian. An alternative parametrization is a double Gaussian function. Since the effect of this alternative mass parametrization is only on the yield, a binned likelihood fit is performed with the mass component alone for the whole p_T region. The fit projections of two different mass parametrization for the p_T range, $2-30$ GeV/c, is shown in Fig. 4.12. The signal yield for the double Gaussian function is 85460.6 ± 534.5 with narrow Gaussian width 0.0147 ± 0.003, tail fraction 0.032 ± 0.011, χ^2/ndf$= 80.2/100$. Using the Crystal Ball function parametrization, the signal yield is 84325.1 ± 548.5 with

Gaussian width 0.0157 ± 0.001, tail fraction 0.036 ± 0.012, χ^2/ndf$= 92.2/100$. The double Gaussian parametrization returned a slightly better χ^2 value. This cannot be used to decide between models because both χ^2 fit probabilities are acceptable. As one sees in Fig. 4.12b, the double Gaussian fits the high side tail of the dimuon mass distribution better than the Crystal Ball Function. This is the origin of the yield difference in the two fits.

The variation in the signal yield of the Crystal Ball function parametrization from the double Gaussian model is 1.3 %. Half the variation from different parametrization is assigned as a systematic uncertainty in Section 4.4.

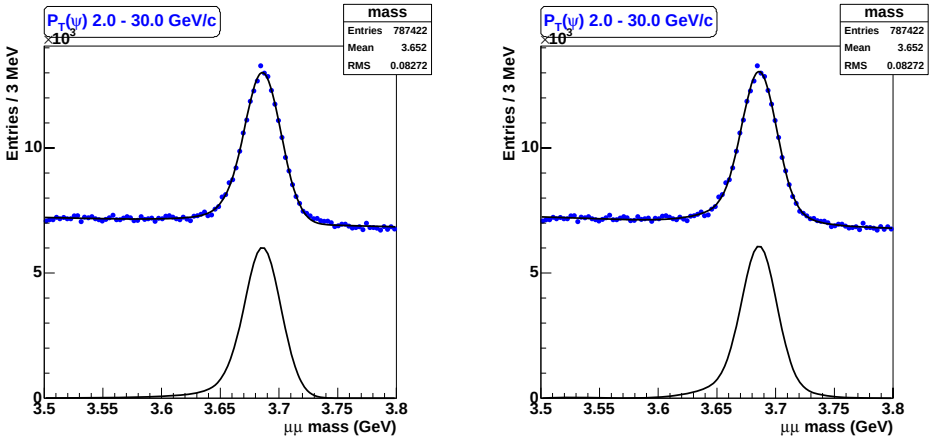

(a) The Crystal Ball function with a single Gaussian

(b) The double Gaussian

Figure 4.12: The mass fit projection of different mass parametrizations.

4.1.3 Fit Results

The p_T-range (2 GeV/c- 30 GeV/c) of $\psi(2S)$ has been divided into 25 bins as listed in Table 4.2. In each p_T-bin, the signal yield and the prompt fraction have been extracted by the maximum unbinned likelihood fit in which the Gaussian width of the Crystal-Ball function is fixed by using Eq. 4.5 with $s = 1.077$ and the B meson proper decay length is fixed at $c\tau_{eff} = s1 \cdot c\overline{\tau}$ with $s1 = 1.10$.

An example of the projections of the unbinned maximum likelihood fit result is shown in Fig. 4.2. The projections of the fit for each p_T bin is available in Appendix C, along with the residual plots in the various p_T bins. Table C.1 in Appendix C gives the

fit χ^2 and probabilities for the mass projections of the likelihood fit in each p_T bin. All the probabilities are acceptable: the worst is 1.5 %, and the probability for the fit in all 25 bins together is 8.8 %.

Prompt Fraction

The $\psi(2S)$ mesons originating from prompt production mechanisms have been separated by utilizing the proper decay length information in the lifetime component of the likelihood fit. The prompt fraction fit parameter f_p in Eq. 4.4 is used to determine the prompt $\psi(2S)$ yield in each p_T bin. The prompt fraction in each p_T bin is shown in Fig. 4.13.

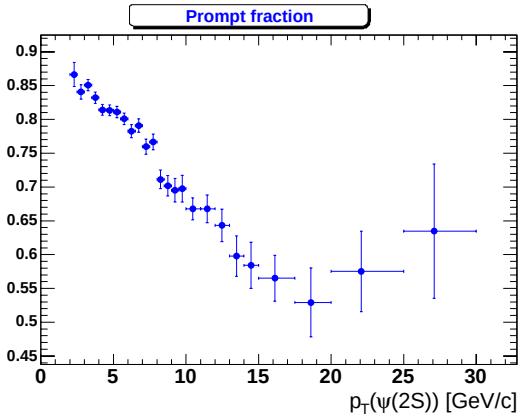

Figure 4.13: The prompt fraction of the $\psi(2S)$ candidates in each p_T bin.

Monte Carlo Studies of the Prompt ct Distribution

In order to see if the apparent substructure in Fig. 4.13 is real or statistical, several checks are done. First, the fits are performed again with using a prompt Gaussian whose width in each p_T bin was fixed from the Monte Carlo. The ct distribution of the unpolarized Monte Carlo sample in 2 GeV/c p_T bin is well described by a double Gaussian as shown in Fig. 4.14b. There is tiny fraction of events outside the prompt Gaussian fit. This fraction is independent of p_T and 0.9 % at all p_T as shown in Fig. 4.14c.

The yield is corrected for this loss with systematic uncertainty of 0.3 %. The MC

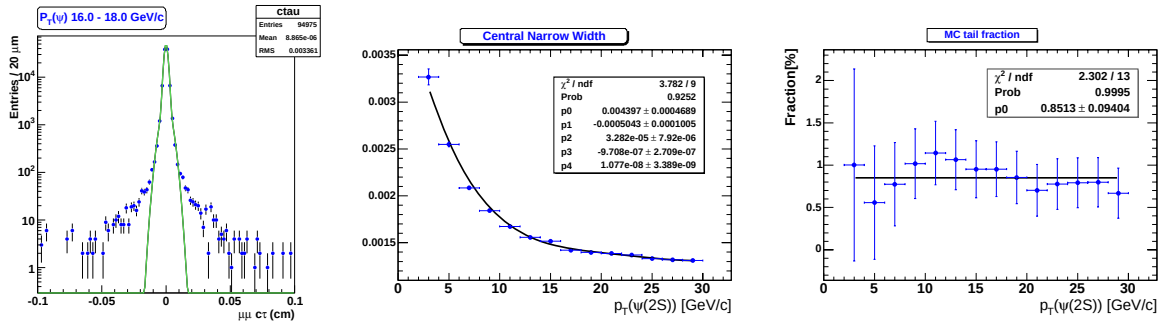

(a) The MC ct distribution

(b) The MC narrow Gaussian width

(c) MC events outside Gaussian fit

Figure 4.14: The prompt fraction in MC.

narrow Gaussian width vs. p_T is shown in Fig. 4.14b. The decrease in narrow Gaussian width with p_T is well described by a 4th order polynomial fit (Fit Probability 93 %). This result is used to fix the narrow Gaussian width in the fit to the data. As can be seen from Table 4.1, there is very little change in the prompt fraction. This shows that parameter correlations in the fitting fuction are not responsible for any structure.

Second, it is checked whether all the data were consistent with a linear p_T dependence. Excepting the two largest-p_T points, the data fit well to a straight line, shown in Fig. 4.15. The small jumps in the prompt fraction are statistical fluctuations.

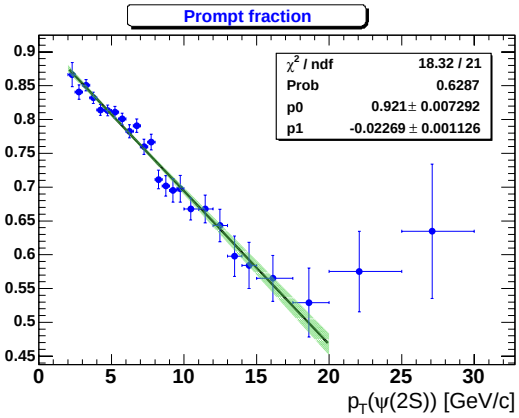

Figure 4.15: The prompt fraction fitted with a straight line. The green band denotes the error corridor.

A possible systematic uncertainty on the prompt fraction from p_T binning is also checked. All the p_T bins are shifted by 0.25 GeV/c and the fit is performed. As shown

$P_T(\psi(2S))$	$< P_T >$	Prompt Fraction	
		Fixed Gaussian Width	Floated Gaussian Width
2.0-2.5	2.30	0.868 $\pm$ 0.018	0.866 $\pm$ 0.018
2.5-3.0	2.77	0.841 $\pm$ 0.011	0.841 $\pm$ 0.011
3.0-3.5	3.25	0.854 $\pm$ 0.008	0.851 $\pm$ 0.008
3.5-4.0	3.75	0.834 $\pm$ 0.008	0.832 $\pm$ 0.008
4.0-4.5	4.24	0.815 $\pm$ 0.008	0.814 $\pm$ 0.008
4.5-5.0	4.74	0.811 $\pm$ 0.008	0.813 $\pm$ 0.008
5.0-5.5	5.24	0.810 $\pm$ 0.008	0.811 $\pm$ 0.009
5.5-6.0	5.74	0.804 $\pm$ 0.008	0.801 $\pm$ 0.009
6.0-6.5	6.24	0.786 $\pm$ 0.009	0.783 $\pm$ 0.010
6.5-7.0	6.74	0.793 $\pm$ 0.010	0.791 $\pm$ 0.010
7.0-7.5	7.24	0.766 $\pm$ 0.011	0.760 $\pm$ 0.011
7.5-8.0	7.74	0.762 $\pm$ 0.012	0.767 $\pm$ 0.012
8.0-8.5	8.24	0.705 $\pm$ 0.014	0.711 $\pm$ 0.014
8.5-9.0	8.74	0.699 $\pm$ 0.015	0.702 $\pm$ 0.015
9.0-9.5	9.24	0.698 $\pm$ 0.017	0.695 $\pm$ 0.017
9.5-10	9.74	0.700 $\pm$ 0.021	0.698 $\pm$ 0.020
10 - 11	10.46	0.665 $\pm$ 0.016	0.668 $\pm$ 0.016
11 - 12	11.46	0.659 $\pm$ 0.020	0.668 $\pm$ 0.021
12 - 13	12.47	0.643 $\pm$ 0.024	0.643 $\pm$ 0.024
13 - 14	13.48	0.595 $\pm$ 0.030	0.598 $\pm$ 0.030
14 - 15	14.48	0.585 $\pm$ 0.034	0.584 $\pm$ 0.034
15 - 17.5	16.12	0.565 $\pm$ 0.034	0.565 $\pm$ 0.034
17.5 - 20	18.61	0.530 $\pm$ 0.059	0.529 $\pm$ 0.051
20 - 25	22.08	0.581 $\pm$ 0.059	0.575 $\pm$ 0.060
25 - 30	27.09	0.637 $\pm$ 0.096	0.635 $\pm$ 0.099

Table 4.1: The prompt fraction of the fixed narrow Gaussian width fit and the floated width fit.

in the Fig. 4.16, there is no evidence of binning systematic.

$P_T(\psi(2S))$	$< P_T >$	Total	Signal	Prompt	Prompt fraction	B-decay
2.0-2.5	2.30	35495	2240.5 ± 115.7	1941.2 ± 139.9	0.866 ± 0.018	299.3 ± 55.1
2.5-3.0	2.77	96473	5729.8 ± 184.2	4816.8 ± 215.9	0.841 ± 0.011	913.0 ± 90.4
3.0-3.5	3.25	118868	7931.8 ± 205.4	6746.9 ± 241.4	0.851 ± 0.008	1184.9 ± 97.4
3.5-4.0	3.75	108198	7853.8 ± 196.4	6535.1 ± 229.8	0.832 ± 0.008	1318.7 ± 99.3
4.0-4.5	4.24	91373	8053.2 ± 183.3	6556.8 ± 212.4	0.814 ± 0.008	1496.4 ± 97.2
4.5-5.0	4.74	72106	7440.6 ± 165.2	6052.5 ± 193.8	0.813 ± 0.008	1388.1 ± 90.3
5.0-5.5	5.24	57055	6273.9 ± 148.2	5087.3 ± 174.0	0.811 ± 0.009	1186.6 ± 81.9
5.5-6.0	5.74	44503	5888.4 ± 133.8	4715.7 ± 157.7	0.801 ± 0.009	1172.7 ± 77.2
6.0-6.5	6.24	35099	5316.4 ± 121.0	4160.1 ± 146.7	0.783 ± 0.010	1156.3 ± 78.3
6.5-7.0	6.74	26908	4447.0 ± 107.6	3516.6 ± 129.1	0.791 ± 0.010	930.4 ± 66.5
7.0-7.5	7.24	20253	3571.5 ± 94.2	2713.0 ± 111.9	0.760 ± 0.011	858.5 ± 63.0
7.5-8.0	7.74	15954	3129.4 ± 84.9	2398.9 ± 101.6	0.767 ± 0.012	730.5 ± 56.3
8.0-8.5	8.24	12103	2510.5 ± 74.9	1785.8 ± 87.5	0.711 ± 0.014	724.7 ± 55.8
8.5-9.0	8.74	9569	2039.8 ± 66.9	1431.4 ± 77.7	0.702 ± 0.015	608.4 ± 50.7
9.0-9.5	9.24	7532	1618.0 ± 59.5	1124.7 ± 69.7	0.695 ± 0.017	493.3 ± 46.4
9.5-10	9.74	6020	1344.9 ± 53.8	938.2 ± 64.1	0.698 ± 0.020	406.7 ± 42.9
10 - 11	10.46	8676	1910.8 ± 64.9	1275.8 ± 74.3	0.668 ± 0.016	635.0 ± 52.5
11 - 12	11.46	5733	1348.9 ± 53.2	900.8 ± 63.3	0.668 ± 0.021	448.1 ± 45.4
12 - 13	12.47	3916	908.6 ± 44.3	584.4 ± 50.4	0.643 ± 0.024	324.2 ± 37.7
13 - 14	13.48	2818	640.2 ± 37.6	382.8 ± 41.6	0.598 ± 0.030	257.4 ± 34.2
14 - 15	14.48	2001	465.0 ± 32.0	271.6 ± 34.6	0.584 ± 0.034	193.4 ± 29.2
15 - 17.5	16.12	3061	584.6 ± 39.0	330.3 ± 42.0	0.565 ± 0.034	254.3 ± 36.9
17.5 - 20	18.61	1671	291.7 ± 28.7	154.4 ± 30.1	0.529 ± 0.051	137.3 ± 28.4
20 - 25	22.08	1462	229.9 ± 27.5	132.2 ± 29.5	0.575 ± 0.060	97.7 ± 25.4
25 - 30	27.09	575	83.6 ± 17.8	53.1 ± 19.6	0.635 ± 0.099	30.5 ± 14.8

Table 4.2: Summary of the unbinned maximum likelihood fit.

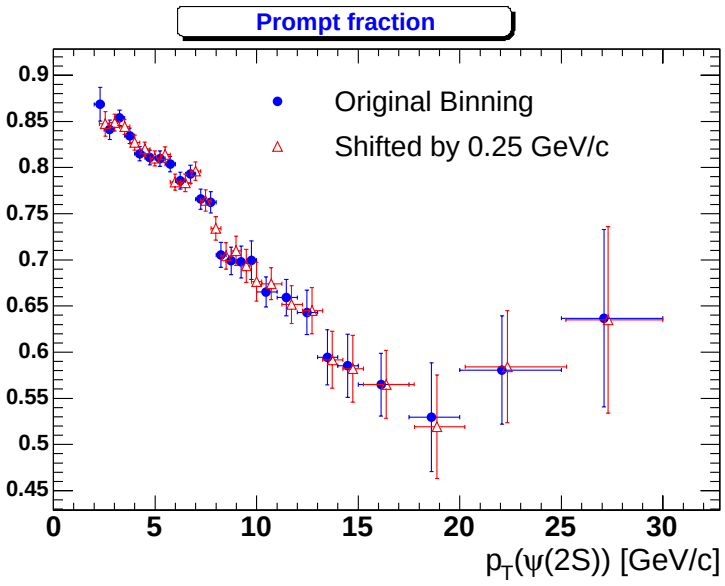

Figure 4.16: The prompt fraction with the original binning and the shifted binning.

4.2 Acceptance and Efficiencies

4.2.1 Acceptance and Trigger Efficiency

The $\psi(2S)$ acceptance is calculated using Monte Carlo events. Since the kinetmatic acceptance as a function of p_T is sensitive to the $\psi(2S)$ polarization, the acceptance based on an unpolarized MC sample could not be simply adopted. The J/ψ and $\psi(2S)$ polarization have been measured in CDF Run II[39], shown in Figure 4.17. The $\psi(2S)$ polarization in each p_T bin is listed in Table 4.3.

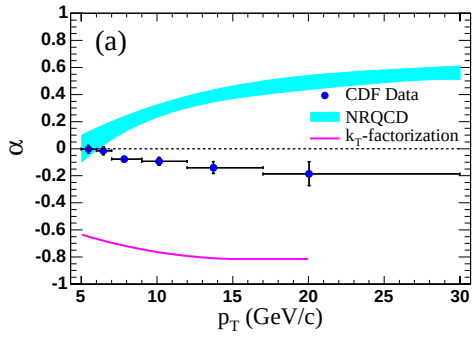

(a) The J/ψ polarization

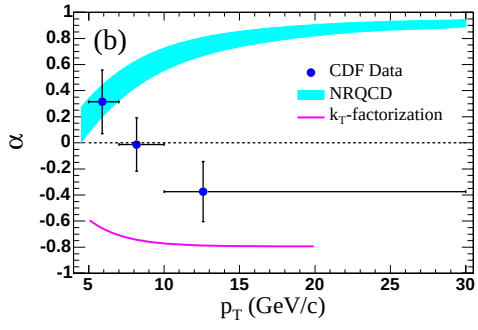

(b) The $\psi(2S)$ polarization

Figure 4.17: The CDF Run II J/ψ and $\psi(2S)$ polarization measurement.

$p_T(\psi(2S))$ [GeV/c]	Mean p_T [GeV/c]	η_{prompt}	α_{prompt}	χ^2/d.o.f
5 - 7	6.2	$0.210 \pm 0.086 \pm 0.01$	$+0.306 \pm 0.235 \pm 0.027$	14 .4/12
7 - 10	7.9	$0.327 \pm 0.089 \pm 0.01$	$+0.014 \pm 0.202 \pm 0.023$	18 .7/14
10 - 30	11.6	$0.558 \pm 0.136 \pm 0.01$	$-0.433 \pm 0.224 \pm 0.016$	26 .8/16

Table 4.3: Prompt $\psi(2S)$ polarization.

The statistical uncertainty on $\psi(2S)$ is much larger than that for the J/ψ. The α parameters in individual p_T bins are too imprecise to be used as reliable polarization estimators for the acceptance correction. Theoretically, the prompt polariztion for the two states is expected to be the same, both in NRQCD and alternative models[16, 34]. The difficulty with using the measured J/ψ polarization to describe that of the $\psi(2S)$ is that there is about 30 % feeddown from higher charmonium states in the J/ψ signal that may dilute the prompt polarization. To be conservative, a method to correlate the three $\psi(2S)$ measurements and invoke the kinematic zero of polarization at p_T = 0 needs to be found. Two approaches are tried: first, to define a polarization function suggested by the data itself, and second, to follow the lead from theory and say that the $\psi(2S)$ prompt polarization is the same as that measured for the J/ψ.

In the first approach it is noted that the experimental $\psi(2S)$ polarization is consistent with being zero not only at p_T= 0 but at all p_T. The fit for the three measured points to zero has a $\chi^2 = 5.45$ for 3 degrees of freedom (no average taken here), for a probability of 14 %. This suggests that using a constant effective polarization parameter (α_{eff}) is a reasonable description of the data. The average of the three measured points is $\alpha_{eff} = 0.01 \pm 0.13$. In the second approach the $\psi(2S)$ and the measured J/ψ prompt polarizations were taken to be equal.

As shown in Fig. 4.18, the J/ψ polarization as a function of p_T is fitted and this fit and its uncertainty is used to compute the acceptance and the systematic uncertainty due to polarization. Extrapolating the fitted function and error to the three $\psi(2S)$ data points, the χ^2 probability that the prompt $\psi(2S)$ polarization is consistent with that of the J/ψ is 41 % ($\chi^2/ndf = 2.9/3$).

Of the two approaches, the one using just the $\psi(2S)$ data is more conservative. A single α_{eff} value for the whole p_T range is used to compute the acceptance and its uncertainty: $\alpha_{eff} = 0.01 \pm 0.13$. The overall systematic uncertainty (not just that due to the acceptance) would be reduced by about 20 % of itself and the average

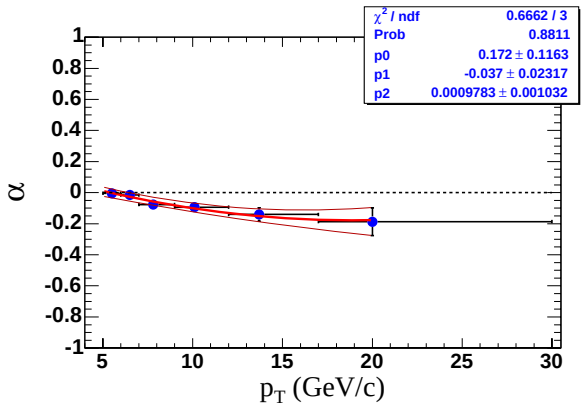

Figure 4.18: The fit curve of the J/ψ polarization.

acceptance would go down by 2.3 % of itself if the second method is used. This is a relatively small change and convinces that using the first method is indeed robust and conservative.

Because the tracking proceeds from the large-radius detectors inward, the geometric acceptance calculated for the prompt events is insensitive to small displacements of the dimuon decay point. We use the same geometric acceptance for the b-decay. No systematic uncertainty is assigned for this assumption. The polarization dependence is recalculated, using the measured b-decay polarization [39].

The effective polarizations for the prompt and b-decay are different. In order to take account for this, a weighted average of the acceptances is used in each p_T bin for the inclusive differential cross section. The acceptances for the prompt and b-decay in each p_T bin is averaged by using the prompt fraction listed in Table 4.2 and then the resulting acceptance is applied to the signal events to get the inclusive cross section.

The $\psi(2S)$ MC samples are made with fixed polarization (0 or -1) and flat distributions in p_T, η and ϕ. Events are produced using a single particle gun `FakeEv`, and decayed to a muon pair by `EvtGen`. After the CDF detector simulation, the events are reconstructed with the data based trigger efficiencies [26]. Then the combined geometrical acceptance and trigger efficiencies, $\mathcal{A}$, is measured by calculating the ratio

$$\mathcal{A} = \frac{N^{rec}(p_T)}{N^{gen}(p_T)} , \tag{4.6}$$

where $N^{rec}(p_T)$ is the number of the reconstructed Monte Carlo events and $N^{gen}(p_T)$ is the number of the generated events.

$P_T(\psi(2S))$	$< P_T >$	$\mathcal{A}_{\alpha=0.0}$	$\mathcal{A}_{\alpha=-1.0}$	$\mathcal{A}_{eff}$
2.0-2.5	2.30	0.0056 $\pm$ 0.0002	0.0089 $\pm$ 0.0005	0.0056 $\pm$ 0.0002
2.5-3.0	2.77	0.0134 $\pm$ 0.0003	0.0193 $\pm$ 0.0007	0.0134 $\pm$ 0.0003
3.0-3.5	3.25	0.0206 $\pm$ 0.0004	0.0306 $\pm$ 0.0009	0.0206 $\pm$ 0.0004
3.5-4.0	3.75	0.0270 $\pm$ 0.0005	0.0389 $\pm$ 0.0010	0.0270 $\pm$ 0.0005
4.0-4.5	4.24	0.0356 $\pm$ 0.0006	0.0520 $\pm$ 0.0012	0.0356 $\pm$ 0.0006
4.5-5.0	4.74	0.0417 $\pm$ 0.0006	0.0616 $\pm$ 0.0014	0.0417 $\pm$ 0.0006
5.0-5.5	5.24	0.0530 $\pm$ 0.0007	0.0742 $\pm$ 0.0015	0.0530 $\pm$ 0.0007
5.5-6.0	5.74	0.0601 $\pm$ 0.0007	0.0856 $\pm$ 0.0017	0.0601 $\pm$ 0.0007
6.0-6.5	6.24	0.0738 $\pm$ 0.0008	0.1001 $\pm$ 0.0019	0.0738 $\pm$ 0.0008
6.5-7.0	6.74	0.0824 $\pm$ 0.0009	0.1129 $\pm$ 0.0020	0.0824 $\pm$ 0.0009
7.0-7.5	7.24	0.0909 $\pm$ 0.0010	0.1251 $\pm$ 0.0021	0.0909 $\pm$ 0.0010
7.5-8.0	7.74	0.1004 $\pm$ 0.0010	0.1357 $\pm$ 0.0022	0.1004 $\pm$ 0.0010
8.0-8.5	8.24	0.1100 $\pm$ 0.0011	0.1496 $\pm$ 0.0024	0.1100 $\pm$ 0.0011
8.5-9.0	8.74	0.1198 $\pm$ 0.0011	0.1579 $\pm$ 0.0025	0.1198 $\pm$ 0.0011
9.0-9.5	9.24	0.1300 $\pm$ 0.0012	0.1678 $\pm$ 0.0026	0.1300 $\pm$ 0.0012
9.5-10	9.74	0.1354 $\pm$ 0.0012	0.1707 $\pm$ 0.0026	0.1354 $\pm$ 0.0012
10 - 11	10.46	0.1450 $\pm$ 0.0009	0.1911 $\pm$ 0.0031	0.1450 $\pm$ 0.0009
11 - 12	11.46	0.1530 $\pm$ 0.0009	0.1988 $\pm$ 0.0032	0.1530 $\pm$ 0.0009
12 - 13	12.47	0.1631 $\pm$ 0.0010	0.2103 $\pm$ 0.0033	0.1631 $\pm$ 0.0010
13 - 14	13.48	0.1712 $\pm$ 0.0010	0.2169 $\pm$ 0.0034	0.1712 $\pm$ 0.0010
14 - 15	14.48	0.1810 $\pm$ 0.0011	0.2240 $\pm$ 0.0035	0.1810 $\pm$ 0.0011
15 - 17.5	16.12	0.1959 $\pm$ 0.0007	0.2390 $\pm$ 0.0023	0.1959 $\pm$ 0.0007
17.5 - 20	18.61	0.2152 $\pm$ 0.0007	0.2610 $\pm$ 0.0024	0.2152 $\pm$ 0.0007
20 - 25	22.08	0.2320 $\pm$ 0.0006	0.2748 $\pm$ 0.0018	0.2320 $\pm$ 0.0006
25 - 30	27.09	0.2474 $\pm$ 0.0006	0.2889 $\pm$ 0.0018	0.2474 $\pm$ 0.0006

Table 4.4: Summary of acceptance with different α's and the effective acceptance at α_{eff}.

4.2.2 Reconstruction Efficiencies

The total reconstruction efficiency is the product of several factors:

$$\epsilon_{reco} = \epsilon^2_{COT} \cdot \epsilon^2_{SVX} \cdot \epsilon^2_{CMU} \cdot \epsilon^2_{\chi^2} \cdot \epsilon_{z_0} \cdot \epsilon_{\Delta z_0} \quad , \tag{4.7}$$

Table 4.5: Summary of reconstruction efficiencies

Selection	Efficiency	Reference
COT offline	$\epsilon(p_T > 1.5) = 99.61 \pm 0.02 \pm 0.91$ %	CDF Note 6394
SVX II offline	96 ± 0.8 %	CDF Note 8289
Muon offline	$\epsilon(p_T > 2.0) = 96.6 \pm 1.4$ %	CDF Note 8289
${\chi^2}_\mu \leq 9.0$	99.6 ± 1.5 %	CDF Note 8289
$Z_0 \leq 60cm$	95.6 ± 0.3 %	CDF Note 7935
$\Delta z_0 \leq 5cm$	99.9 ± 0.2 %	CDF Note 8289

where ϵ_{COT} is the COT-tracking efficiency, ϵ_{SVX} is the SVX II offline cut efficiency, ϵ_{CMU} is the muon reconstruction efficiency in muon chamber, ϵ_{χ^2} is the muon chamber χ^2 cut efficiency, ϵ_{z_0} and $\epsilon_{\Delta z_0}$ are the vertex quality cut efficiencies. Table 4.5 summarizes the offline reconstruction efficiencies. For the SVX II offline cut efficiency, in each $\psi(2S)$ p_T bin, the sideband subtracted muon p_T spectrum has been used to estimate a weighted average for the SVX II offline cut efficiency. The efficiency varies from 0.952 to 0.966 over the $\psi(2S)$ p_T range. A p_T-independent value 0.96 ± 0.008 has been used accomodating the small p_T-dependent variation. The data included in this analysis were collected prior to the significant luminosity increases in February - June, 2006. There are small luminosity-weighted changes included in the efficiencies quoted, as described in the notes.

4.3 Luminosity

The $\psi(2S)$ cross section analysis uses a 1.1fb^{-1}data set collected using the dimuon trigger path (`JPSI_CMUCMU1.5` or `JPSI_CMUCMU1.5_DPS`). As the instantaneous luminosity has increased, the unprescaled `JPSI_CMUCMU1.5` trigger path was changed to the dynamically prescaled trigger path, `JPSI_CMUCMU1.5_DPS` [1] has been implemented to cope with the increased trigger rate.

The Dynamic-Prescale(DPS) trigger selects events with a varying prescale in the course of a run. In order to calculate the correct luminosity for the dynamically prescaled trigger path, `JPSI_CMUCMU1.5_DPS`, we developed the DPS Accounting tool[35]

[1] `L2_TWO_CMU1.5_PT1.5_DPHI120_OPPQ_DPS`. From June, 2004, Physics Table `PHYSICS_2_05_v-10`.

which calculates the effective luminosity in each run section. The integrated luminosity for the trigger path `JPSI_CMUCMU1.5` is 280 pb^{-1} and the effective luminosity for the dynamically prescaled trigger path `JPSI_CMUCMU1.5_DPS` is 656 pb^{-1}. After multiplying the correction factor of 1.019, the total (effective) luminosity for this analysis is found to be 954 pb^{-1}.

4.4 Systematic Uncertainties

Two scale factors, s and $s1$, are used in the unbinned maximum likelihood fit as described in previous sections. To investigate the systematic uncertainty from the scale factors s and $s1$, the combinations of $(s, s1) = (1.069, 1.10), (1.085, 1.10), (1.077, 1.075),$ and $(1.077, 1.125)$ have been tried. The largest variation is assigned as a systematic uncertainty in the signal yield. And the $s1$ variations with $s = 1.077$ are used to estimate the systematic uncertainty in the prompt fraction. The variation of the signal yield and prompt fraction in each p_T bin is summarized in Table 4.6.

As discussed in Section 4.2, the systematic uncertainty from the $\psi(2S)$ polarization is estimated from the averaged $\psi(2S)$ polarization. The systematic changes from the α_{eff} in each p_T bin are listed in Table 4.6.

In order to estimate the systematic uncertainty from the dimuon trigger efficiencies [26], the trigger efficiency($\epsilon_{trigger}$) is varied by 1σ and the changes in the signal yield is looked at. The result is shown in Table 4.6.

The systematic uncertainty from the reconstruction efficiency is calculated to be 2.5 % from Table 4.5. And the uncertainty on the luminosity is reported to be 6 %.

A different mass probability density function (PDF) using a double Gaussian for the mass signal than the Crystal Ball function is also tried as described in Section 4.1.2. A mass PDF systematic uncertainty is assgined as 0.7 %.

All the systematic uncertainties are summarized in Table 4.7.

$P_T(\psi(2S))$	$< P_T >$	s & $s1$ [%]	Prompt [%]	$\epsilon_{trigger}$[%]	$\mathcal{A}$[%]
2.0-2.5	2.30	0.26	0.08	3.09	7.14
2.5-3.0	2.77	0.48	0.17	2.37	5.97
3.0-3.5	3.25	0.25	0.09	1.62	6.31
3.5-4.0	3.75	0.24	0.13	1.20	5.56
4.0-4.5	4.24	0.41	0.17	2.55	5.90
4.5-5.0	4.74	0.29	0.31	1.29	6.24
5.0-5.5	5.24	0.30	0.97	1.58	5.28
5.5-6.0	5.74	0.26	0.15	1.55	5.49
6.0-6.5	6.24	0.32	0.14	1.70	4.61
6.5-7.0	6.74	0.42	0.25	1.49	4.85
7.0-7.5	7.24	0.24	0.17	1.18	4.84
7.5-8.0	7.74	0.51	0.20	1.75	4.58
8.0-8.5	8.24	0.42	0.55	1.53	4.64
8.5-9.0	8.74	0.27	0.20	1.68	4.17
9.0-9.5	9.24	0.27	0.23	1.44	3.77
9.5-10	9.74	0.16	0.13	1.57	3.40
10 - 11	10.46	0.35	0.23	1.26	4.14
11 - 12	11.46	0.33	0.31	1.69	3.92
12 - 13	12.47	0.22	0.26	1.36	3.74
13 - 14	13.48	0.34	0.44	1.45	3.45
14 - 15	14.48	0.17	0.46	1.37	3.09
15 - 17.5	16.12	0.27	0.37	1.37	2.86
17.5 - 20	18.61	0.21	0.17	1.39	2.79
20 - 25	22.08	0.39	0.30	1.40	2.41
25 - 30	27.09	0.48	0.21	1.57	2.18

Table 4.6: Systematic Uncertainty in Yield in Percent.

4.5 Result

The differential cross section is calculated using Eq. 4.1. The inclusive and prompt $\psi(2S)$ cross sections are listed in Table 4.8, and the differential cross section results with statistical uncertainties are shown in Figure 4.19 and 4.20 for the inclusive and prompt $\psi(2S)$ correspondingly.

Source	Systematic Uncertainty
Luminosity	± 6 %
Reconstruction Efficiency	± 2.5 %
Trigger Efficiency	$\pm (1.2 - 3.1)$ %
Mass PDF	± 0.7 %
Prompt Fraction	± 0.3 %
$\psi(2S)$ Polarization	$\pm (2.2 - 7.1)$ %
Mass and Lifetime Modeling	$\pm (0.2 - 0.5)$ %

Table 4.7: Summary of the systematic uncertainty.

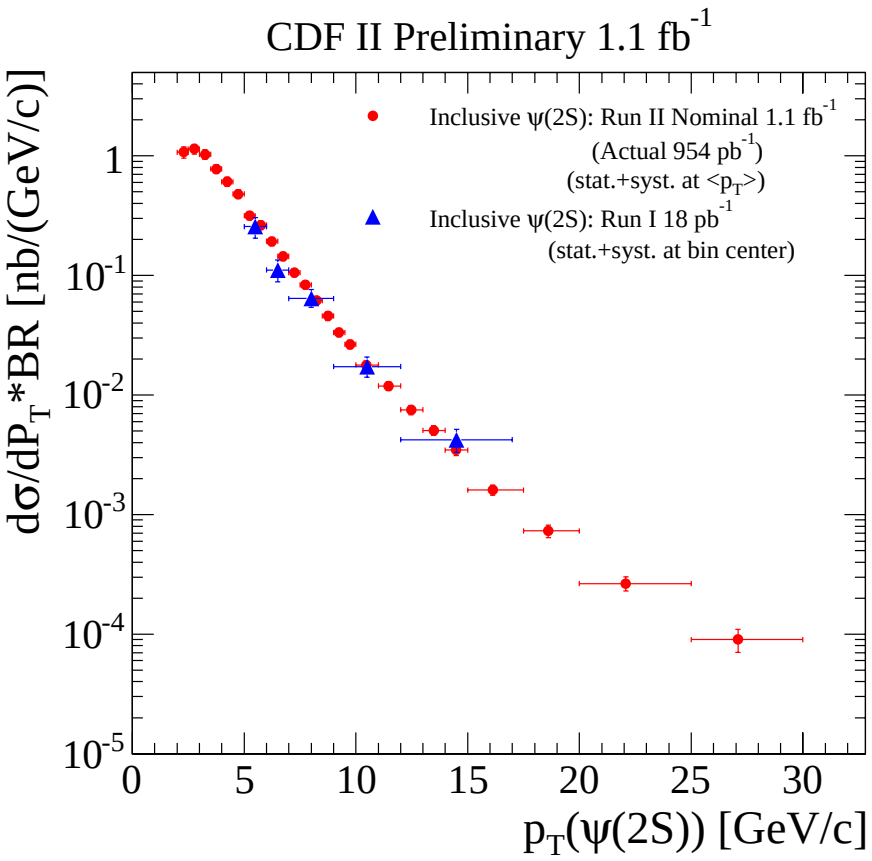

Figure 4.19: The inclusive $\psi(2S)$ differential cross section.

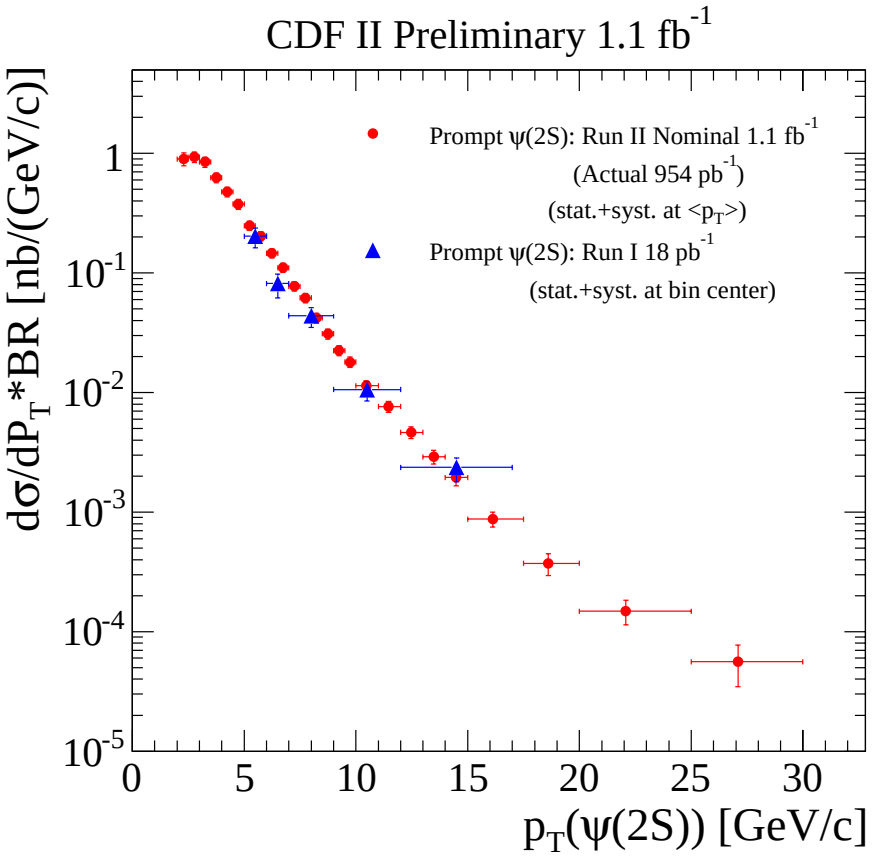

Figure 4.20: The prompt $\psi(2S)$ differential cross section.

$P_T(\psi(2S))$	Inclusive $\frac{d\sigma}{dp_T} \cdot$ Br[nb/(GeV/c)]	Prompt $\frac{d\sigma}{dp_T} \cdot$ Br[nb/(GeV/c)]	B-decay $\frac{d\sigma}{dp_T} \cdot$ Br[nb/(GeV/c)]
2.0-2.5	1075 ± 74 ± 103	899 ± 65 ± 89	176 ± 32 ± 14
2.5-3.0	1142 ± 47 ± 99	932 ± 42 ± 84	210 ± 21 ± 16
3.0-3.5	1030 ± 34 ± 90	849 ± 30 ± 77	181 ± 15 ± 13
3.5-4.0	778 ± 25 ± 64	628 ± 22 ± 53	151 ± 11 ± 11
4.0-4.5	608 ± 18 ± 53	478 ± 15 ± 43	131 ± 8 ± 10
4.5-5.0	481 ± 14 ± 41	376 ± 12 ± 34	104 ± 7 ± 8
5.0-5.5	317 ± 10 ± 26	249 ± 9 ± 21	68 ± 5 ± 5
5.5-6.0	263 ± 8 ± 22	203 ± 7 ± 17	60 ± 4 ± 4
6.0-6.5	193 ± 6 ± 15	146 ± 5 ± 12	47 ± 3 ± 3
6.5-7.0	144 ± 5 ± 11	111 ± 4 ± 9	34 ± 2 ± 2
7.0-7.5	106 ± 4 ± 8.2	77.4 ± 3.2 ± 6.2	28.3 ± 2.1 ± 2.0
7.5-8.0	83.6 ± 3.1 ± 6.5	62.0 ± 2.6 ± 5.0	21.6 ± 1.7 ± 1.5
8.0-8.5	61.7 ± 2.6 ± 4.7	42.1 ± 2.1 ± 3.4	19.6 ± 1.5 ± 1.4
8.5-9.0	45.9 ± 2.1 ± 3.4	31.0 ± 1.7 ± 2.4	14.9 ± 1.2 ± 1.0
9.0-9.5	33.4 ± 1.7 ± 2.4	22.4 ± 1.4 ± 1.7	11.0 ± 1.0 ± 0.7
9.5-10	26.6 ± 1.5 ± 1.9	18.0 ± 1.2 ± 1.3	8.6 ± 0.9 ± 0.6
10 - 11	17.8 ± 0.8 ± 1.3	11.4 ± 0.7 ± 0.9	6.4 ± 0.5 ± 0.4
11 - 12	11.9 ± 0.7 ± 0.9	7.63 ± 0.54 ± 0.58	4.26 ± 0.43 ± 0.3
12 - 13	7.52 ± 0.52 ± 0.54	4.65 ± 0.40 ± 0.35	2.88 ± 0.34 ± 0.19
13 - 14	5.06 ± 0.42 ± 0.36	2.90 ± 0.32 ± 0.21	2.16 ± 0.29 ± 0.14
14 - 15	3.46 ± 0.33 ± 0.24	1.95 ± 0.25 ± 0.14	1.52 ± 0.23 ± 0.10
15 - 17.5	1605 ± 152 ± 110	874 ± 111 ± 62	731 ± 106 ± 48
17.5 - 20	730 ± 103 ± 51	372 ± 73 ± 26	358 ± 74 ± 23
20 - 25	265 ± 45 ± 18	148 ± 33 ± 10	117 ± 30 ± 8
25 - 30	90 ± 26 ± 6	56 ± 21 ± 4	34 ± 17 ± 2

Table 4.8: The differential cross section (pb/GeV/c) times the dimuon branching fraction as a function of p_T for $|y(\psi(2S))| \leq 0.6$. Note: for $p_T >$ 15 GeV/$c$the cross section units change to fbGeV/c.

The differential cross section of $\psi(2S)$ from B-decays is shown in Fig. 4.21. The prompt and B-decay $\psi(2S)$ cross section are compared to the J/ψ cross section [29] as shown in Fig. 4.22a and Fig. 4.22b. The prompt and B-decay $\psi(2S)$ differential cross section has softer slope than the slope of J/ψ differential cross section. The ratio, $\frac{d\sigma}{dp_T} \cdot BR(\psi(2S))$ / $\frac{d\sigma}{dp_T} \cdot BR(J/\psi)$, from prompt and B-decay production is shown in Fig. 4.23a and Fig. 4.23b compared to Run I result [36] in Fig. 4.24.

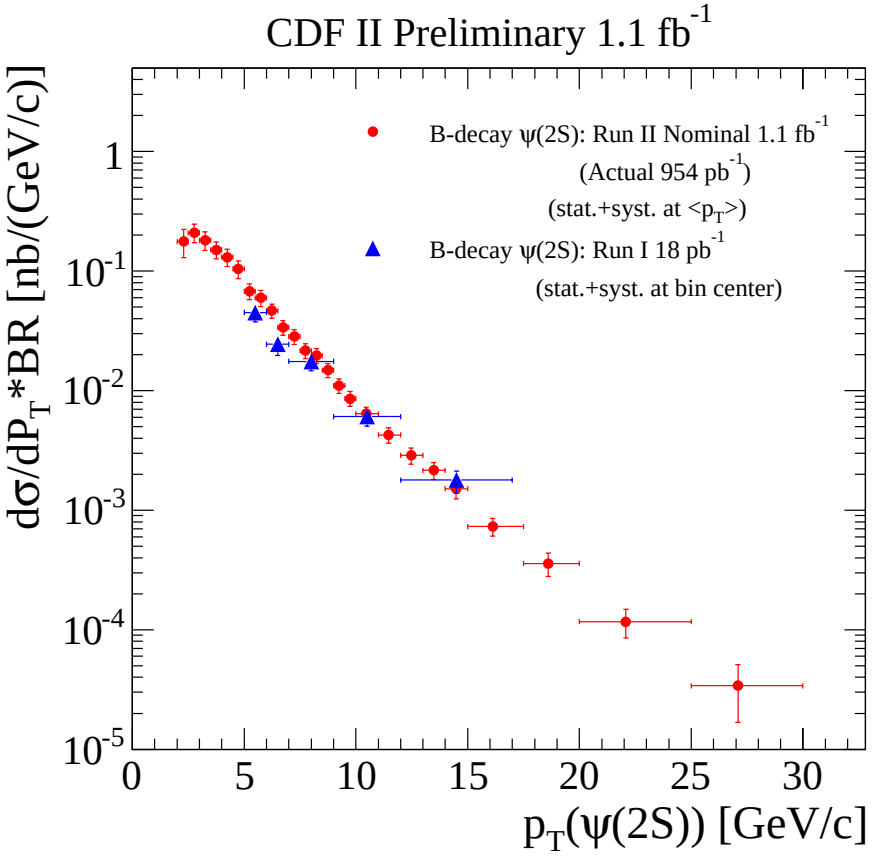

Figure 4.21: The $\psi(2S)$ from B-decay differential cross section.

The integrated differential cross section multiplied by the branching ratio for dimuon decay is measured to be:

$$\sigma(p\overline{p} \to \psi(2S)X, |y(\psi(2S))| < 0.6,\ p_T > 2\ \text{GeV}/c)_{1.96} \cdot Br(\psi(2S) \to \mu^+\mu^-) = 3.17 \pm 0.04(\text{stat}) \pm 0.28(\text{syst})\ \text{nb}.$$

In the CDF Run I, the inclusive $\psi(2S)$ cross section is measured for $p_T(\psi(2S))$ ex-

ceeding 5 GeV/c[36]:

$$\sigma(p\overline{p} \to \psi(2\mathrm{S})X, |\eta| < 0.6, p_T > 5 \text{ GeV}/c)_{1.80} \cdot Br(\psi(2\mathrm{S}) \to \mu^+\mu^-) \\ = 0.57 \pm 0.04(\mathrm{stat})^{+0.08}_{-0.09}(\mathrm{syst}) \text{ nb}$$

To compare with the Run I measurement, we have integrated cross section of inclusive $\psi(2\mathrm{S})$ with $p_T > 5$ GeV/c. The cross section is found to be:

$$\sigma(p\overline{p} \to \psi(2\mathrm{S})X, |y(\psi(2\mathrm{S}))| < 0.6, p_T > 5 \text{ GeV}/c)_{1.96} \cdot Br(\psi(2\mathrm{S}) \to \mu^+\mu^-) \\ = 0.68 \pm 0.01(\mathrm{stat}) \pm 0.06(\mathrm{syst}) \text{ nb}$$

These measurements show that the integrated cross section has increased by $18 \pm 19\ \%$ compared to the Run I measurement. This is quite consistent with the prediction in the reference[37] of an increase of $14 \pm 8\ \%$ for prompt J/ψ and $\psi(2\mathrm{S})$ integrated cross sections when the Tevatron center of mass energy is raised from 1.80 to 1.96 TeV.

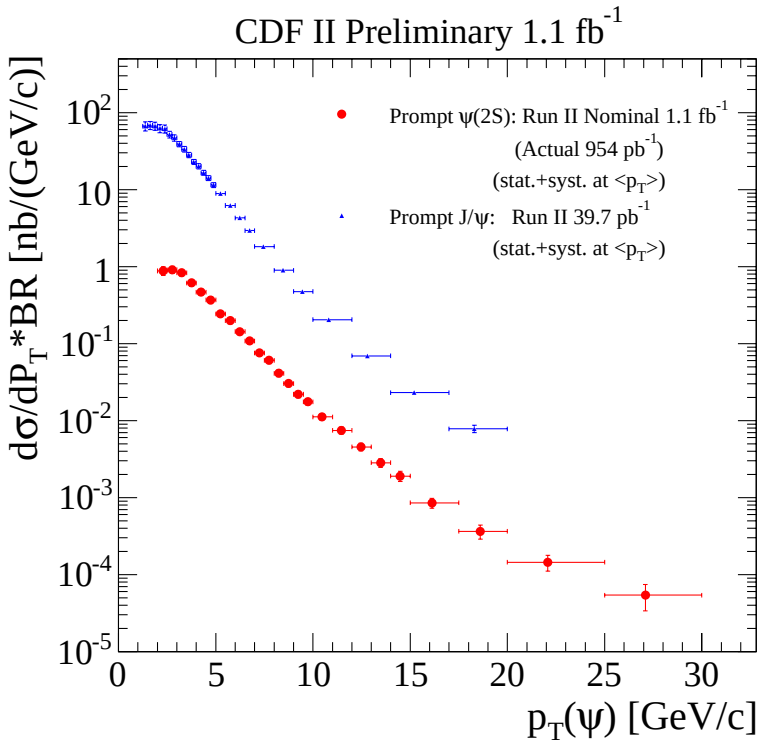

(a) The prompt ψ

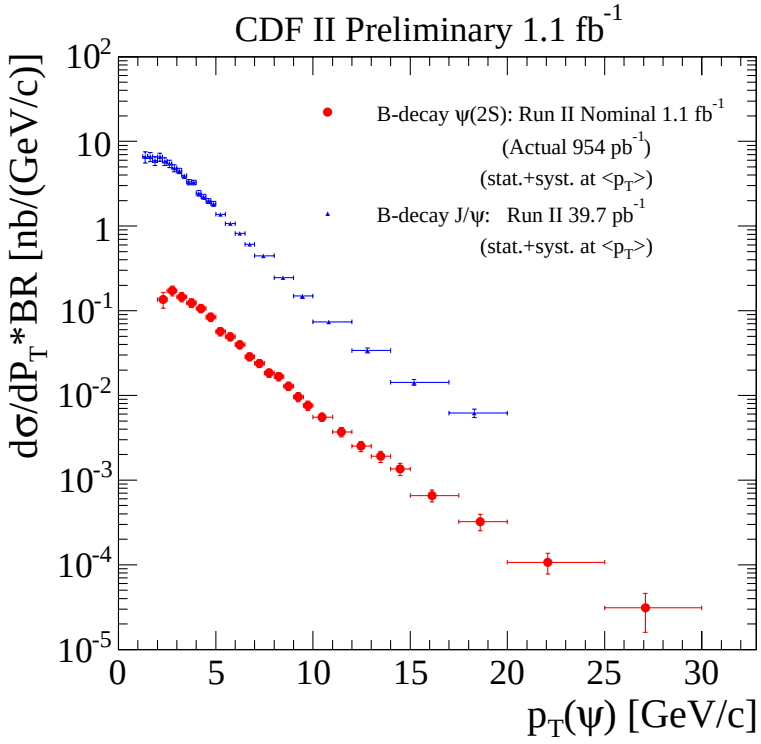

(b) The ψ from B-decay

Figure 4.22: The p_T dependent differential cross section of $\psi(2S)$ and J/ψ.

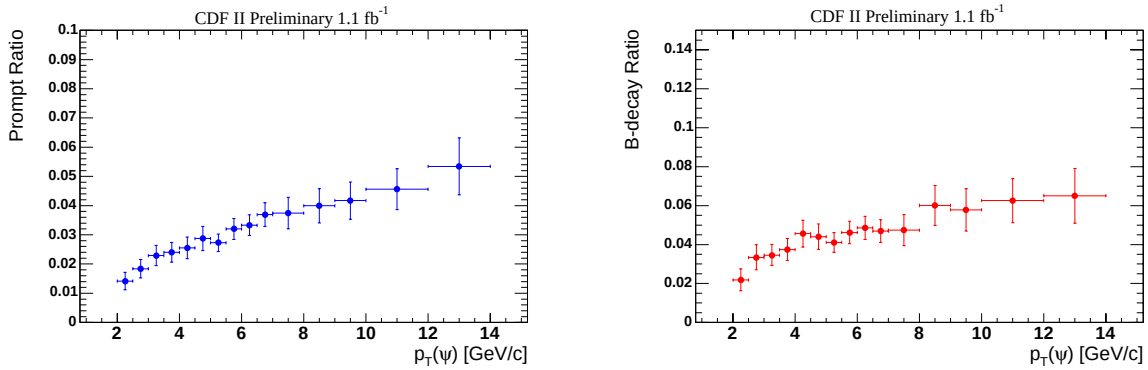

(a) The prompt ψ **(b)** The ψ from B-decay

Figure 4.23: The ratio of p_T dependent differential cross section of $\psi(2S)$ and J/ψ.

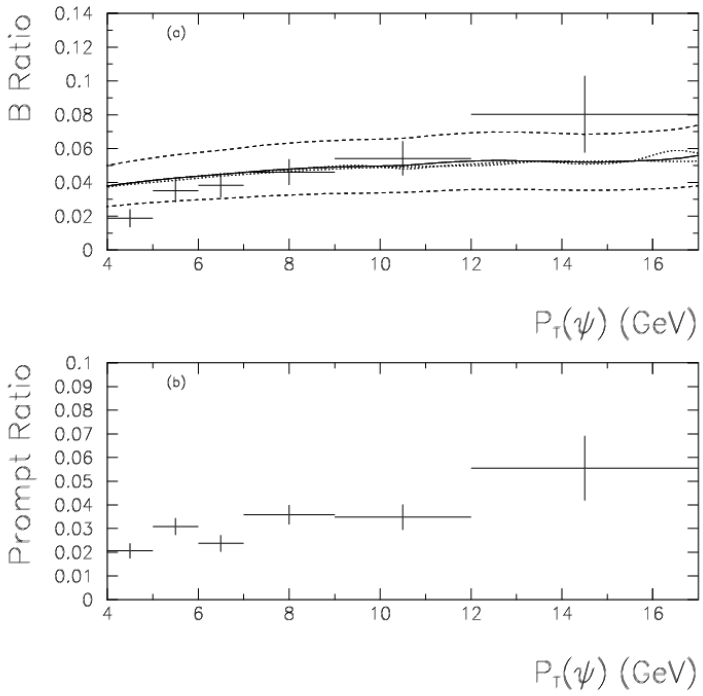

Figure 4.24: The ratio of $\psi(2S)$ to J/ψ measured in Run I.

Chapter 5

Conclusion

"We are what we repeatedly do."
— Aristotle 384 BC – 322 BC

This year will be one of the most exciting moments in particle physics. The Large Hadron Collider (LHC), the largest particle accelerator in the energy frontier is on its own way to begin its first collision at CERN, near Geneva, Switzerland. The Tevatron has played a leading role in the precise measurements, discoveries of missing pieces in the Standard Model, and the searches for new physics for decades.

5.1 Discussion and Future Prospects

Charmonium production and the polarization of the J/ψ and $\psi(2S)$ have provided important inputs and feedbacks in the field of quarkonium physics. It has been more than ten years since the CDF collaboration measured the prompt cross sections for the production of several charmonium states in $p\overline{p}$ collisions at a center-of-mass energy of 1.8 TeV[15, 38].

In this thesis, the $\psi(2S)$ production cross section and the polarization measured with about 1 fb^{-1} data have been reported. The result of the prompt $\psi(2S)$ polarization is summarized in Sec. 3.5. Even though the data include at least an order of magnitude higher statistics than the Run I measurement, the uncertainties on the polarization parameter α are still large. In theory, α should be zero at $p_T = 0$. It is noticeable

that the measured prompt $\psi(2S)$ polarization is also consistent with being zero in the p_T region of the measurement ($\chi^2 = 5.6$ for 3 degrees of freedom, for a probability 14%). This result is contrary to the polarization predictions of NRQCD factorization with color-octet matrix elements while the enhanced NNLO model predicts similar behavior, as is seen in the data.

The current measurement of the $\psi(2S)$ polarization is principally limited by statistics. The integrated luminosity of CDF at the time of this writing reached above 3 fb^{-1} and it is growing faster and faster. The higher statistics of the $\psi(2S)$ will improve the uncertainties in the polarization measurement and provide a useful guide to our understanding of charmonium production mechanism. The precise measurement of the $\psi(2S)$ polarization will also lead to an improvement in the cross section measurement.

The prompt production of $\psi(2S)$ mesons as summarized in Sec. 4.5 shows an increase both in the differential cross section for the over our p_T range and also in the integrated cross section relative to the Run I measurement. This increase can be expected from the higher parton density in $p\overline{p}$ collisions at a center-of-mass energy 1.96 TeV at Run II compared to that at 1.8 TeV in Run I. The data used in this thesis have at least an order of magnitude higher statistics than the Run I measurements and the p_T range of the differential cross section has been extended further into the perturbative region (out to 30 GeV/c).

NRQCD factorization approach introduces unknown non-perturbative parameters called Long-Distance Matrix Elements (LDME) which are universal functions in any collision and which therefore can be fixed from any single experiment or combination of experiments. The polarization measurement of $\psi(2S)$ in this thesis is contradictory to the prediction of the transverse polarization at large $p_T$from NRQCD. We note that a recent analysis of J/ψ production from fixed-target experiments [40] does not support the universality of the LDME. In the NRQCD factorization approach, the extraction of the various color-octet matrix elements relies on the differences in their p_T dependences. The smaller uncertainties and the extended p_T range of the measurement in this thesis will help to reduce the ambiguities in extracting the color-octet matrix elements.

The k_T-factorization approach is different from the collinear approaches as it uses effective BFKL vertices. Since the leading order contributions include fragmentation channels, this approach could be more suitable to the treatment of high energy collisions, in which fragmentation dominates, than the collinear approaches. In fact, the

k_T factorization predictions are in better agreement with some ep data from HERA than are the NRQCD predictions[4].

In the enhanced NNLO model, the authors calculated the prompt hadroproduction of J/ψ, $\psi(2S)$, and Υ states adding the additional contribution of an extra gluon exchange in NNLO amplitudes. The uncertainties of their calculation are rather large but with their choices of scales and the effective gluon mass, their cross section prediction describes the RHIC and Tevatron data well. In addition, their mechanism predicts a longitudinal polarization of J/ψ at large transverse momentum which agrees qualitatively with the recent Tevatron measurement. Nevertheless, at this stage this model cannot be used to predict the p_T slope of the cross section for either the J/ψ or the $\psi(2S)$ separately. It only gives their ratio. We hope that the agreement shown in this thesis leads to new developments in this picture, better to compare to data.

The Tevatron measurements have played the major role to probe charmonium production with the large available range of p_T but there are other experiments measure the charmonium production: ep collisions at HERA and e^+e^- annihilation at the B factories. The measurements of charmonium production in other experiments are also important since they can provide tests of the universality of the production matrix elements.

The measurement of quarkonium production and polarization at the LHC will provide tests of theoretical models at higher values of transverse momentum. The measurements at the highest available p_T are especially important since the factorization is robust there, while the measurement over the whole range of available p_T are interesting. It would be essential to construct parton-shower Monte Carlo codes based on NRQCD factorization to predict differential rates for quarkonium production at the LHC.

The NRQCD models have successfully matched the measured J/ψ and $\psi(2S)$ cross sections at the Tevatron while the polarization still remains as a smoking gun for the presence of the color-octet production mechanism. The puzzles still remain to be solved, but accompanying efforts and improvements in both theory and experiments will finally lead to a fundamental understanding of quarkonium physics.

Appendix A

Spin Density Matrix and Angular Distribution

Consider the production and decay of a resonance ψ in a two-body reaction,

$$a + b \to c + \psi, \quad \psi \to 1 + 2 \; .$$

The overall transition amplitude $\mathcal{M}_{fi}$ can be written as [41],

$$\mathcal{M}_{fi} \sim \sum_{\Lambda} \langle \vec{p} \lambda_1 \lambda_2 | \mathcal{M} | \psi \Lambda \rangle \langle \vec{p}_f \lambda_c \Lambda | T(w_0) | \vec{p}_i \lambda_a \lambda_b \rangle \; .$$

where $\vec{p}$ is the momentum of the particle 1 in the rest frame of the resonance ψ with the spherical angles given by $\Omega = (\theta, \phi)$, λ_1 is the spin of the particle 1, λ_2 is the spin of the particle 2, $\mathcal{M}$ is the transition amplitude of the ψ decay, Λ is the spin of the ψ, $\vec{p}_f$ is the center of mass momentum of the particle c, λ_c is the spin of the particle c, the operator T is defined by the invariant S matrix, $S = 1 + iT$, w_0 is the center of mass energy, $\vec{p}_i$ is the center of mass momentum of the particle a, λ_a is the spin of the particle a, and λ_b is the spin of the particle b.

Then the differential cross section in the ψ rest frame decay angle $\Omega = (\theta, \phi)$ can be expressed as,

$$\frac{d\sigma}{d\Omega} \sim \int d\Omega_0 \; dw K(w) \sum |\mathcal{M}_{fi}|^2 \; ,$$

where w is the mass of the resonance ψ and $K(w)$ is a factor that includes all the

quantities dependent on w, such as the phase space factor and the square of the Breit-Wigner function $D(w)$ of the ψ.

If we define the spin density matrix correspoding to the ψ as,

$$\rho^{\psi}_{\Lambda\Lambda'} \sim \int d\Omega_0 \sum \langle \vec{p}_f \lambda_c \Lambda | T(w_0) | \vec{p}_i \lambda_a \lambda_b \rangle \times \langle \vec{p}_f \lambda_c \Lambda | T(w_0) | \vec{p}_i \lambda_a \lambda_b \rangle^* \ ,$$

where the sum runs over λ_a, λ_b, and λ_c, we can write the differential cross section as,

$$\frac{d\sigma}{d\Omega} \sim \int \ dw K(w) \sum_{\Lambda\Lambda'\lambda_1\lambda_2} \langle \vec{p}\lambda_1\lambda_2 | \mathcal{M} | \psi\Lambda \rangle \rho^{\psi}_{\Lambda\Lambda'} \langle \psi\Lambda' | \mathcal{M}^{\dagger} | \vec{p}\lambda_1\lambda_2 \rangle$$

and the spin density matrix contains the information on the production polarization.

By definition, the spin density matrix is Hermitian and satisfies $\mathrm{Tr}(\rho) = 1$, and the parity conservation leads to a relation,

$$\rho^{\psi}_{\Lambda\Lambda'} = (-)^{\Lambda-\Lambda'} \rho^{\psi}_{-\Lambda-\Lambda'} \ .$$

The spin density matrix ρ of the $\psi(2\mathrm{S})$ in dimuon decay can be written as,

$$\rho = \begin{pmatrix} \rho_{11} & \rho_{10} & \rho_{1-1} \\ \rho_{01} & \rho_{00} & \rho_{0-1} \\ \rho_{-11} & \rho_{-10} & \rho_{-1-1} \end{pmatrix}$$

where ρ_{00} is the longitudinal polarization fraction and $(\rho_{11} + \rho_{-1-1})$ is the transverse polarization fraction.

In this thesis, the decay coordinate system $(\hat{x}, \hat{y}, \hat{z})$ is defined as: $\hat{z}$ lies along the momentum of $\psi(2\mathrm{S})$ in the lab frame, $\hat{y}$ is the production plane normal which is lying along the vector product of the proton momentum in the lab frame and the $\psi(2\mathrm{S})$ momentum, and thus $\hat{x} = \hat{y} \times \hat{z}$ in the right-handed coordinate system. Since $\hat{z}$ lies along the $\psi(2\mathrm{S})$ momentum in the lab frame, the directions of these unit vectors do not change under Lorentz boost between the lab frame and the $\psi(2\mathrm{S})$ rest frame.

The normalized angular distribution for $\psi(2\mathrm{S}) \to \mu^+\mu^-$ is,

$$I(\Omega^*) = \left(\frac{2J+1}{4\pi} \right) \sum_{mm'} \rho^J_{mm'} \sum_{\lambda} D^{J^*}_{m\lambda}(\phi^*, \theta^*, 0) D^J_{m'\lambda}(\phi^*, \theta^*, 0) g^J_{\lambda} \ , \qquad \text{(A.1)}$$

where $\Omega^*(\theta^*, \phi^*)$ describes the direction of the μ^+ in the $\psi(2S)$ rest frame with respect to the direction of the $\psi(2S)$ in the lab frame, $\rho^J_{mm'}$ is the spin density matrix for $\psi(2S)$ with spin J, $D^{J^*}_{m\lambda}(\phi^*, \theta^*, 0)$ is the rotation matrix, g^J_λ is the decay amplitude, and $\lambda = \lambda_{\mu^+} - \lambda_{\mu^-}$.

Using the fact that the spin density matrix is Hermitian and the parity conservation, the elements of ρ satisfies, $\rho_{-1-1} = \rho_{11}$, $\rho_{-11} = \rho_{1-1}$, $\rho_{-10} = -\rho_{10}$, $\rho_{0-1} = -\rho_{01}$. Therefore there are only four independent real parameters in ρ. A convenient set is ρ_{00}, ρ_{1-1}, $\mathrm{Re}(\rho_{10})$, $\mathrm{Im}(\rho_{10})$.

A further simplification can be done by assuming that the μ^+ is 100% right-handed and the μ^- is 100% left-handed based on the fact that the muons in the $\psi(2S)$ rest frame are relativistic. Then $\lambda = 1$ and there is only one decay amplitude g^1_1 ,and $g^1_1 = 1$ by the trace condition, $\sum_\lambda g^J_\lambda = 1$.

The definition of the rotation matrix can be given as,

$$\begin{aligned} D^j_{m'm}(\alpha, \beta, \gamma) &= \langle jm'|e^{-i\alpha J_z} e^{-i\beta J_y} e^{-i\gamma J_z}|\rangle \\ &= e^{-im'\alpha} d^j_{m'm} e^{-im\gamma} \end{aligned}$$

Using all the constraints and substituting the corresponding rotation matrix D using the relation between the D and the shperical harmonics, Eq. A.1 becomes,

$$\begin{aligned} I(\Omega^*) = \left(\frac{3}{4\pi}\right) [&\frac{1}{4}(1 + \cos^2\theta^*) + \frac{\rho_{00}}{4}(2\sin^2\theta^* - \cos^2\theta^* - 1) + \frac{\rho_{1-1}}{2}\sin^2\theta^* \cos 2\phi^* \\ &+ \frac{\mathrm{Re}(\rho_{10})}{\sqrt{2}} \sin 2\theta^* \cos\phi^* - \sqrt{2}\mathrm{Im}(\rho_{10}) \sin\theta^* \sin\phi^*] \ . \end{aligned} \quad \text{(A.2)}$$

The polarization measurement is done by integrating over ϕ^* in this analysis, and thus Eq. A.2 can be further simplified by integrating over ϕ^*,

$$I(\theta^*) = \frac{3}{2}\left[\frac{1}{4}(1 + \cos^2\theta^*) + \frac{\rho_{00}}{4}(1 - 3\cos^2\theta^*)\right] \ .$$

Defining the polarization parameter $\alpha = \frac{1-3\rho_{00}}{1+\rho_{00}}$, the angular distribution can be written as,

$$I(\theta^*) = \frac{3}{2(\alpha + 3)}\left(1 + \alpha\cos^2\theta^*\right) \ . \quad \text{(A.3)}$$

Appendix B

B.1 Polarization Fit Templates

The templates for the polarization fit is made from the Monte Carlo samples. A full transverse/longitudinal MC samples are reconstructed after following a sequence of detector simulation and the trigger efficiency correction. The MC templates used in the polarization analysis are listed below.

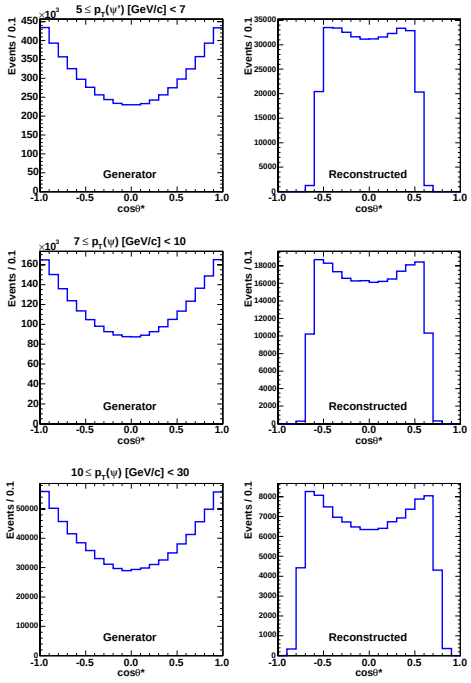

(a) Fully transverse templates

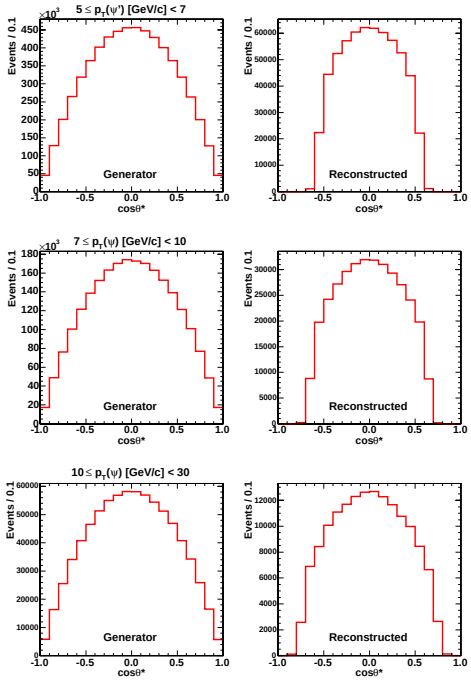

(b) Fully longitudinal templates

Figure B.1: The cosθ^* templates from Monte Carlo samples for $p_T(\mu) > 1.75$ GeV/c.

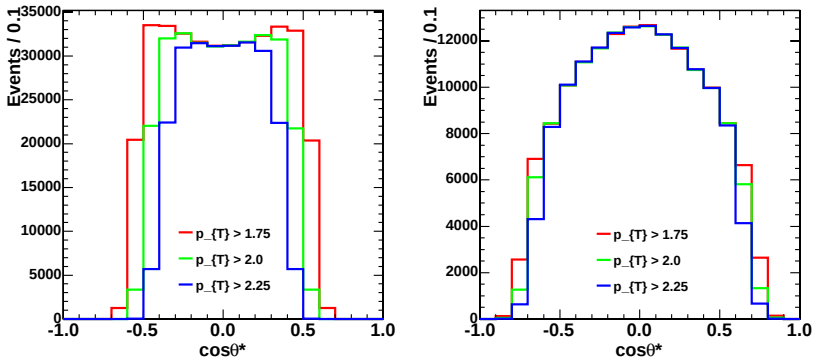

(a) $p_T(\psi(2S))$ 5-7 GeV/c

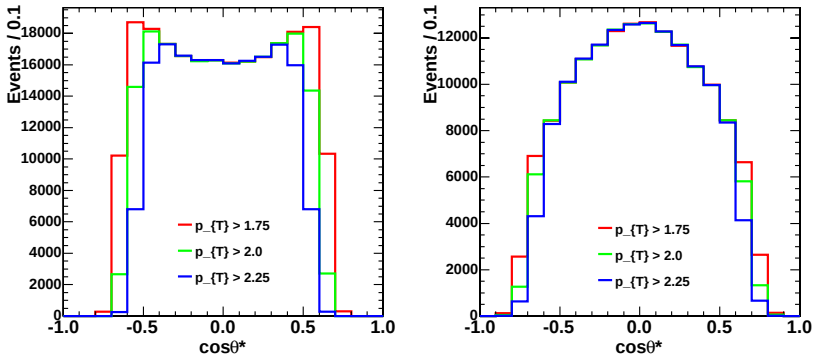

(b) $p_T(\psi(2S))$ 7-10 GeV/c

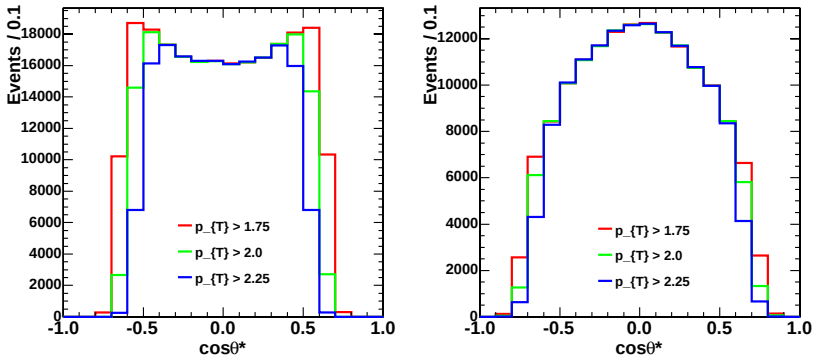

(c) $p_T(\psi(2S))$ 10-30 GeV/c

Figure B.2: The cosθ^* templates for different $p_T(\mu)$ cuts in each $\psi(2S)$ p_T bin. Left column is for T and right column is for L.

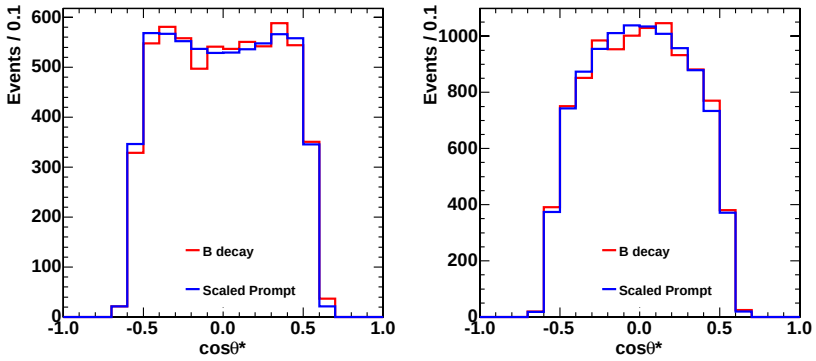

(a) $p_T(\psi(2S))$ 5-7 GeV/c

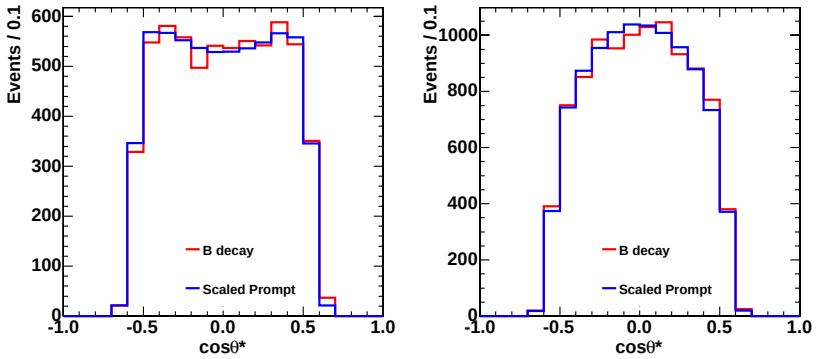

(b) $p_T(\psi(2S))$ 7-10 GeV/c

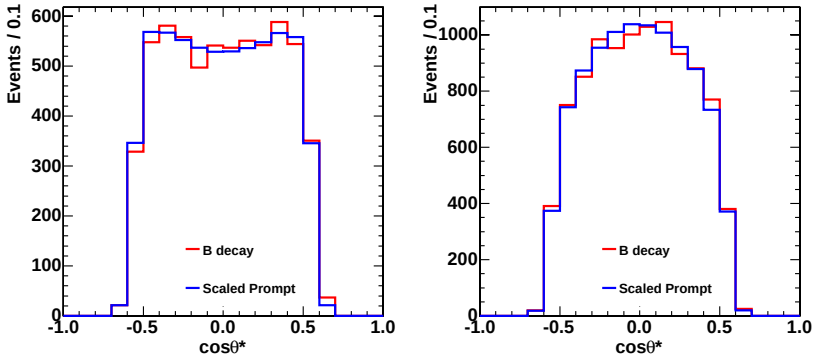

(c) $p_T(\psi(2S))$ 10-30 GeV/c

Figure B.3: The B decay cosθ^* templates with the scaled prompt templates in each $\psi(2S)$ p_T bin. Left column is for T and right column is for L.

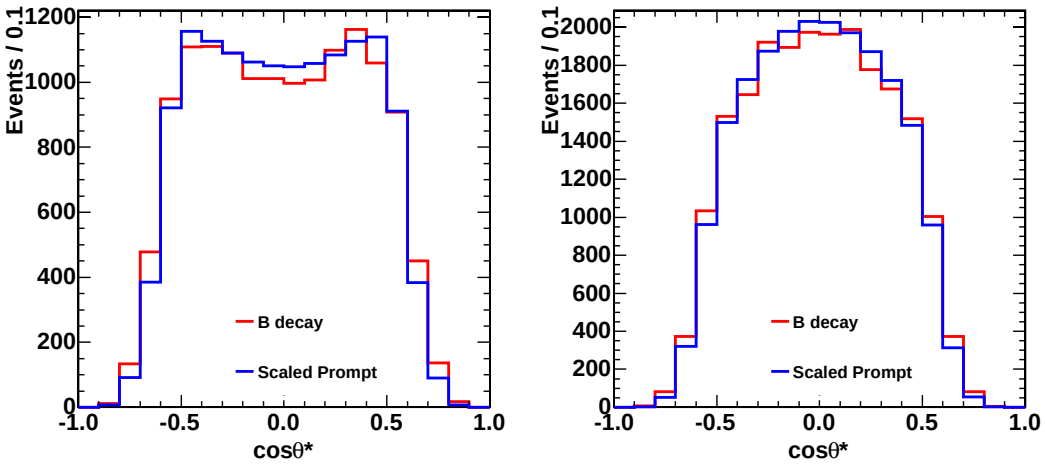

Figure B.4: The cosθ^* templates used for the B decay polarization fit with the scaled prompt templates.

B.2 Simulation tcl scripts

B.2.1 Prompt MC

```
#-----------------------------------------------------------------
# This is the tcl file that defines the tclfragment collection,
# as well as defining a variety of parameters for the
# mcrequest.
#
# generator: FakeEv
# decay table: EvtGen
# dimuon filter at particle level.
#
#-----------------------------------------------------------------
#
# Mosix = 1 turns off timer action
#
set Mosix             0
set outputPath   myPath
#
set dataset           $env(cdfSim_DATASET)
set run               $env(cdfSim_RUN)
set runSection        $env(cdfSim_RUNSECTION)
set repFreq           100
set nevents           $env(cdfSim_EVTS)
set evtOffset         $env(cdfSim_OFFSET)
creator set NSIM
#set cdfSim_REALISTIC_MC 1
set outputDir        .
set outputFile $outputDir/simulation.output

### Use official location to source tcl files for chosen release.
# Unless you are using a test release
if [ file exists $env(SRT_PRIVATE_CONTEXT)/SimulationMods/test ] {
 set TCL_LOCATION $env(SRT_PRIVATE_CONTEXT)/SimulationMods/test
} else {
```

```
 set TCL_LOCATION $env(SRT_PUBLIC_CONTEXT)/SimulationMods/test
}
#  ^--- above is not really used but makes the standard tcl happy.
#
#
#*****************************************************************
#       tcl fragments that are part of this collection:
#*****************************************************************
useRCP set false
#-------- setup the gen input manager ----------------
#         these are standard files,
#         you should not need to change these
#
# source mc_cdfSim_convert.tcl
#-------------------------------------------------------------
# provides a conversion of tcl variables from runMC to cdfSim
# so that cdfSim scripts can be used relatively untouched
#-------------------------------------------------------------
set cdfSim_REPORT_FREQUENCY 1000
set cdfSim_FIRST_EVENT      $evtOffset
set cdfSim_RUN_NUMBER       $run
set cdfSim_RUN_SECTION      $runSection
set cdfSim_OUTPUT_FILE      $outputFile
set cdfSim_RANDOM_SEED_OUTPUT ${dataset}_${runSection}_CdfRnStat.dat
set cdfSim_RANDOM_SEED_INPUT $env(RANDOM_SEED_INPUT)
#===== End of ../mcProduction/Bgroup/tcl/mc_cdfSim_convert.tcl =====

#-------- setup the generator and decayer -----------------
#
#     The decay table must be in the BMC-<release>/dbt  directory
#    you can set here the particle definition file e.g.
#    set env(EVTGEN_PDT_TABLE)  $env(EVTGEN_DECAY_DIR)/pdt_nomix.table
# source setup_fakeev.tcl
#########################################################################
# enable generator ( no generators are enabled by default )
module enable FAKE_EVENT
```

```
talk FAKE_EVENT
    use PT
    use RAPIDITY
    use PHI
# SET PARAMETER_NAME MEAN SIGMA PMIN PMAX POWER MODE(1=gauss,2=flat)
    generate RAPIDITY 0. 0.   0.    0.8   0.  2
    generate PHI      0. 0.   0.    360.  0.  2
# generate psi(2S)
  generate CDFCODE  30443
  generate NPARTICLES 1
#############################################################################
  PtHistMenu
    usePtHist set true
    lowPt  set   5.
    highPt set  30.
    nbinPt set 250
    source $env(EVTGEN_DECAY_DIR)/psi_pt.dat
  exit
#############################################################################
  show
exit
#############################################################################
#===== End of ../mcProduction/Bgroup/tcl/setup_fakeev.tcl =====

  set userDecayFile psi2Smm.DEC
# source mc_evtgen534.tcl
#
#  Evt Gen setup for CHARM
#
mod enable EvtGen
mod disable TauolaModule
mod disable QQModule
#
module talk EvtGen
  UseUserDecayFile set t
  UserDecayFile set  $env(EVTGEN_DECAY_DIR)/$userDecayFile
```

```
  DecayPromptCharm set true
show
exit

#========== End of ../mcProduction/Bgroup/tcl/mc_evtgen534.tcl =============
...
```

B.2.2 B-decay MC

```
#-----------------------------------------------------------------
# This is the tcl file that defines the tclfragment collection,
# as well as defining a variety of parameters for the
# mcrequest.
#
# 508 BGenerator inclusive B
# External spectrum from note cdf6285 (inclusive J/Psi)
# decay table EvtGen B to psi X to mu mu X
# dimuon filter at particle level.
#
#-----------------------------------------------------------------
#
# Mosix = 1 turns off timer action
#
set Mosix             0
set outputPath   myPath
#
set dataset           $env(cdfSim_DATASET)
set run               $env(cdfSim_RUN)
set runSection        $env(cdfSim_RUNSECTION)
set repFreq           100
set nevents           $env(cdfSim_EVTS)
set evtOffset         $env(cdfSim_OFFSET)
creator set NSIM
#set cdfSim_REALISTIC_MC 1
set outputDir        .
```

```
set outputFile $outputDir/simulation.output

### Use official location to source tcl files for chosen release.
# Unless you are using a test release
if [ file exists $env(SRT_PRIVATE_CONTEXT)/SimulationMods/test ] {
 set TCL_LOCATION $env(SRT_PRIVATE_CONTEXT)/SimulationMods/test
} else {
 set TCL_LOCATION $env(SRT_PUBLIC_CONTEXT)/SimulationMods/test
}
#  ^--- above is not really used but makes the standard tcl happy.
#
#
#*****************************************************************
#       tcl fragments that are part of this collection:
#*****************************************************************
useRCP set false
#-------- setup the gen input manager ----------------
#         these are standard files,
#         you should not need to change these
#
# source mc_cdfSim_convert.tcl
#-------------------------------------------------------------
# provides a conversion of tcl variables from runMC to cdfSim
# so that cdfSim scripts can be used relatively untouched
#-------------------------------------------------------------
set cdfSim_REPORT_FREQUENCY 100
set cdfSim_FIRST_EVENT      $evtOffset
set cdfSim_RUN_NUMBER       $run
set cdfSim_RUN_SECTION      $runSection
set cdfSim_OUTPUT_FILE      $outputFile
set cdfSim_RANDOM_SEED_OUTPUT ${dataset}_${runSection}_CdfRnStat.dat
set cdfSim_RANDOM_SEED_INPUT $env(RANDOM_SEED_INPUT)
#===== End of ../mcProduction/Bgroup/tcl/mc_cdfSim_convert.tcl =====

#      User-dependant part:
#      you can change pt and y cuts
```

```
# ------- setup B+/B- pt > 5 ,|y| < 1.3 ---
#    -bmeson=1 B+
#    -bmeson=2 B0
#    -bmeson=3 Bs
#    -bmeson=4 Bc+
#    -bmeson=5 AntiLambdaB
#    -bmeson=6 User Defined
   set BMeson 1
   set BGen_PtMin1 5.0
   set BGen_PtMin2 0
   set BGen_EtaMin -1.3
   set BGen_EtaMax  1.3
   set spectrum     B_spectrum.hbook
   set hist         1
# source mc_bgen_ext_spectrum.tcl
 set env(BOTTOM_LIBRARY) $env(PROJECT_DIR)/generatorMods/bgen
# first disable everything in HardScatGenSequence:
mod disable Pythia
mod disable Isajet
mod disable herwig
mod disable Bgenerator
mod disable FAKE_EVENT
mod disable WGRAD
mod disable Wbbgen
mod disable VecbosModule
mod disable VecunwModule
mod disable Vecher
# enable this MC generator
module enable Bgenerator
module talk   Bgenerator
  Bgenerator
  VERBOSE set 0
  PT-MIN-b1 set $BGen_PtMin1
  PT-MIN-b2 set $BGen_PtMin2
  RAPMIN-b1 set  $BGen_EtaMin
  RAPMAX-b1 set  $BGen_EtaMax
```

```
# external spectrum and hist specifications
  NDE -gentype=10 -file=$env(EVTGEN_DECAY_DIR)/$spectrum -ihist=$hist -bxsec=0
# Fragmentation fraction from CDF 7911
  BMESON -gencode=3 -mixu=35.6 -mixd=33.8 -mixs=11.1 -mixc=0. -mixl=19.5
#
#    -bmeson=1 B+
#    -bmeson=2 B0
#    -bmeson=3 Bs
#    -bmeson=4 Bc+
#    -bmeson=5 AntiLambdaB
#    -bmeson=6 User Defined
     BMESON -gencode=2 -bmeson=$BMeson
# fragmentation is turned off in case of external spectrum
     FRAGMENT set 0
   show
 exit
exit

#===== End of ../mcProduction/Bgroup/tcl/mc_bgen_ext_spectrum.tcl =====

#-------- setup the decayer ----------------
#
#     The decay table must be in the BMC-<release>/dbt  directory
#    you can set here the particle definition file e.g.
#    set env(EVTGEN_PDT_TABLE)  $env(EVTGEN_DECAY_DIR)/pdt_nomix.table
     set userDecayFile BtoPsiUX.DEC
# source mc_EvtGen_BMeson.tcl
#
#  Evt Gen setup for BMeson decay
#
module enable EvtGen
mod disable TauolaModule
mod disable QQModule
#
module talk EvtGen
  UseUserDecayFile set t
```

```
  UserDecayFile set  $env(EVTGEN_DECAY_DIR)/$userDecayFile
  DecayBMeson set true
  DecayPromptCharm set false
  DecayBBaryon set false
exit

#===== End of ../mcProduction/Bgroup/tcl/mc_EvtGen_BMeson.tcl =====
...
```

B.3 The modified decay table

```
#decay ratio has been modified to
Decay anti-B0
#       B -> cc= s
0.103   psi(2S)  K_S0              SVS_CP beta  dm -1 1.0 0.0 1.0 0.0;
0.103   psi(2S)  K_L0              SVS_CP beta  dm  1 1.0 0.0 1.0 0.0;
0.052   psi(2S)  K*S               SVV_CP beta  dm 1 Aplus phAplus Azero
                                                    phAzero Aminus phAminus;
0.052   psi(2S)  K*L               SVV_CP beta  dm  -1 Aplus phAplus Azero
                                                    phAzero Aminus phAminus;
0.207   psi(2S)  anti-K*0T         SVV_HELAMP PKHplus PKphHplus PKHzero
                                               PKphHzero PKHminus PKphHminus;

0.138   psi(2S)  K-  pi+                PHSP;
0.069   psi(2S)  anti-K0   pi0          PHSP;
0.069   psi(2S)  anti-K0   pi+  pi-     PHSP;
0.034   psi(2S)  anti-K0   pi0  pi0     PHSP;
0.034   psi(2S)  K-  pi+  pi0           PHSP;
0.138   psi(2S)  anti-K_10             PHSP;
Enddecay
#
Decay B0
#       B -> cc= s
0.103     psi(2S)  K_S0              SVS_CP beta  dm -1 1.0 0.0 1.0 0.0;
0.103     psi(2S)  K_L0              SVS_CP beta  dm  1 1.0 0.0 1.0 0.0;
```

```
0.052     psi(2S)  K*S              SVV_CP beta  dm 1 Aplus phAplus Azero
                                                 phAzero Aminus phAminus;
0.052     psi(2S)  K*L              SVV_CP beta  dm  -1 Aplus phAplus Azero
                                              phAzero Aminus phAminus;
0.207     psi(2S)  K*0T             SVV_HELAMP PKHplus PKphHplus PKHzero
                                              PKphHzero PKHminus PKphHminus;

0.138     psi(2S)  K+  pi-          PHSP;
0.069     psi(2S)  K0  pi0          PHSP;
0.069     psi(2S)  K0  pi-  pi+     PHSP;
0.034     psi(2S)  K0  pi0  pi0     PHSP;
0.034     psi(2S)  K+  pi-  pi0     PHSP;
0.138     psi(2S)  K_10             PHSP;
Enddecay
#
Decay B-
#   B -> cc= s          sum = 1.92%
0.207    psi(2S) K-                       SVS;
0.310    psi(2S) K*-                      SVV_HELAMP PKHplus PKphHplus
                                        PKHzero PKphHzero PKHminus PKphHminus;
0.138    psi(2S) anti-K0   pi-                  PHSP;
0.069    psi(2S) K-  pi0                  PHSP;
0.069    psi(2S) K-  pi+  pi-             PHSP;
0.034    psi(2S) K-  pi0  pi0             PHSP;
0.034    psi(2S) anti-K0   pi-  pi0             PHSP;
0.138    psi(2S)  K_1-             PHSP;
Enddecay
#
Decay B+
#   B -> cc= s          sum = 1.92%
0.207    psi(2S) K+                       SVS;
0.310    psi(2S) K*+                      SVV_HELAMP PKHplus PKphHplus
                                        PKHzero PKphHzero PKHminus PKphHminus;
0.138    psi(2S) K0  pi+                  PHSP;
0.069    psi(2S) K+  pi0                  PHSP;
0.069    psi(2S) K+  pi-  pi+             PHSP;
```

```
0.034    psi(2S) K+  pi0  pi0              PHSP;
0.034    psi(2S) K0  pi+  pi0              PHSP;
0.138    psi(2S)  K_1+                     PHSP;
Enddecay
#
Decay anti-B_s0
# fkw 4/28/00 Strategy for charmonium modes:
# Take Bd BR's, replace spectator,
# assume etaprime = 2/3 ss
# and eta = 1/3 ss
#
# Note: Just for kicks I gave the c\bar c decays a small piece that is
#       self tagging. See if you can find it. This is already in
#       the B0 decays in cleo's version of decay.dec .
#
#                              B --> (c c=)  (s s=)
# 2.65%
# should be: psi = 0.80%  CLNS 94/1315 but isn't quite right.
#
0.137    psi(2S) eta'              SVS;
0.069    psi(2S) eta               SVS;
0.353    psi(2S) phi               SVV_HELAMP  1.0 0.0 1.0 0.0 1.0 0.0;
0.088    psi(2S) K-       K+       PHSP;
0.088    psi(2S) anti-K0  K0       PHSP;
0.088    psi(2S) anti-K0  K+   pi- PHSP;
0.088    psi(2S) anti-K0  K0   pi0 PHSP;
0.088    psi(2S) K-       K+   pi0 PHSP;
Enddecay
# B_s decays.
# ------------------------------------------------------
# whb&fkw 3/28/01 Taken from fkw's QQ tables.
#                 most dubious part are the B to baryons.
# fkw 4/28/00 made the Bs parallel to the Bd as best as I could
# ------------------------------------------------------
Decay B_s0
0.137    psi(2S)     eta'                          SVS;
```

```
0.069    psi(2S)     eta                                SVS;
0.353    psi(2S)     phi              SVV_HELAMP  1.0 0.0 1.0 0.0 1.0 0.0;
0.088    psi(2S)     K-          K+                     PHSP;
0.088    psi(2S)     anti-K0     K0                     PHSP;
0.088    psi(2S)     K0          K-         pi+         PHSP;
0.088    psi(2S)     anti-K0     K0         pi0         PHSP;
0.088    psi(2S)     K-          K+         pi0         PHSP;
Enddecay
#
Decay psi(2S)
#VLLPOL alpha ; alpha =  1 Fully transverse
#                     =  0 Unpolarized
#                     = -1 Fully longitudinal
#1.0000    mu+  mu-                      VLLPOL  1;
1.0000    mu+  mu-                      VLLPOL  0;
#1.0000    mu+  mu-                      VLLPOL -1;
Enddecay
#
End
```

Appendix C

Fit Projections

The dashed lines in the residual plots indicate $\pm 2\ \sigma$ region of the signal (prompt component) in mass (proper decay length) projection. In interpreting the ct residual plots, recall that only the integral yield in the signal region marked by the dashed lines affects the cross section result. If the sum of the residuals in the signal region is nearly zero, then significant excursions in individual bins have no impact on the physics.

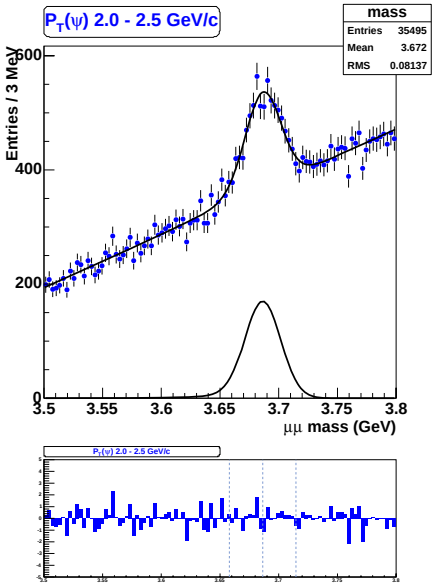

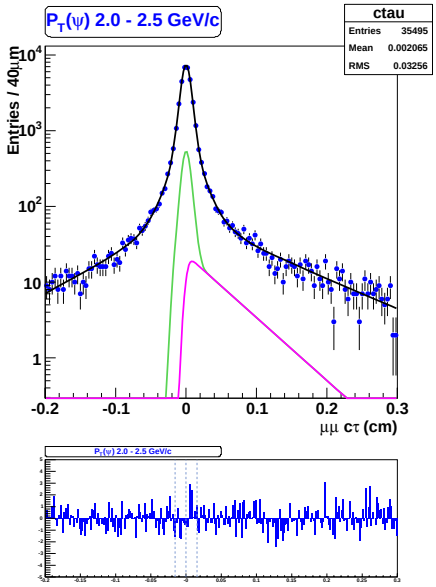

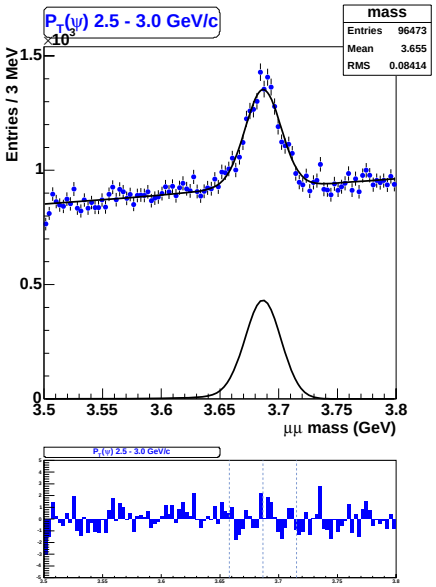
$P_T(\psi)$ 2.5 - 3.0 GeV/c
mass
Entries 96473
Mean 3.655
RMS 0.08414
Entries / 3 MeV
μμ mass (GeV)

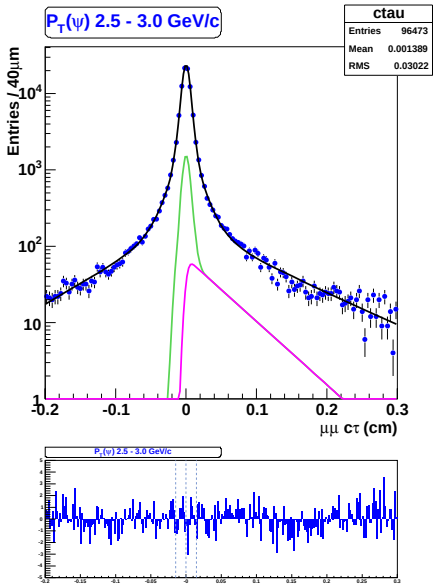
$P_T(\psi)$ 2.5 - 3.0 GeV/c
ctau
Entries 96473
Mean 0.001389
RMS 0.03022
Entries / 40μm
μμ cτ (cm)

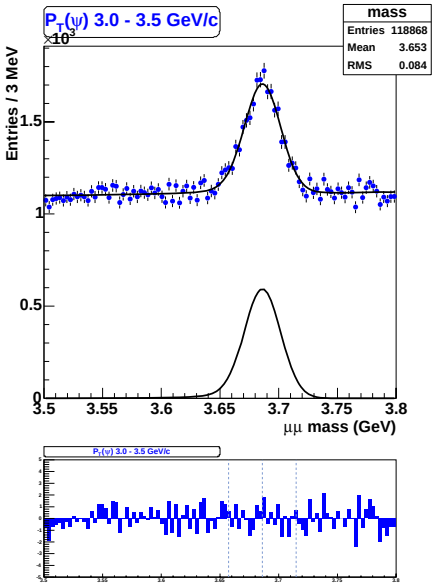
$P_T(\psi)$ 3.0 - 3.5 GeV/c
mass
Entries 118868
Mean 3.653
RMS 0.084
Entries / 3 MeV
μμ mass (GeV)

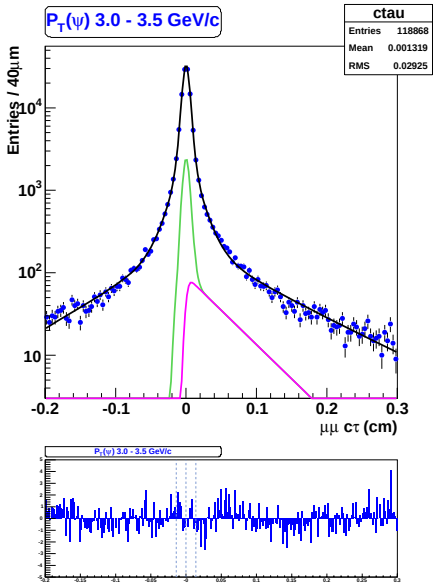
$P_T(\psi)$ 3.0 - 3.5 GeV/c
ctau
Entries 118868
Mean 0.001319
RMS 0.02925
Entries / 40μm
μμ cτ (cm)

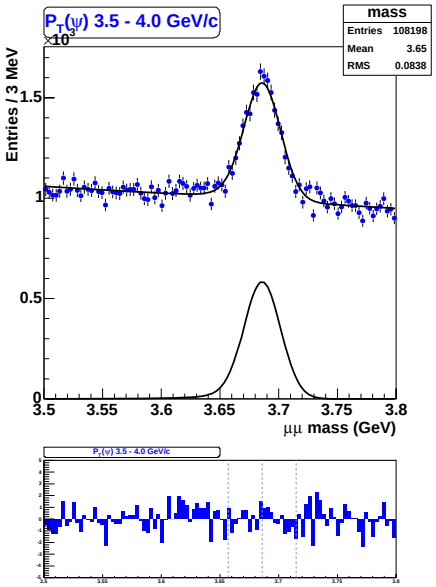
$P_T(\psi)$ 3.5 - 4.0 GeV/c
mass
Entries 108198
Mean 3.65
RMS 0.0838
Entries / 3 MeV
μμ mass (GeV)

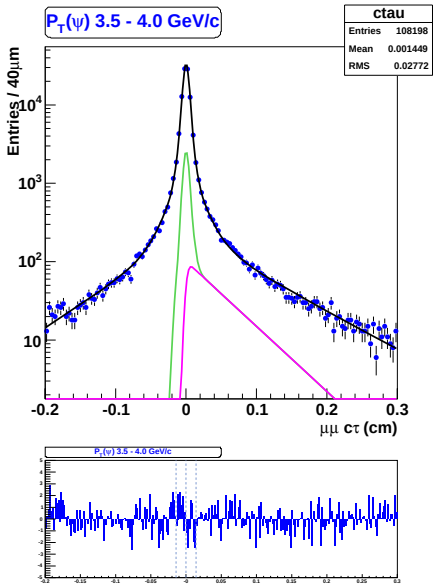
$P_T(\psi)$ 3.5 - 4.0 GeV/c
ctau
Entries 108198
Mean 0.001449
RMS 0.02772
Entries / 40μm
μμ cτ (cm)

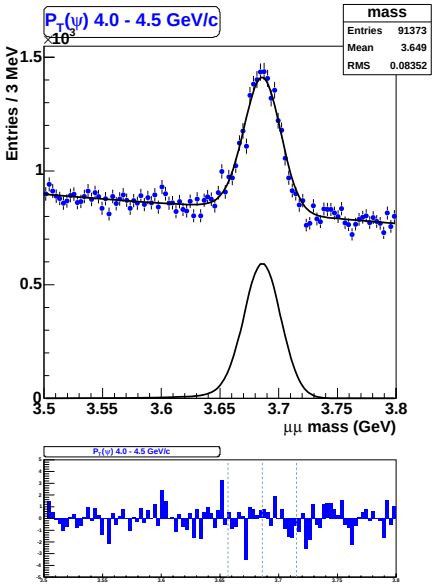
$P_T(\psi)$ 4.0 - 4.5 GeV/c
mass
Entries 91373
Mean 3.649
RMS 0.08352
Entries / 3 MeV
μμ mass (GeV)

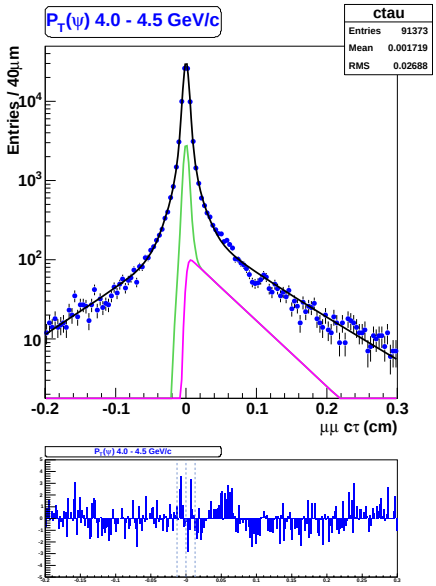
$P_T(\psi)$ 4.0 - 4.5 GeV/c
ctau
Entries 91373
Mean 0.001719
RMS 0.02688
Entries / 40μm
μμ cτ (cm)

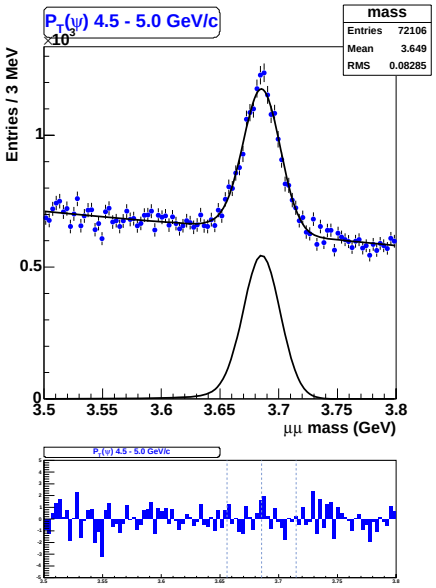
$P_T(\psi)$ 4.5 - 5.0 GeV/c
mass
Entries 72106
Mean 3.649
RMS 0.08285
Entries / 3 MeV
μμ mass (GeV)

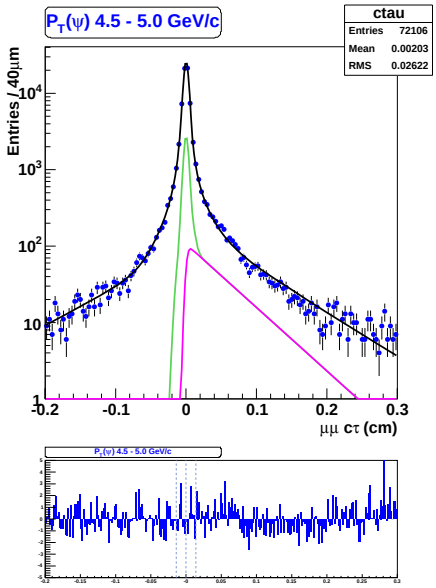
$P_T(\psi)$ 4.5 - 5.0 GeV/c
ctau
Entries 72106
Mean 0.00203
RMS 0.02622
Entries / 40μm
μμ cτ (cm)

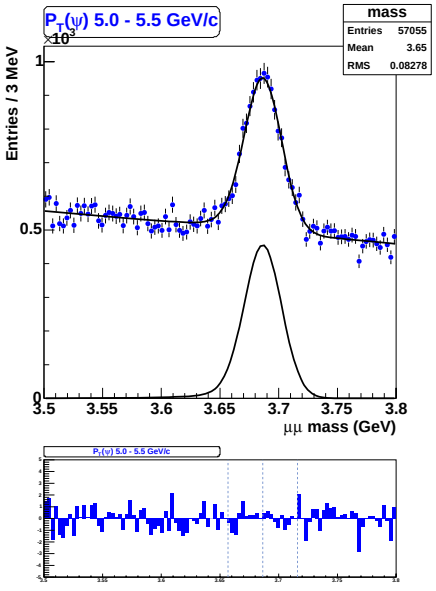
$P_T(\psi)$ 5.0 - 5.5 GeV/c
mass
Entries 57055
Mean 3.65
RMS 0.08278
Entries / 3 MeV
μμ mass (GeV)

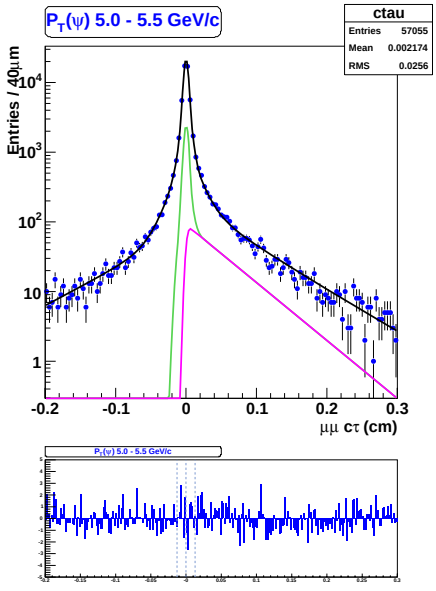
$P_T(\psi)$ 5.0 - 5.5 GeV/c
ctau
Entries 57055
Mean 0.002174
RMS 0.0256
Entries / 40μm
μμ cτ (cm)

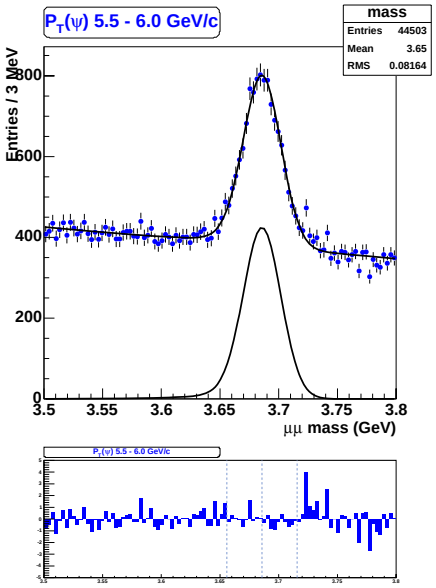
$P_T(\psi)$ 5.5 - 6.0 GeV/c
mass
Entries 44503
Mean 3.65
RMS 0.08164
Entries / 3 MeV
μμ mass (GeV)

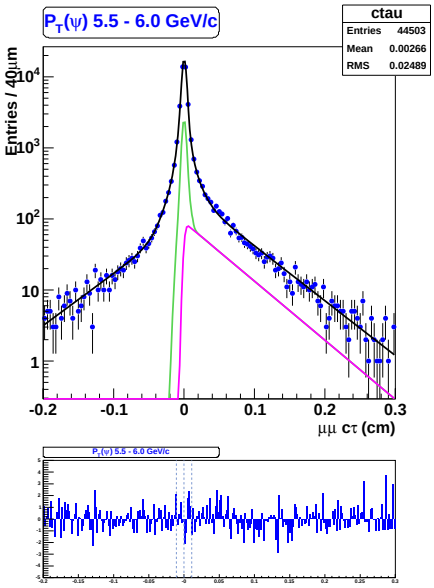
$P_T(\psi)$ 5.5 - 6.0 GeV/c
ctau
Entries 44503
Mean 0.00266
RMS 0.02489
Entries / 40 μm
μμ cτ (cm)

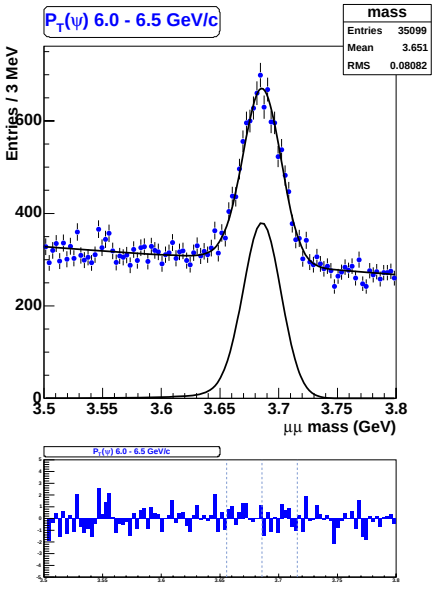
$P_T(\psi)$ 6.0 - 6.5 GeV/c
mass
Entries 35099
Mean 3.651
RMS 0.08082
Entries / 3 MeV
μμ mass (GeV)

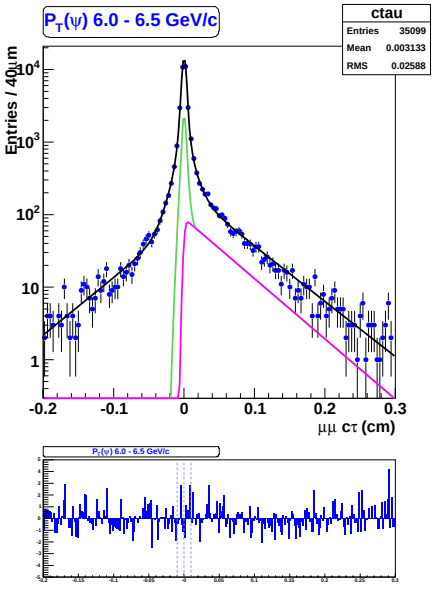
$P_T(\psi)$ 6.0 - 6.5 GeV/c
ctau
Entries 35099
Mean 0.003133
RMS 0.02588
Entries / 40 μm
μμ cτ (cm)

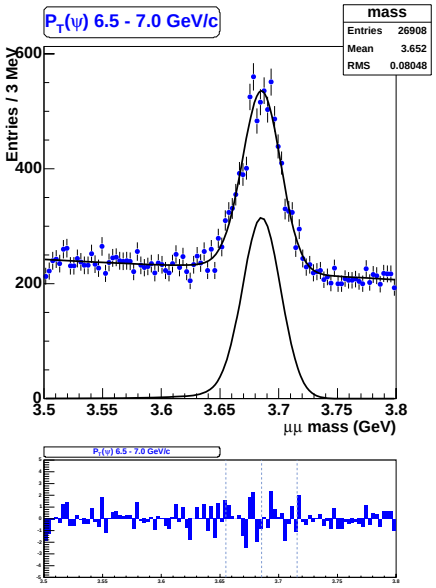
$P_T(\psi)$ 6.5 - 7.0 GeV/c
mass
Entries 26908
Mean 3.652
RMS 0.08048
Entries / 3 MeV
600
400
200
0
3.5
3.55
3.6
3.65
3.7
3.75
3.8
μμ mass (GeV)

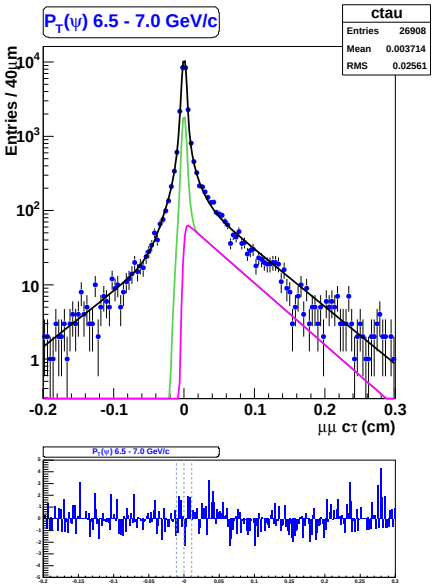
$P_T(\psi)$ 6.5 - 7.0 GeV/c
ctau
Entries 26908
Mean 0.003714
RMS 0.02561
Entries / 40 μm
10^4
10^3
10^2
10
1
-0.2
-0.1
0
0.1
0.2
0.3
μμ cτ (cm)

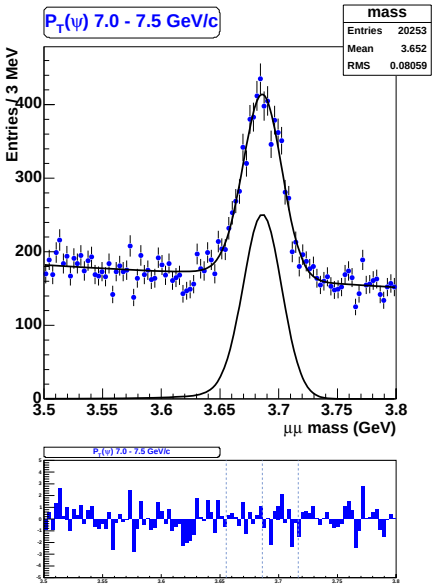
$P_T(\psi)$ 7.0 - 7.5 GeV/c
mass
Entries 20253
Mean 3.652
RMS 0.08059
Entries / 3 MeV
μμ mass (GeV)

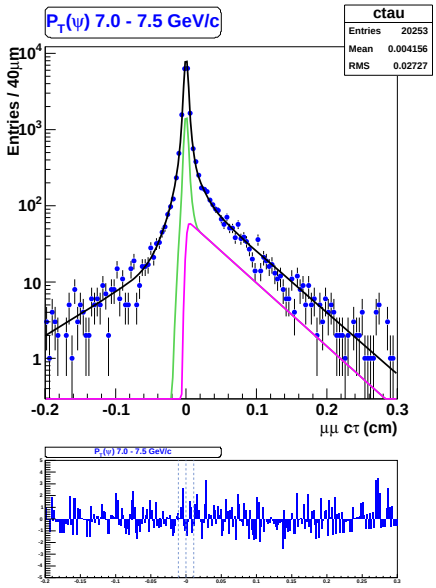
$P_T(\psi)$ 7.0 - 7.5 GeV/c
ctau
Entries 20253
Mean 0.004156
RMS 0.02727
Entries / 40μm
μμ cτ (cm)

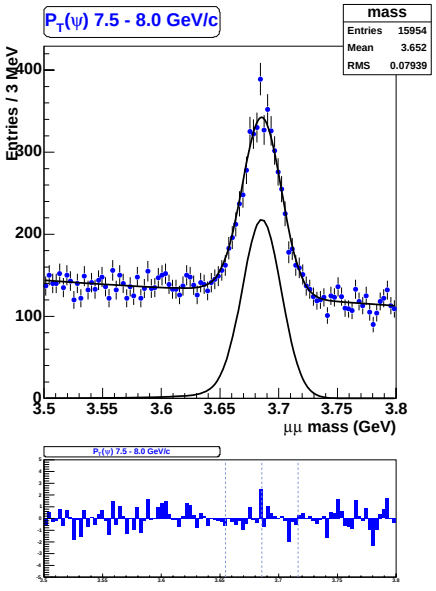
$P_T(\psi)$ 7.5 - 8.0 GeV/c
mass
Entries 15954
Mean 3.652
RMS 0.07939
Entries / 3 MeV
μμ mass (GeV)

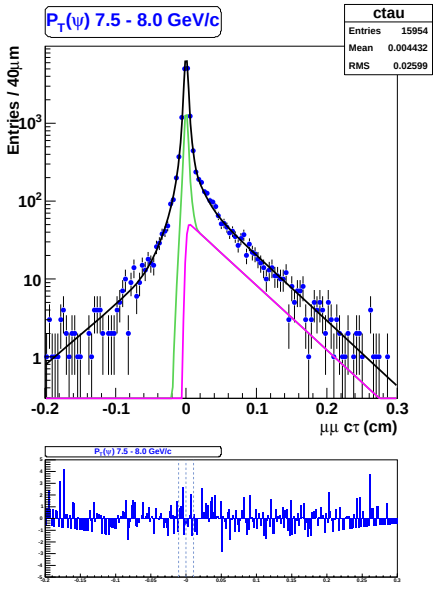
$P_T(\psi)$ 7.5 - 8.0 GeV/c
ctau
Entries 15954
Mean 0.004432
RMS 0.02599
Entries / 40μm
μμ cτ (cm)

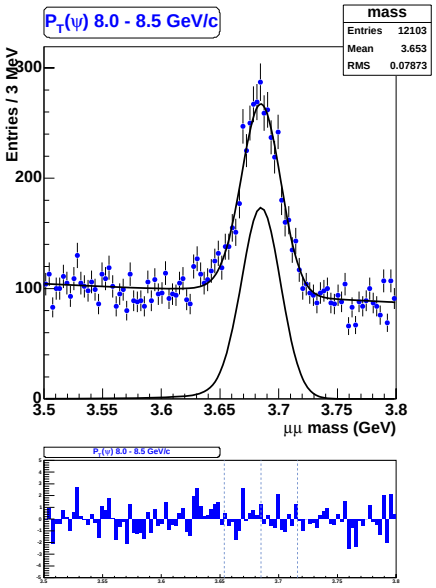
$P_T(\psi)$ 8.0 - 8.5 GeV/c
mass
Entries 12103
Mean 3.653
RMS 0.07873
Entries / 3 MeV
μμ mass (GeV)

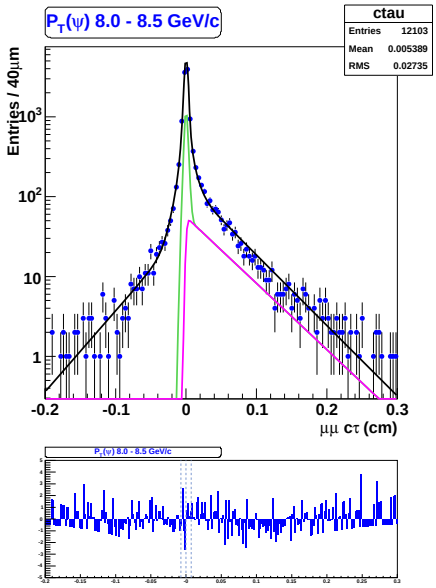
$P_T(\psi)$ 8.0 - 8.5 GeV/c
ctau
Entries 12103
Mean 0.005389
RMS 0.02735
Entries / 40μm
μμ cτ (cm)

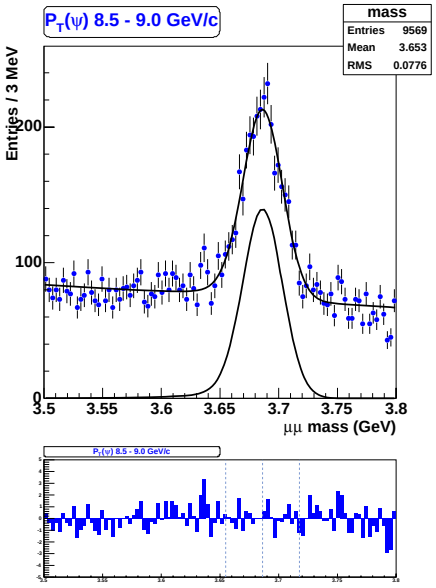
$P_T(\psi)$ 8.5 - 9.0 GeV/c
mass
Entries 9569
Mean 3.653
RMS 0.0776
Entries / 3 MeV
μμ mass (GeV)

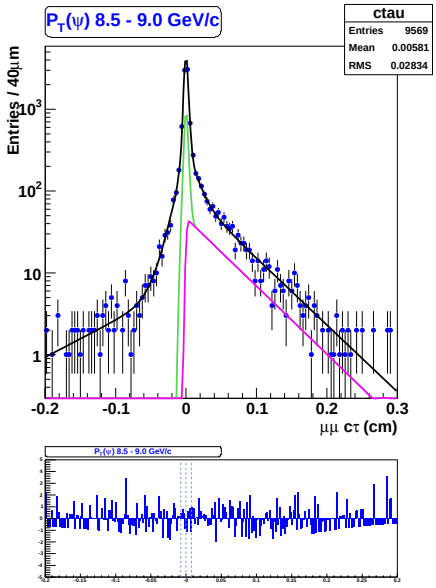
$P_T(\psi)$ 8.5 - 9.0 GeV/c
ctau
Entries 9569
Mean 0.00581
RMS 0.02834
Entries / 40μm
μμ cτ (cm)

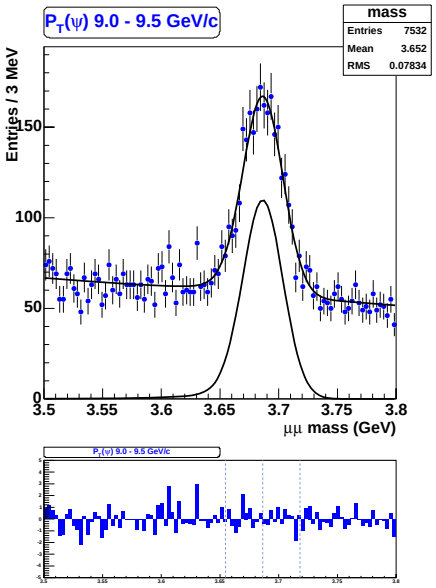
$P_T(\psi)$ 9.0 - 9.5 GeV/c
mass
Entries 7532
Mean 3.652
RMS 0.07834
Entries / 3 MeV
μμ mass (GeV)

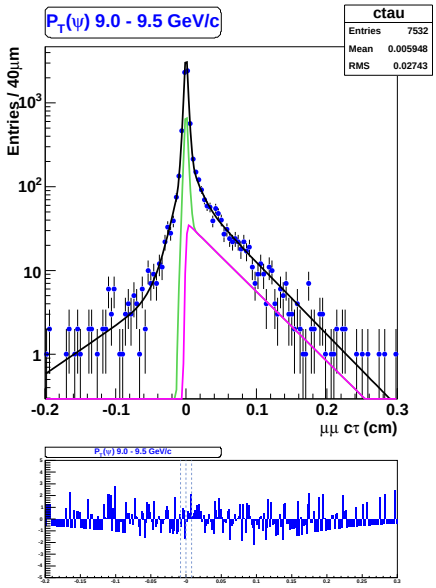
$P_T(\psi)$ 9.0 - 9.5 GeV/c
ctau
Entries 7532
Mean 0.005948
RMS 0.02743
Entries / 40μm
μμ cτ (cm)

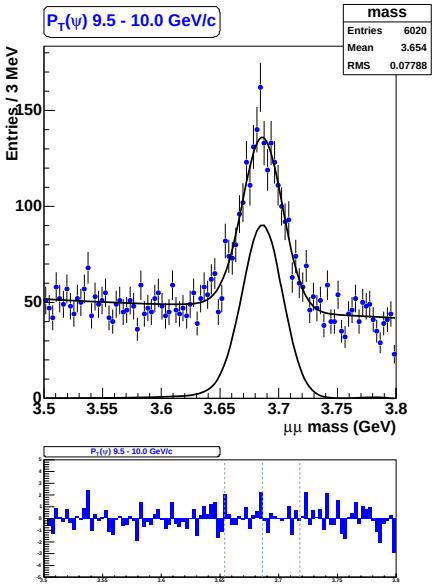
$P_T(\psi)$ 9.5 - 10.0 GeV/c
mass
Entries 6020
Mean 3.654
RMS 0.07788
Entries / 3 MeV
μμ mass (GeV)

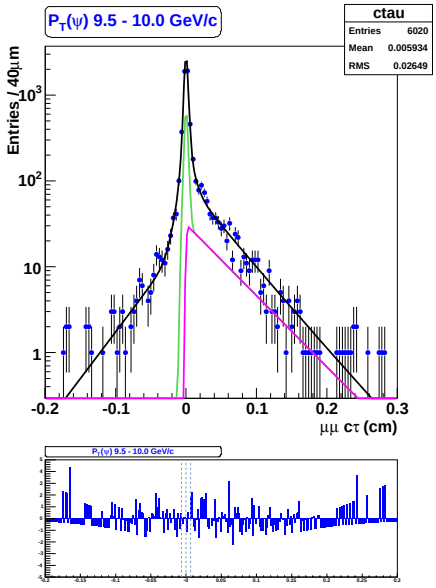
$P_T(\psi)$ 9.5 - 10.0 GeV/c
ctau
Entries 6020
Mean 0.005934
RMS 0.02649
Entries / 40μm
μμ cτ (cm)

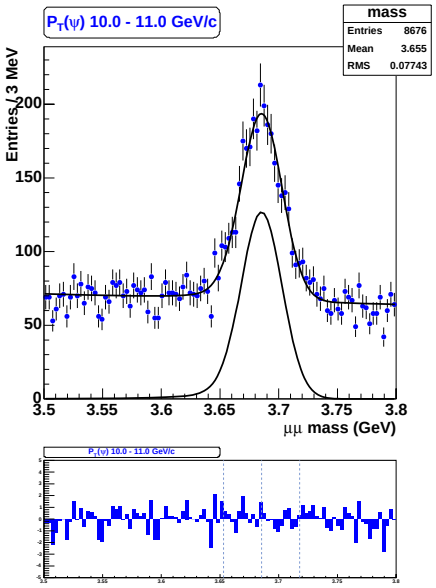
$P_T(\psi)$ 10.0 - 11.0 GeV/c
mass
Entries 8676
Mean 3.655
RMS 0.07743
Entries / 3 MeV
μμ mass (GeV)

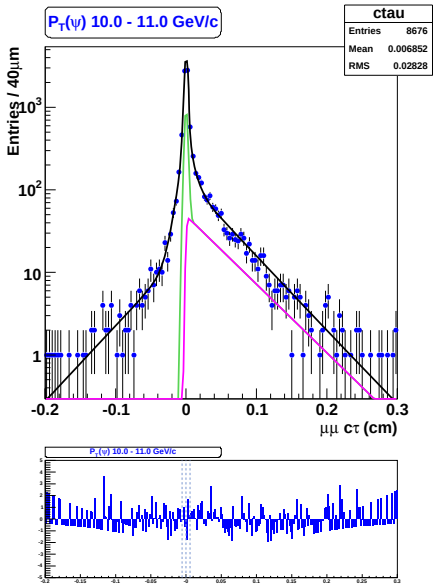
$P_T(\psi)$ 10.0 - 11.0 GeV/c
ctau
Entries 8676
Mean 0.006852
RMS 0.02828
Entries / 40μm
μμ cτ (cm)

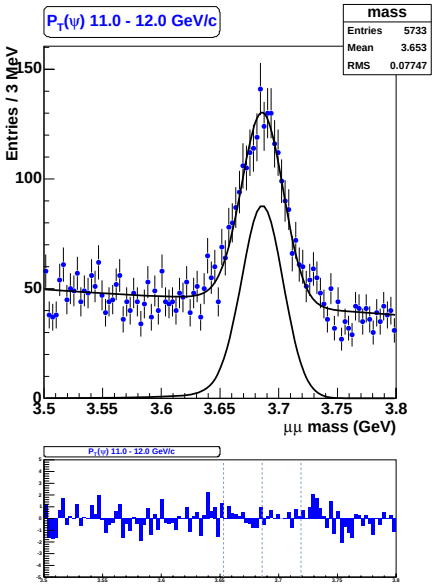
$P_T(\psi)$ 11.0 - 12.0 GeV/c
mass
Entries 5733
Mean 3.653
RMS 0.07747
Entries / 3 MeV
μμ mass (GeV)

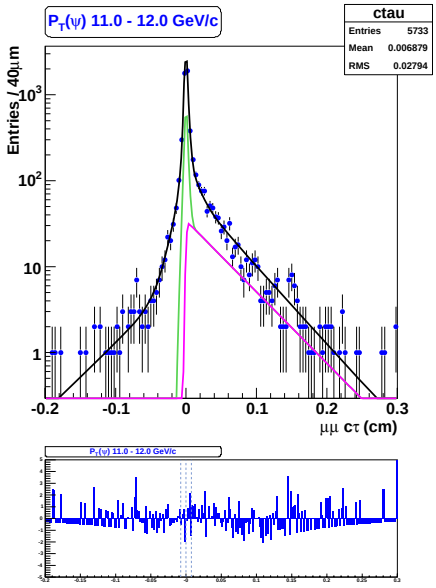
$P_T(\psi)$ 11.0 - 12.0 GeV/c
ctau
Entries 5733
Mean 0.006879
RMS 0.02794
Entries / 40μm
μμ cτ (cm)

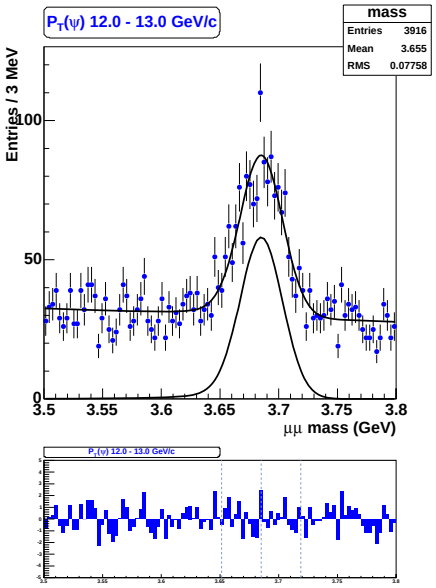
$P_T(\psi)$ 12.0 - 13.0 GeV/c
mass
Entries 3916
Mean 3.655
RMS 0.07758
Entries / 3 MeV
μμ mass (GeV)

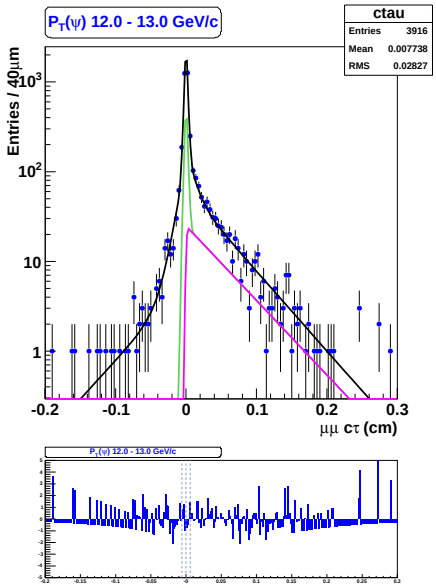
$P_T(\psi)$ 12.0 - 13.0 GeV/c
ctau
Entries 3916
Mean 0.007738
RMS 0.02827
Entries / 40 μm
μμ cτ (cm)

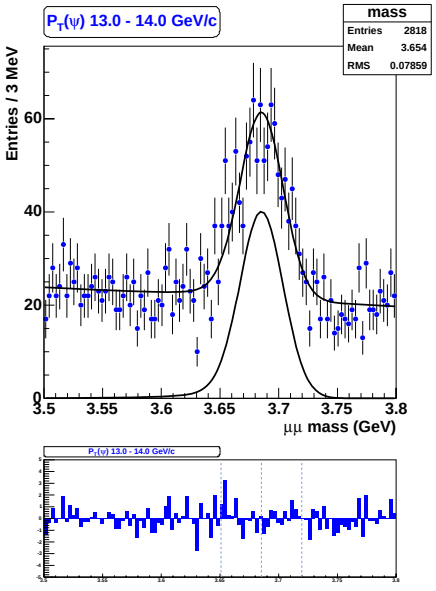
$P_T(\psi)$ 13.0 - 14.0 GeV/c
mass
Entries 2818
Mean 3.654
RMS 0.07859
Entries / 3 MeV
μμ mass (GeV)

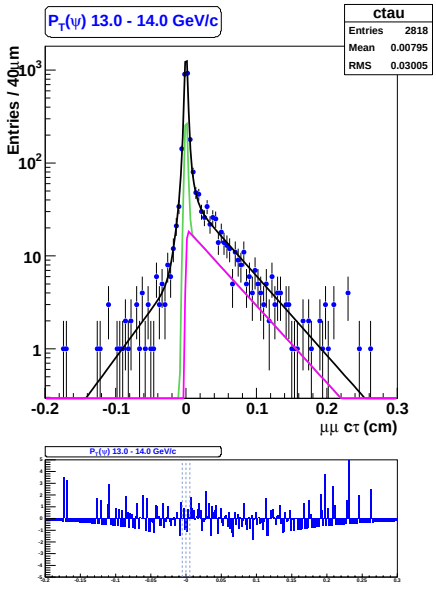
$P_T(\psi)$ 13.0 - 14.0 GeV/c
ctau
Entries 2818
Mean 0.00795
RMS 0.03005
Entries / 40 μm
μμ cτ (cm)

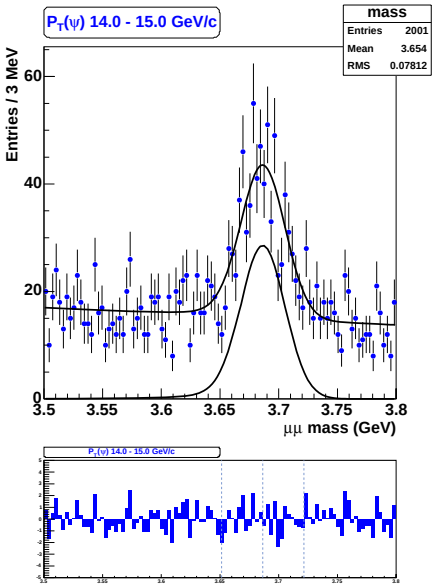
$P_T(\psi)$ 14.0 - 15.0 GeV/c
mass
Entries 2001
Mean 3.654
RMS 0.07812
Entries / 3 MeV
μμ mass (GeV)

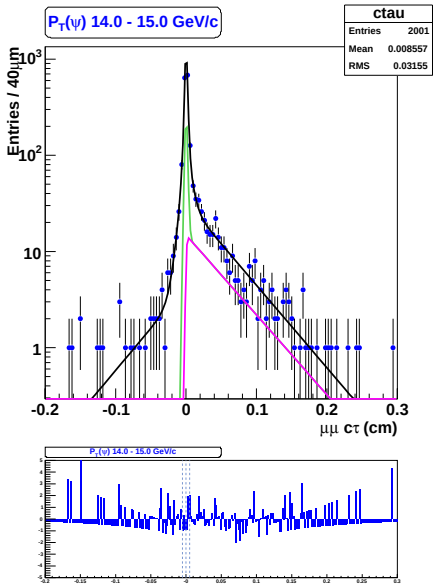
$P_T(\psi)$ 14.0 - 15.0 GeV/c
ctau
Entries 2001
Mean 0.008557
RMS 0.03155
Entries / 40 μm
μμ cτ (cm)

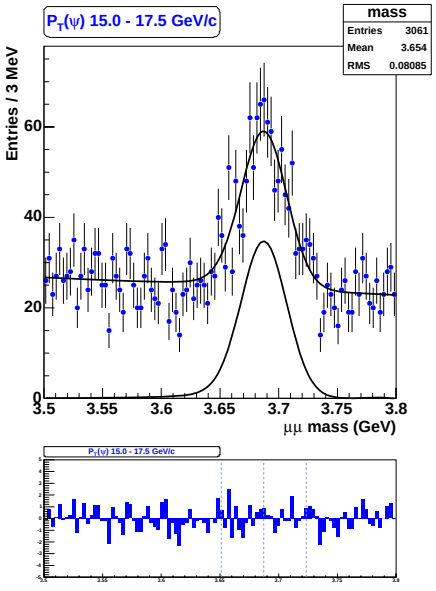
$P_T(\psi)$ 15.0 - 17.5 GeV/c
mass
Entries 3061
Mean 3.654
RMS 0.08085
Entries / 3 MeV
μμ mass (GeV)

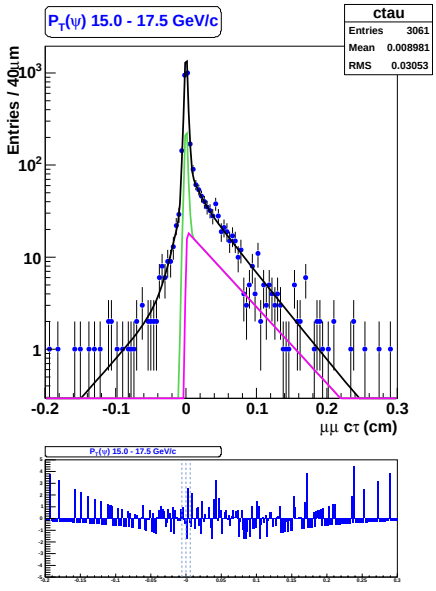
$P_T(\psi)$ 15.0 - 17.5 GeV/c
ctau
Entries 3061
Mean 0.008981
RMS 0.03053
Entries / 40 μm
μμ cτ (cm)

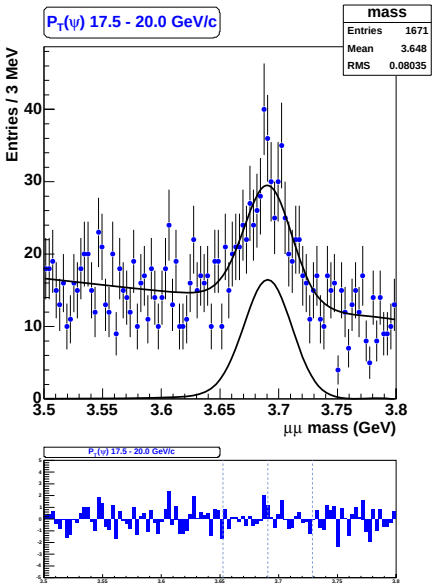
$P_T(\psi)$ 17.5 - 20.0 GeV/c
mass
Entries 1671
Mean 3.648
RMS 0.08035
Entries / 3 MeV
μμ mass (GeV)

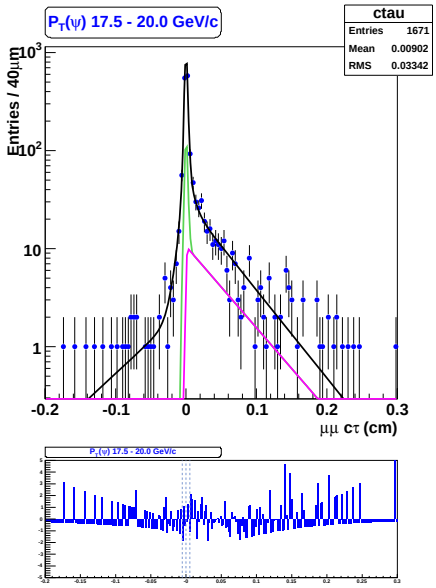
$P_T(\psi)$ 17.5 - 20.0 GeV/c
ctau
Entries 1671
Mean 0.00902
RMS 0.03342
Entries / 40μm
μμ cτ (cm)

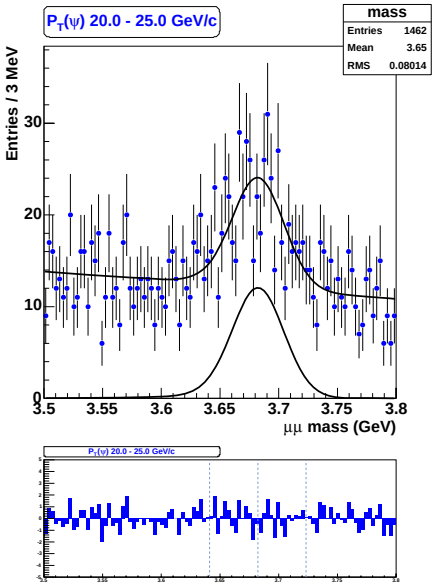
$P_T(\psi)$ 20.0 - 25.0 GeV/c
mass
Entries 1462
Mean 3.65
RMS 0.08014
Entries / 3 MeV
μμ mass (GeV)

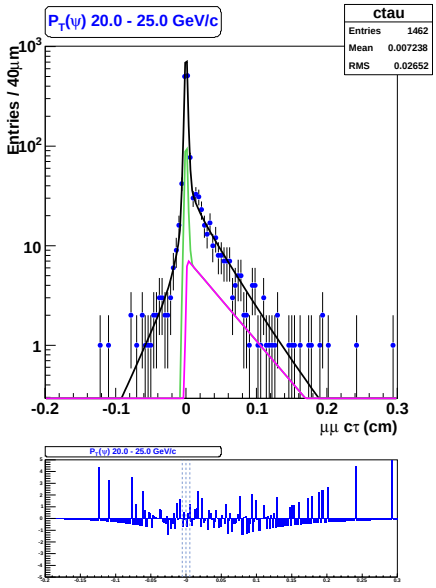
$P_T(\psi)$ 20.0 - 25.0 GeV/c
ctau
Entries 1462
Mean 0.007238
RMS 0.02652
Entries / 40μm
μμ cτ (cm)

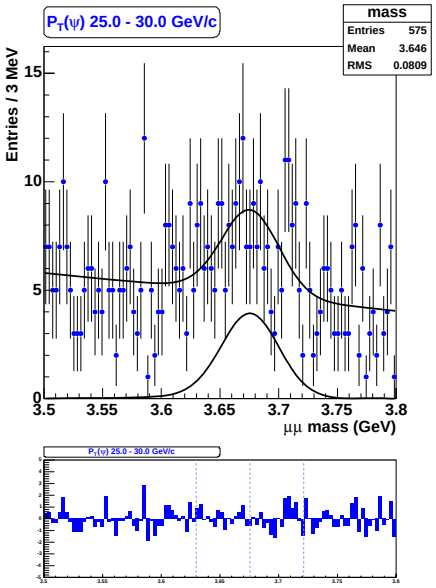
$P_T(\psi)$ 25.0 - 30.0 GeV/c
mass
Entries 575
Mean 3.646
RMS 0.0809
Entries / 3 MeV
μμ mass (GeV)

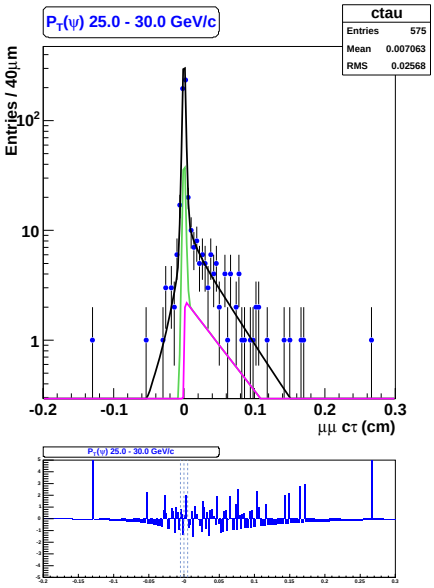
$P_T(\psi)$ 25.0 - 30.0 GeV/c
ctau
Entries 575
Mean 0.007063
RMS 0.02568
Entries / 40μm
μμ cτ (cm)

$P_T(\psi(2S))$	$< P_T >$	χ^2/ndf	Fit Prob.
2.0-2.5	2.30	64.54 / 100	0.998
2.5-3.0	2.77	103.20 / 100	0.393
3.0-3.5	3.25	104.44 / 100	0.361
3.5-4.0	3.75	108.48 / 100	0.264
4.0-4.5	4.24	118.70 / 100	0.098
4.5-5.0	4.74	101.92 / 100	0.428
5.0-5.5	5.24	95.04 / 100	0.622
5.5-6.0	5.74	71.09 / 100	0.987
6.0-6.5	6.24	95.97 / 100	0.595
6.5-7.0	6.74	90.05 / 100	0.752
7.0-7.5	7.24	126.81 / 100	0.036
7.5-8.0	7.74	74.24 / 100	0.975
8.0-8.5	8.24	122.59 / 100	0.062
8.5-9.0	8.74	125.59 / 100	0.043
9.0-9.5	9.24	78.29 / 100	0.947
9.5-10	9.74	104.81 / 100	0.351
10 - 11	10.46	103.98 / 100	0.373
11 - 12	11.46	95.34 / 100	0.613
12 - 13	12.47	123.37 / 100	0.056
13 - 14	13.48	111.70 / 100	0.199
14 - 15	14.48	132.97 / 100	0.015
15 - 17.5	16.12	109.69 / 100	0.239
17.5 - 20	18.61	106.26 / 100	0.315
20 - 25	22.08	100.65 / 100	0.463
25 - 30	27.09	128.16 / 100	0.030

Table C.1: $\sum \chi^2/\mathrm{ndf} = 2597.88/2500$, $\chi^2 - \mathrm{Prob.} = 8.44\%$

Appendix D

DPS Accounting - Luminosity for Dynamically Prescaled Trigger Paths

There are many trigger paths which have been prescaled in order to be fitted into the limited trigger bandwidth. And more comes as we have higher instantaneous luminosity.

In case a trigger path is prescaled, the integrated luminosity measured by CLC cannot not be simply used for the trigger path since the trigger path accepts only a certain fraction of total events that satisfy the trigger cuts. And there was no simple tool to get a correct luminosity information for prescaled trigger paths directly from the data.

Based on the fact that the scaler controls trigger prescales, we have calculated the effective luminosity for prescaled trigger paths. The effective luminosity is calculated in each run section by trigger id and then integrated over a run by trigger id. The integrated luminosity of every run in zero bias dataset(gcrs0d, gcrs0h, and gcrs0i) is stored in CDF offline database(`FILECATALOG.CDF2_RUNS_WITH_LUMINOSITY`) by trigger paths.

Users can retrieve the luminosity information for a trigger path by using a wrap-up script `dpslum.sh` or `DFCLuminosityTool` [1].

[1] See appendix.

D.1 Prescale and Luminosity calculation

A scaler information is used to retrieve trigger counts before and after prescale. For normal cases(Dynamic Prescale, Luminosity Enable, and Rate Limit), we use the trigger counts recorded in SL1D(Level 1) and TL2D(Level 2). In addition, any trigger prescaled by hand can be treated as normal case.

For special cases:

- Fractional Prescale - use FPS pre-Fred input scaler for counts after prescale and Fred Live scaler for counts before prescale.
- Über Prescale - use counts of the number of empty buffers.
- L2 Rate - use L2 trigger scaler for counts after prescale and L1 prereq scaler in L2 for counts before prescale.

A numeric integration over run sections gives the effective luminosity:

$$\mathcal{L}_{eff} = \sum_i \frac{A_i - A_{i-1}}{B_i - B_{i-1}} \int_{t_{i-1}}^{t_i} \mathcal{L}\, dt \tag{D.1}$$

where B_i and A_i denote the trigger counts before and after prescale.

D.1.1 PrescaleModule

The PrescaleMoudle is a C++ module which reads the trigger counts from zero bias data(gcrs0*) and fills in `PRESCALE.CDF2_RUNSECTION_LIVETIMES` table. For every run section, it stores level 1 and level 2 scaler information of the last event in each run section by trigger ID.

It also checks SVT beamline status at the beginning and skips bad SVT beamline run sections for SVT triggers using data quality bit 19 in `CDF2_RUNSECTIONS`.

D.2 DFCPrescaleDataFiller

After PrescaleModule filled in `PRESCALE.CDF2_RUNSECTION_LIVETIMES table`, DFCPrescaleDataFiller(The Filler) reads the trigger counts before and after prescale and calculate fractions(1/prescale) from two consecutive run sections. Then the calculated fractions are recorded in the same table for every run section by trigger ID. And the Filler calculate the effective luminosity:

$$\mathcal{L}_{eff} = \frac{1}{P^{L3}} \cdot \sum_i \delta_i^{SVT} \; f_i^{L1} \; f_i^{L2} \; \mathcal{L}_i \tag{D.2}$$

where P^{L3} is level 3 prescale, $f_i^{L1(L2)}$ is the L1(L2) fraction of i th run section.

D.3 DFCPrescaleDataFixer

In a certain period of early 0i data, the Scalers were truncated to fit in the buffer. When there are run sections with truncated TL2D bank, DFCPrescaleDataFixer tries to find non-truncated run section and average over multiple run sections.

D.4 Checking process - Script1 and Script2

The result of PrescaleModule has been checked in two aspects, missing run sections and luminosity. The Script1 checks whether any run section is missed by PrescaleModule. We found that zero bias data didn't have information for some run sections.

Example:

```
**** In Script1: ==> found (2) missing run_section(s)
     in cdf2_runsection_livetimes for run_number = 203873
**** ==> sessionID = 50  is missing
**** ==> sessionID = 51  is missing
```

The Script2 compares calculated effective luminosities of (prescale factor) $\times$ `JET_20`(prescaled) and `JET_100`(unprescaled).

Example:

```
lumi_check ==> run  = 203896
lumi_check: lumi_jet100 * 1000                      = 54.7547
lumi_check: sumLumiOffline_cdf2_runsections         = 54.75473
lumi_check: lumi_jet20 * 1000                  = 0.0438054
lumi_check: PS_factor (l1_PS(50) * l2_PS(25)) = 1250
lumi_check: lumi_jet20 * pS_factor                  = 54.75675
```

D.5 Summary

The effective luminosities for prescaled trigger paths have been calculated and recorded in CDF offline databse(`FILECATALOG.CDF2_RUNS_WITH_LUMINOSITY`) by run number and trigger path. And the information can be retrieved by using DFCLuminosityTool. The current tool extracts the effective luminosity for runs.

But since `PRESCALE.CDF2_RUNSECTION_LIVETIMES` table has prescale information in section level, the luminosity for each section can be extracted in principle.

There are 2285 runs(897633 sections) in gcrs0d dataset, 972 runs(426039 sections) in gcrs0h dataset, and 1019 runs(506811 sections) in gcrs0i dataset [2]. The period 10(287 runs) is also added.

From period 11, we plan to integrate PrescaleModule into the automatic calibration sequence.

D.6 `dpslum.sh` and `DFCLuminosityTool`

D.6.1 `dpslum.sh`

This is a wrap-up script of DFCLuminosityTool. The script reads run numbers from the run list provided by users and returns the total luminosity for the specified tirgger path.

[2] up to period 9

Example:

```
>./dpslum.sh runlist JPSI_CMUCMU1.5_DPS

##### Retrieving luminosity from db #####

##### Calculating lum sum for  706  runs #####

JPSI_CMUCMU1.5_DPS       363.065728014

>more dpslum.sh

#!/bin/bash
########################################
# A wrap-up script of DFCLuminosityTool  #
# dpslum.sh [run_list] [path_name]       #
#                                        #
# K. Chung  Thu Apr 26 23:03:31 CDT 2007 #
########################################

source ~cdfsoft/cdf2.shrc
setup cdfsoft2 6.1.4int3

exec < $1
count=0;
echo "     "
echo "##### Retrieving luminosity from db #####"
echo "     "

while read run
do
let "count+=1"
DFCLuminosityTool -db production_file_catalog -runs "$run" -path_name "$2" >> lum.tmp
done
sum=0;
echo "##### Calculating lum sum for " $count " runs #####"
exec <lum.tmp
while read path luminosity
do
sum=$(echo "scale=6;$sum+$luminosity" | bc)
done

# print out the result #
echo "   "
```

```
echo $2 "     " $sum
echo "     "
rm lum.tmp
exit 0
```

D.6.2 DFCLuminosityTool

```
>setup cdfsoft2 6.1.4int3
>DFCLuminosityTool -help

 Usage:
        -db <database_id, e.g data_file_catalog>
        -runs <runs space separated list of runs, enclosed in " ">
        -range <runs range specified as "[low,high]">
        -table_name <name of physics table, enclosed in " " (optional)>
        -table_tag <table tag (optional)>
        -path_name <name of L3 path, enclosed in  " " (optional)>
        -path_tag <L3 pat tag, (optional)>
        either -runs or -range has to be specified
        if unsure use with -range "[0,999999]"
        -with_tag (Switch - with tag switch)
        -help (Switch - help output)
```

Example:

```
>setup cdfsoft2 6.1.4int3
>DFCLuminosityTool -db production_file_catalog \
>                  -range "[203819,204109]" \
>                  -path_name "JPSI_CMUCMU1.5_DPS"

                  JPSI_CMUCMU1.5_DPS      6.37906

>DFCLuminosityTool -db production_file_catalog \
>                  -runs "203819 203824 203826 203869 203871 \
```

```
>                          203872 203873 203874 203881 203894 \
>                          203896 204076 204077 204079 204082 \
>                          204105 204107 204109" \
>                   -path_name "JPSI_CMUCMU1.5_DPS"

                  JPSI_CMUCMU1.5_DPS      6.37906
```

Colophon

This thesis was made in LaTeX 2_ε using the “hepthesis” class [42].

Bibliography

[1] J. D. Bjorken, Phys. Rev. **179**, 1547 (1969).

[2] W. E. Caswell and G. P. Lepage, Phys. Lett. B **167**, 437 (1986).

[3] G. T. Bodwin, E. Braaten and G. P. Lepage, Phys. Rev. D **51**, 1125 (1995).

[4] CERN Yellow Report, CERN-2005-005, Geneva: CERN, 2005.- 487 p. [arXiv:hep-ph/0412158].

[5] W. M. Yao *et al.* [Particle Data Group], J. Phys. G **33**, 1 (2006).

[6] G. A. Schuler, arXiv:hep-ph/9403387.

[7] [CDF Collaboration], arXiv:hep-ex/9412013.

[8] E. Braaten and T. C. Yuan, Phys. Rev. Lett. **71**, 1673 (1993).

[9] E. Braaten and S. Fleming, Phys. Rev. Lett. **74**, 3327 (1995).

[10] P. Cho and M. Wise, Phys. Lett. B **346**, 129 (1995).

[11] S. Catani, M. Ciafaloni and F. Hautmann, Phys. Lett. B **242**, 97 (1990).

[12] J. C. Collins and R. K. Ellis, Nucl. Phys. B **360**, 3 (1991).

[13] G. Camici and M. Ciafaloni, Phys. Lett. B **386**, 341 (1996).

[14] M. G. Ryskin, A. G. Shuvaev and Y. M. Shabelski, Phys. Atom. Nucl. **64**, 120 (2001).

[15] F. Abe *et al.* [CDF Collaboration], Phys. Rev. Lett. **79**, 572 (1997).

[16] V. A. Khoze, A. D. Martin, M. G. Ryskin and W. J. Stirling, Eur. Phys. J. C **39**, 163 (2005) [arXiv:hep-ph/0410020].

[17] M. G. Ryskin, Z. Phys. C **57**, 89 (1993).

[18] A. A. Affolder *et al.* [CDF Collaboration], Phys. Rev. Lett. **85**, 2886 (2000) [arXiv:hep-ex/0004027].

[19] Fermilab-PUB-96/390-E.

[20] F. Abe *et al.* [CDF Collaboration], Nucl. Instrum. Meth. A **271**, 387 (1988).

[21] A. Sill [CDF Collaboration], Nucl. Instrum. Meth. A **447**, 1 (2000).

[22] Fermilab-Proposal-909.

[23] A. A. Affolder *et al.* [CDF Collaboration], Nucl. Instrum. Meth. A **526**, 249 (2004).

[24] D. Acosta *et al.*, Nucl. Instrum. Meth. A **494**, 57 (2002).

[25] K. Chung *et al.*, CDF Note 8212 (2006).

[26] D. Glenzinski *et al.*, CDF Note 7314 (2007).

[27] `http://www-cdf.fnal.gov/internal/physics/bottom/b-montecarlo/`

[28] D. J. Lange, Nucl. Instrum. Meth. A **462**, 152 (2001).

[29] D. E. Acosta *et al.* [CDF Collaboration], Phys. Rev. D **71**, 032001 (2005) [arXiv:hep-ex/0412071].

[30] `http://fcdfhome.fnal.gov/usr/slava77/cdfnotes/7314/code/`

[31] T. Delvin, CDF Note 3126 (1995).

[32] J. Gaiser, SLAC-R-255 (1982).

[33] G. Punzi, PHYSTAT2003, SLAC Sep. 8-11 (2003).

[34] S. P. Baranov, Phys. Rev. D **66**, 114003 (2002).

[35] K. Chung *et al.*, CDF Note 8980 (2007).

[36] G. Bauer *et al.*, CDF Note 3561 (1996).

[37] K. Anikeev *et al.*, arXiv:hep-ph/0201071.

[38] F. Abe *et al.* [CDF Collaboration], Phys. Rev. Lett. **79**, 578 (1997).

[39] A. Abulencia *et al.* [CDF Collaboration], Phys. Rev. Lett. **99**, 132001 (2007) [arXiv:0704.0638 [hep-ex]].

[40] F. Maltoni *et al.*, Phys. Lett. B. **638**, 202 (2006).

[41] S. U. Chung, BNL-QGS-02-0900 (2005)

[42] A. Buckley, `http://www.insectnation.org/projects/hepthesis/`

List of Figures

List of Tables